Downloaded from orbit.dtu.dk on: May 05, 2023

DTU Library

Modeling of Coupled Nano-Cavity Lasers

Skovgård, Troels Suhr

Publication date:
2012

Document Version
Publisher's PDF, also known as Version of record

Link back to DTU Orbit

Citation (APA):
Skovgård, T. S. (2012). *Modeling of Coupled Nano-Cavity Lasers*. Technical University of Denmark.

General rights
Copyright and moral rights for the publications made accessible in the public portal are retained by the authors and/or other copyright owners and it is a condition of accessing publications that users recognise and abide by the legal requirements associated with these rights.

- Users may download and print one copy of any publication from the public portal for the purpose of private study or research.
- You may not further distribute the material or use it for any profit-making activity or commercial gain
- You may freely distribute the URL identifying the publication in the public portal

If you believe that this document breaches copyright please contact us providing details, and we will remove access to the work immediately and investigate your claim.

Modeling of Coupled Nano-Cavity Lasers

A dissertation submitted to the Department of Photonics Engineering at the Technical University of Denmark as part of the requirements for the degree of Doctor of Philosophy

Troels Suhr Skovgård
15. maj 2012
Version 1.4

ABSTRACT

Modeling of nanocavity light emitting semiconductor devices is done using the semiconductor laser rate equations with spontaneous and stimulated emission terms modified for Purcell enhanced recombination. The modified terms include details about the optical and electronic density-of-states and it is argued that Purcell enhancement should also be included in stimulated recombination term, contrary to the common practice in the literature. It is shown that for quantum well devices, the Purcell enhancement is effectively independent of the cavity quality factor due to the broad electronic density-of-states relative to the optical density-of-states. The low effective Purcell effect for quantum well devices limits the highest possible modulation bandwidth to a few tens of gigahertz, which is comparable to the performance of conventional diode lasers. Compared to quantum well devices, quantum dot devices have narrower electronic density-of-states and are not affected by the reduction of the Purcell enhancement to the same degree. The highest modulation bandwidth is found for below threshold operation, where the bandwidth is not cavity-limited.

Using finite-difference time-domain methods, systems of passive, coupled photonic crystal nanocavity structures are simulated. The resonance frequencies of in-phase and out-of-phase coupled quadrupole modes in rectangular photonic crystal H1 cavities are extracted and are found to vary non-trivially with the intercavity separation. A qualitative explanation is given in terms of the in-plane mode profiles. Farfield emission patterns for the structures are calculated based on the finite-difference time-domain simulations. It is found that only systems with an even number of holes separating the cavities show clear signs of being coupled. This non-trivial coupling behavior is useful for design of coupled systems.

A tight-binding description for coupled nanocavity lasers is developed and employed to investigate the phase-locking behavior for the system of two coupled cavities. Phase-locking is found to be critically dependent on exact parameter values and to be difficult to achieve for systems with large linewidth enhancement factors and low Purcell enhancement such as quantum well based lasers. Realistic numbers for the coupling strength are extracted from finite-difference time-domain simulations.

RESUMÉ

Lysgenerering i halvleder nanokavitetskomponenter bliver modelleret ved hjælp af rate ligninger for halvleder lasere, hvor leddene for spontan og stimuleret emission er modificeret til at inkludere Purcell forstærket rekombination. De modificerede led inkluderer detaljer om den optiske og elektroniske tilstandstæthed og der bliver argumenteret for at Purcell forstærkningen også bør inkluderes i leddet for stimuleret rekombination, hvilket går imod den almindelige opfattelse i litteraturen. Det bliver vist at for kvantebrøndskomponenter er Purcell forstærkningen reelt uafhængig af kavitetens kvalitetsfaktor på grund af den brede elektroniske tilstandstæthed i forhold til den optiske tilstandstæthed. Den lave effektive Purcell effekt for kvantebrøndskomponenter begrænser den højest mulige modulationsbåndbredde til langt under 100 gigahertz hvilket er sammenligneligt med konventionelle diode laseres præstationsniveau.
Sammenlignet med kvantebrønde har kvanteprik komponenter smallere elektroniske tilstandstætheder og er ikke påvirket i samme grad af reduktionen af Purcell forstærkningen. Den højeste modulationsbåndbredde er fundet for operation under tærsklen hvor båndbredden ikke er begrænset af kavitetens båndbredde.
Ved brug af finite-difference time-domain metoder simuleres passive, koblede fotonisk krystal nanokavitet strukturer. Resonansfrekvenser for koblede kvadrupoltilstande i og ude af fase i rektangulære fotonisk krystal H1 kaviteter bliver bestemt og viser sig at variere ikke-trivielt med afstanden mellem kaviteterne. En kvalitativ forklaring bliver givet på baggrund af tilstandsprofilerne i planet. Fjernfelt-emissionsmønstre for strukturerne bliver beregnet på baggrund af finite-difference time-domain beregningerne. Det viser sig at kun systemer med et lige antal huller imellem kaviteterne viser tydelige tegn på kobling.
En tight-binding beskrivelse af koblede nanokavitetslasere bliver udviklet og anvendt til at undersøge fase-låsning i systemer med to koblede kaviteter. Faselåsning viser sig at være kritisk afhængig af de præcise parameterværdier og at være vanskelig at opnå i systemer med store linjebredde forstærkningsfaktorer og lav Purcell forstærkning så som lasere baseret på kvantebrønde. Realistiske værdier for koblingsstyrken bliver udledt fra finite-difference time-domain simuleringer.

ACKNOWLEDGEMENTS

I owe thanks to a great number of people for their help and support in the development of this thesis. The positive working environment at DTU Fotonik and the help of friends and colleagues has made the work enjoyable and significantly improved the quality of the end product. Thank you all for making it interesting and challenging. Some people deserve special mentioning, so here goes in no particular order:

My supervisors Jesper Mørk and Niels Gregersen have with their patient help and much-needed insights ensured that the project did not veer (too much) off course. Thank you for always being available for discussions and advice. Lars Hagedorn Frandsen, who was supervisor for a short while, was helpful in the early stages of the project.

Martin Schubert has been a great help throughout the project by assisting me with the `MEEP` code, by allowing me into his laboratory and by showing great perseverance. Seemingly endless discussions about farfields and related issues was especially important for the development of the results in chapter 5.

The comparison to the Cluster Expansion Model in chapter 4 is the result of collaboration with Michael Lorke, who also initiated several necessary sanity checks along the way. He was also the first to point out that Purcell enhancement should be included in the laser rate equation stimulated emission term, which formed the basis for much of the following work.

Thanks to Philip Trøst Kristensen, Jin Liu, Mikkel Heuck and the three Nielsens, Per, Torben and Henri, for many helpful discussions along the way.

Special thanks goes to my fellow inmates of room 166, Andrei Andryieuski, Thor Ansbæk, Sara Ek and Roza Shirazi, who were always available for cake, discussion or procrastination, depending on the need. Thank you for putting up with the seemingly endless discussions about farfields mentioned above.

Finally, thanks go to my lovely wife, Stine, for love and support and to my son, Viktor, for providing welcome distractions.

CONTENTS

1. INTRODUCTION

The problem of long distance communication has always been of great importance, because of the obvious advantages of being able to communicate your thoughts to someone far away. Considerable effort and ingenuity has been invested in solving this problem and there has always been a striving for faster, more efficient and more reliable means of communication. The main mode of communication has developed from runners and bonfires in medieval times, over the enormous telegraph networks in the 19th century and to the transatlantic telephone networks of the 20th century.

The invention and development of the semiconductor laser diode in the 1960s and the optical fiber in the 1980s ushered in a new era in communications. Optical communication systems offer several advantages over the electrical wire based systems [1].
First, the production cost for copper wires is significantly larger than that of optical fibers (for the same information capacity). At the same time, electrical cables are perhaps 10-20 times heavier than a corresponding optical cable, which makes the laying of the optical cables relatively cheaper. Furthermore, loss and noise issues are smaller in optical fibers, allowing for larger distance between regeneration stations ($\sim$10 km for electrical cables and $\sim$100 km for optical fibers).
Secondly, the information capacity of optical fibers is much larger than that of electrical cables. Where an electrical cable can carry perhaps 2000 telephone calls simultaneously it has recently been demonstrated that a single optical fiber can handle close to 60 million phone calls (5.1 Tbit/s) at a single wavelength [2]. Furthermore, optical communication allows for wavelength division multiplexing techniques, which could increase the capacity by perhaps a factor of 1000. Because of the large capacity of optical fibers the communication system can be upgraded relatively easily simply by changing the emitters, detectors and repeater stations.
Thirdly, optical communication is more secure, as optical cables are more difficult to tap into and the signals are harder to manipulate. There are few places where a tap is practically possible and even then, any interference with the signal is easily detectable.

For these reasons nearly all long-haul telecommunication is handled today by fiber optics and the trend is to convert smaller and smaller systems to fiber optics. Today metro access networks, local access networks and even rack-to-rack networks are routinely set up using fiber optics and the next step in the contin-

ued down-scaling of the system size is to replace the electrical interconnects on computer chips by the optical equivalent. There are several compelling reasons to do so [3–6]:

1. **Charging time:** While the individual transistor becomes faster as the feature length scale decreases, the same is not true for the electrical interconnects. The charging time of these interconnects, which is determining for the communication speed, is more or less scale invariant. Optical interconnects transmit data using photons rather than electrons and are therefore not limited by this charge time issue.

2. **Power consumption:** How much power a CPU can consume ultimately depends on how much heat can be removed by cooling. The limited amount of available power must be divided between the different parts of the CPU. As the feature length decreases more and more energy is consumed by the interconnects so that with 2002 technology ∼50% of the available power was taken up by the interconnects. Estimates suggests that in order to meet future power limitations the interconnects cannot use more than 100 fJ/bit. This is difficult to achieve with electrical interconnects, but is feasible using optical interconnects.

3. **Design issues:** Due to the charging time issue mentioned above, long electrical wires are problematic at high data rates. Optical interconnects do not have this problem, which allows for new and more simple designs of the CPU. Furthermore, a CPU using electrical wiring is designed to operate at a certain clock-speed and cannot deviate significantly from this operation speed, as this will lead to different loss and inductance, cross-talk effects and wave reflection issues. In optically based systems, the chip designs can be recycled at higher operation speeds, as the modulation of the light has no practical influence on its propagation.

4. **Environmental issues:** An argument that is seen more and more frequently at conferences and in paper abstracts is that of the environmental impact of telecommunication. As of 2005 ∼1% of the worlds energy was consumed by data centers across the world. While this does not sound too bad compared to e.g. the transport or production sector, one has to keep in mind that unlike other sectors, the telecommunication sector increases by more than 40 % per year.

Equally important as the optical interconnects are the light sources that will generate the modulated signal. These must be small enough to fit on the chip, efficient enough to meet the power consumption criteria and fast enough to keep up with the data rates required. Further increase in the bandwidth of conventional light emitting diodes is difficult and in this context nanocavity devices become interesting.

Nanocavity light emitting devices are characterized by using optical cavities that confine the light on a length scale comparable to the light wavelength [7–23]. The ultra tight confinement of the optical mode gives a very large

amplitude of the electromagnetic field in the cavity, which leads to a strong light-matter interaction. The enhanced interaction is known as the Purcell effect, which was first described by E. M. Purcell in 1946 [24]. In light emitting devices, the Purcell factor gives faster recombination rates and therefore also lower threshold and higher modulation speed. Thus, nanocavity light emitting devices improve on all the requirements for integration of optical interconnects on chips. The basic viability of the concept of the nanocavity light emitter has already been demonstrated experimentally in several papers [7–23], perhaps most notably in the work by M. Notomi *et al.* [21], who recently presented nanocavity lasing at 50 % quantum efficiency and with a modulation bandwidth of 20 GHz at 8.8 fJ/bit. Theoretical studies of nanocavity light emitters have been undertaken by several groups [25–28], however, a firm theoretical understanding of the processes involved and the limitations of nanocavity lasers has yet to emerge.

Of course, fast and efficient light sources are also of interest for long-haul communication, but here the microscopic length scale of the devices becomes an obstacle. This is because the output power necessarily decreases with the amount of active material that can fit inside the cavity. For nanocavity devices, this makes the output power too low to be practically usable over long distances. The obvious solution is to couple many nanocavity devices together in large arrays, so that the combined output becomes of usable size. This approach, however, has its own problems as the devices must be phase-locked and the emission profile must be controlled. Some work has already been done in this area. Experimental studies of coupled arrays of nanocavity lasers was carried out by H. Altug et al. [12] in 2006 where lasing was observed as well as high modulation speed although the latter claim has since been contested [26]. Coupling of diode lasers was studied in the 1980s by H. G. Winful and S. S. Wang [29, 30], who developed a coupled mode theory for this type of systems. However, this study was restricted to conventional light emitting devices.

The present work aims at advancing on both fronts by developing models for the nanocavity light emitting devices, by studying the optical properties of the devices involved and by simulating coupled nanocavity systems. We wish to treat the nanocavity devices in a simple and easily analyzable model, which at the same time is accurate enough to include all important effects. Laser rate equations fulfill both of these requirements and have the additional benefit of being widely known in the literature. However, the laser rate equations have mostly been used for modeling of conventional semiconductor laser diodes and are not immediately suited for nanocavity lasers modeling. Modifying the laser rates to also apply to the nanocavity regime is then the first objective and is treated in chapter 2 and 3. We analyze the model in chapter 4 and attempt to validate our findings by comparing to experimental work and to a more accurate microscopic model.

The optical properties of the nanocavity devices are investigated in chapter 5, where finite-difference time-domain simulations of relevant structures are

carried out. This simulation tool can be used to extract structure parameters such as mode volume and Q-factors, but can also be used to understand experimental results. In this chapter, we investigate systems of two coupled photonic crystal cavities and see how the coupling affects farfield radiation patterns.

Finally, in chapter 6 coupling terms for two coupled cavities are developed in a tight-binding model and included in the laser rate equations. This allows for a study of the conditions that have to be met for phase-locking to occur in nanocavity lasers.

2. BASIC CONCEPTS

In this chapter, we first introduce a number of basic concepts for conventional semiconductor lasers. Next, key elements of nanocavity light emitters are defined and finally a short overview of the nanoscale light confinement techniques used in the following chapters is presented.

2.1 Conventional Diode Lasers

Most of the light that we see is the result of two fundamental recombination processes, spontaneous and stimulated emission, which bring excited electrons to lower energy states under the emission of light.

Spontaneous emission is a random process where the decay of the excitation happens at an unpredictable time and the photon is emitted in a random direction [31, 32] (See schematic in figure 2.1a.). Spontaneous emission is by far the most common light emission mechanism and nearly all natural light is the result of some spontaneous emission process. Spontaneous emission exists under many names depending on the source of the excitation [33]. For example, in fluorescence the emitter is excited by light at a shorter wavelength, in chemiluminescence the excitation comes from chemical reactions and in triboluminescence the energy comes from breaking bonds in certain solids, e.g. by crushing sugar cubes. In semiconductor light emitters the excitations are created by photoluminescence or by electroluminescence, i.e. by passing current through the material.

Stimulated emission is the decay of an excitation due to the presence of another photon (figure 2.1b). The stimulated emission process has some interesting and useful features. First, the photon is emitted in the same mode (the same direction) as the stimulating photon and second, the two photons will be in phase [31, 32]. Thus, every stimulated emission event constructively interferes with the electromagnetic field. In a quantum optics interpretation, stimulated emission works by the same basic process as spontaneous emission. However, in spontaneous emission the excitation decay is not stimulated by another photon, but by vacuum field fluctuations [32].

Apart from the two emission processes, stimulated absorption is also of importance for light emitting devices. This process is the reverse of a stimulated emission event, i.e. an incoming photon is absorbed by an electron in its low energy state producing an excitation (figure 2.1c). Thus, each stimulated ab-

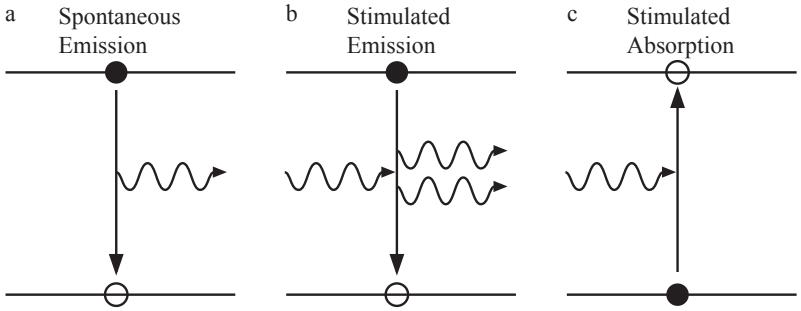

Fig. 2.1: a) In the spontaneous emission process, an excitation decays and emits a photon in a random direction. b) Stimulated emission requires an incoming photon to trigger the excitation decay. The emitted light is in the same direction as the incoming photon and in phase. c) The stimulated absorption process consumes one photon and creates one excitation.

sorption event subtracts a photon from the optical field.

Semiconductor light emitting devices function by these three processes and are divided into two groups according to which process is dominant. For Light Emitting Diodes (LEDs), light is produced through spontaneous emission, while the coherent emission from a laser is the result of stimulated emission. A conceptual laser design is shown in figure 2.2. It consists of active (excitable) material in an optical cavity, which in this example is two aligned mirrors (one being semi-transparent). The active material can be excited through various means, but semiconductor devices are typically electrically pumped. Electrons are injected into the conduction band by applying a voltage across the semiconductor and they recombine with holes injected into the valence band.
At weak pump (figure 2.2 top left), only a limited number of emitters are excited and the photon density is therefore low. The probability of having a stimulated emission or absorption event is thus also low. This is the LED regime, where spontaneous emission is responsible for almost all emission events.
At higher pump power (figure 2.2 top center), the photon density increases and the probability of having stimulated events is increased. The photons that are emitted in the direction of the mirrors are caught by the optical cavity. For every cavity round trip, the photons trigger more stimulated events and a coherent field builds up. Spontaneous emission still contributes significantly to the photon density and this pumping regime is called the threshold regime.
At even higher pump power (figure 2.2 top right), stimulated emission is the most dominant process and almost all emitted photons adds to the coherent field. This is the lasing regime.

An important experimental characteristic of a laser is the input-output curve (I/O curve), which is shown in figure 2.2 (bottom). The transition from the LED regime to the laser regime is seen in the input-output curve as a sharp non-linear increase in the output. The low output in the LED regime reflects

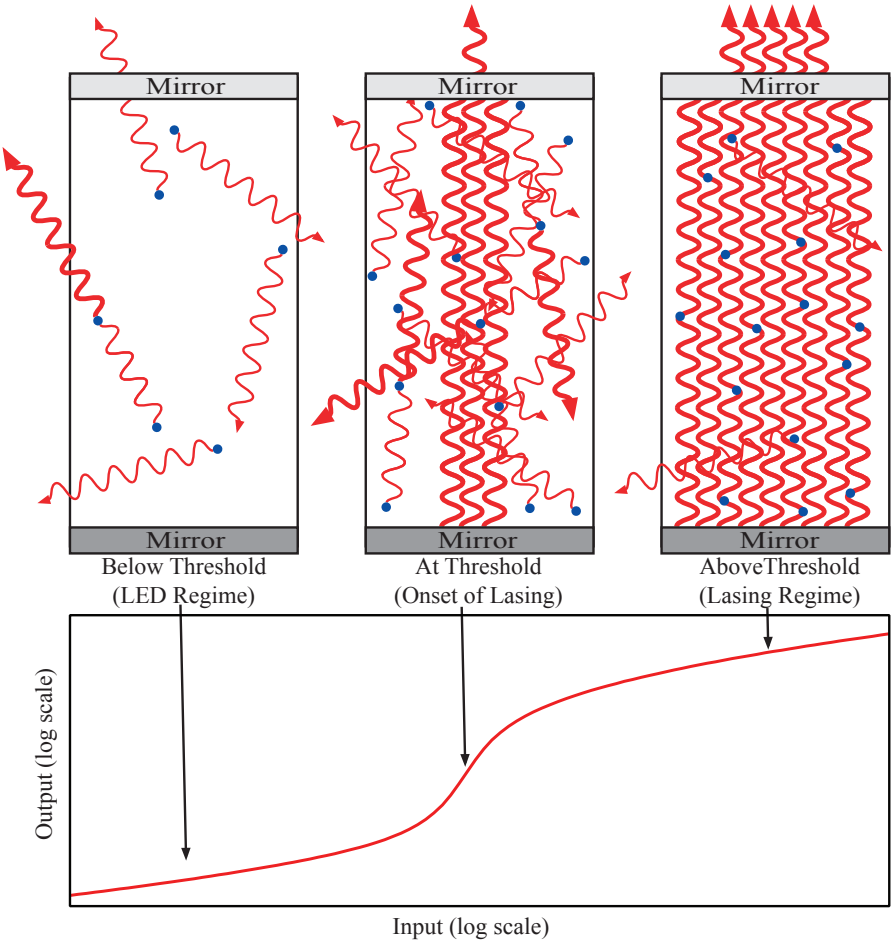

Fig. 2.2: Top: A conceptual laser design at three pump levels: Below threshold, at threshold and above threshold. Blue circles are excited emitters, wavy lines are photons. Bottom: A general input-output curve.

the fact that only a small fraction of all the spontaneously emitted photons are caught by the cavity. This fraction, called the β-factor, is of the order of 10^{-5} for conventional semiconductor diode lasers. Above threshold nearly all photons are created by the stimulated emission process and are thus always emitted in the right direction.

A characteristic dynamical property, which is of special interest for telecommunication applications, is the modulation bandwidth of the device. This is a measure of how fast the input power can be modulated while still maintaining a reasonable output. Figure 2.3 shows examples of a modulation response curves for increasing pump. At high frequencies, the output becomes limited by e.g. the speed of the emission processes or the cavity lifetime and the modulation

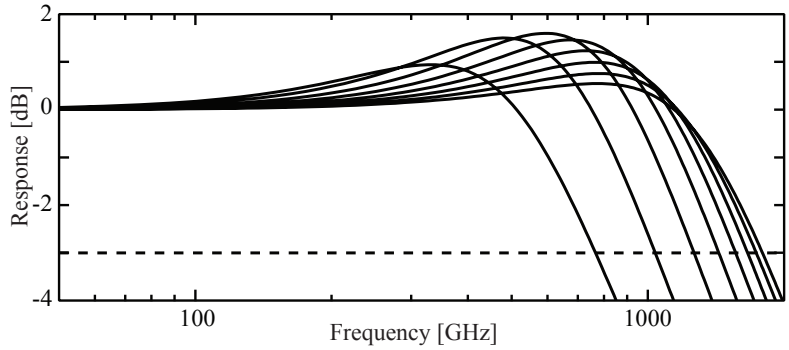

Fig. 2.3: Modulation response curves for different pumps plotted on a dB scale.

response quickly decreases, limiting the maximum modulation frequency. The conventional measure for the bandwidth is where the output is $\frac{1}{2}$ (approx -3dB) of the DC level. This is called the 3dB-bandwidth and is typically in the range of a few GHz for conventional diode lasers [31].

Semiconductor materials are characterized by a forbidden energy gap between the filled valence band and unoccupied conduction band (see figure 2.4a). In equilibrium, most of the electrons occupy the valence band, but through random collision events, electrons can be promoted to occupy higher energy states, leaving behind holes in the valence band. The electrons fill the conduction band, which in bulk semiconductors has a parabolic shape, follow the well-known Fermi-Dirac distribution

$$f = \frac{1}{1 + e^{\frac{E - E_F}{k_B T}}} \tag{2.1}$$

where E_F is the Fermi level, k_B is the Boltzmann constant and T is the temperature. Typically, in semiconductor diodes, the electrons are injected high into the conduction band and thermalize back to the lowest unoccupied conduction band state by the emission of phonons. From here, the electrons can make transitions back to the valence band to recombine with the holes, releasing their energy as photons. The energy of the emitted photons corresponds to the bandgap energy plus the energy of the electron and hole state. As the electrons are being actively injected into the conduction band, the energy distribution of electrons is out of equilibrium and can no longer be described by a single Fermi distribution. Instead, the equilibrium Fermi distribution split up into two quasi Fermi distributions, one for electrons and one for holes. The electron quasi Fermi level will be higher than in equilibrium because more electrons have a high energy, while the hole quasi Fermi level will be lower (see figure 2.4b).

If a thin layer of a semiconductor material is sandwiched between layers of semiconductors with a different bandgap, a 1D potential well for the carriers is formed. If the well is thin enough (on the order of 10 nm), the carriers can

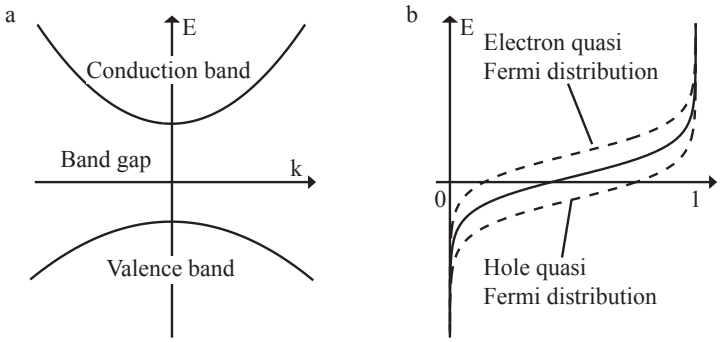

Fig. 2.4: a) The bulk semiconductor have parabolic conduction and valence bands. b) The equilibrium Fermi distribution of electrons split up into a pair of electron and hole quasi Fermi distributions under non-equilibrium conditions.

only occupy discrete quantized energy levels determined as solutions to the Schrödinger equation [31, 34, 35]. This Quantum Well (QW) structure has an electronic Density-Of-States (DOS) that consists of sharp steps at the energy of the quantized states. In between the steps, the electronic DOS is constant as the structure is only confined in one dimension, so that electrons can propagate freely perpendicular to the well. The sharp staircase-like features of the QW, makes it advantageous to use as active material for light emitters as the carriers are concentrated both physically and energetically to a narrow region. Furthermore, the energy levels of the QW can be engineered to a large extent by changing materials and well thickness. This gives the QW laser a very high efficiency (~ 50 % is not uncommon) and great flexibility, so that the majority of all diode lasers today feature one or more QWs.

Quantum Dot (QD) lasers expand on the idea of quantized carrier confinement by using active material that confines the carriers in three dimensions. QD samples are typically formed using self-assembled Stranski-Krastanov growth, which involves depositing mono-layers of one semiconductor material on a substrate of another semiconductor material [36]. If the lattice mismatch between the two materials is large enough, strain effects will force the deposited material to redistribute into isolated islands (or dots), which are energetically favorable. The process is finalized by capping the formed dots by another layer of the substrate material. The Stranski-Krastanov formation of QDs is inherently random and will lead to a distribution of sizes and shapes of the formed QDs. As the quantized energy levels are dependent on the exact dimensions of the QD, this will lead to a distribution of energy levels called the inhomogeneous broadening [37]. The QD 3D confinement results in an electronic DOS that consists of sharp isolated peaks, which gives an even better carrier confinement than in QWs. On the other hand, the nanoscopic dimension of the QDs results in a small overlap of the active volume with the optical mode (compared to e.g. QWs), so that for laser applications, it is necessary to use high QD densities or many layers of QDs.

2.2 Nanoscale Light Emitters

Nanoscale light emitters are different from conventional semiconductor diode lasers in that the size of the confining cavity is comparable to the wavelength of the light. Conventional diodes have relatively large cavities, typically several microns long, that can support many modes each many wavelengths long. Nanocavities characteristically only support a few modes and due to the small length scale, each mode is confined to a volume of a few cubic wavelengths. As the energy of the mode is concentrated in a small volume, the amplitude of the electromagnetic field is increased in a nanocavity. The high field amplitude results in large light-matter interaction, which is determining for the recombination rates. The amount that the recombination rate increases is known as the Purcell factor, which was first described in 1946 by E. M. Purcell [24]. The Purcell enhancement is proportional to the cavity quality factor (Q-factor) divided by the mode volume, V. It can be written as [38]

$$F = \frac{3}{4\pi^2}\frac{Q}{V}\left(\frac{\lambda}{n}\right)^3 = \frac{6}{\pi^2}\frac{Q}{V_n} \tag{2.2}$$

where $V_n = V/\left(\frac{\lambda}{2n}\right)^3$ is the normalized mode volume in half wavelengths cubed and n is the refractive index. The cavity Q-factor is a measure for how fast an optical mode is leaked from the cavity and describes the fact that real cavity modes are always lossy (i.e. they are quasi modes). The Q-factor is defined from the energy dissipation rate of a leaky cavity with center frequency ω_c [39]

$$Q \equiv \omega_c \left|\frac{U}{d_t U}\right| = \omega_c \tau_p \tag{2.3}$$

Here U is the energy and the energy dissipation rate is inversely proportional to the photon lifetime τ_p. Using this definition and assuming that the mode is a decaying harmonic oscillation, the Fourier transform is easily found to be a Lorentzian with a Full Width at Half Maximum (FWHM) of $\frac{\omega_c}{Q} = \frac{1}{\tau_p} = \delta\omega_c$

$$\mathcal{F}\{U(t)\} = \frac{1}{\pi}\frac{\frac{1}{2}\delta\omega_c}{(\omega-\omega_c)^2 + \left(\frac{1}{2}\delta\omega_c\right)^2} \tag{2.4}$$

As the emission spectrum is easily obtained in an experiment, the Q-factor of a cavity is often determined in this way from the FWHM of the measured cavity peak, $\delta\omega$. Depending on what is measured, the Q-factor is then given by

$$Q = \frac{\omega_c}{\delta\omega_c} = \frac{\nu_c}{\delta\nu_c} = \frac{E_c}{\delta E_c} \approx \frac{\lambda_c}{\delta\lambda_c} \tag{2.5}$$

using the standard convention for the relationship between angular and real frequency, wavelength and energy, i.e. $\omega = 2\pi\nu = \frac{E}{\hbar} = \frac{2\pi c}{\lambda}$.

Optical modes are confined to the inside of a cavity and decays evanescently outside and the mode volume is introduced to as a measure of the effective extend of a given mode. It is commonly expressed as [40]

$$V = \frac{\int \varepsilon(\boldsymbol{r})\left|\boldsymbol{\mathcal{E}}(\boldsymbol{r})\right|^2 d\boldsymbol{r}}{\max\left\{\varepsilon(\boldsymbol{r})\left|\boldsymbol{\mathcal{E}}(\boldsymbol{r})\right|^2\right\}} \tag{2.6}$$

where ε is the relative dielectric function and $\boldsymbol{\mathcal{E}}$ is the electric field of the mode. In other words, the mode volume describes the size of the volume necessary to give the total energy of the mode, if the mode had had the energy density $\max\left\{\varepsilon\left(\boldsymbol{r}\right)\left|\boldsymbol{\mathcal{E}}\left(\boldsymbol{r}\right)\right|^2\right\}$ everywhere.

The fact that the recombination rate is enhanced by the Purcell effect, affects the device performance in a number of ways. First, the dynamics is expected to become faster as the conversion from electron-hole pairs to photons becomes faster. Secondly, the β-factor increases as only the spontaneous emission into the cavity mode is enhanced. This means that a smaller number of photons are emitted to the background. Thirdly, by the same argument, the threshold is expected to decrease.

In devices with high Purcell factors, the β-factor can approach unity. This removes the jump at threshold in the I/O curve (c.f. figure 2.2 bottom) giving a seemingly thresholdless laser. However, the name is misleading as even high-β devices still have a pumping regime, where spontaneous emission dominates the recombination. The threshold can be difficult to determine in high-β lasers even for alternative methods, such as linewidth narrowing and the $g^{(2)}$-behavior. Recently, a new approach to determining the threshold of pulsed lasers was suggested by X. Hachair *et al.* [41], which involves studying the phase-space of the photon time evolution. Above threshold, the photon population dynamics becomes faster by the photon number, which leads to a clear, measurable reduction of the phase-space area enclosed by the photon number phase-space trajectory. The phase-space area reduction can be used as an identifier for the transition between spontaneous and stimulated emission and is seen to fit well with experiments [41].

2.3 Types of Nanoscale Optical Confinement

Confinement of light on the wavelength scale requires special techniques and materials, where the electromagnetic environment can be controlled. Below, we describe a number of nanoscale optical confinement techniques, ending up with a description of the photonic crystal cavities that will be used later on.

Total Internal Reflection

A beam of light incident on a planar interface between two uniform and transparent media, medium 1 and 2 with refractive indices of n_1 and n_2, will be partly reflected and partly transmitted. The reflected beam will leave at the same angle as the incident beam (θ_i, relative to the plane normal), while the transmitted (or refracted) beam will leave at an angle (θ_r) determined by Snell's law [42], i.e.

$$n_1 \sin\left(\theta_i\right) = n_2 \sin\left(\theta_r\right) \tag{2.7}$$

Thus, a beam that is transmitted through an interface leaves at an outgoing angle described by eqn. (2.7) (See figure 2.5). For $n_1 > n_2$, the transmitted

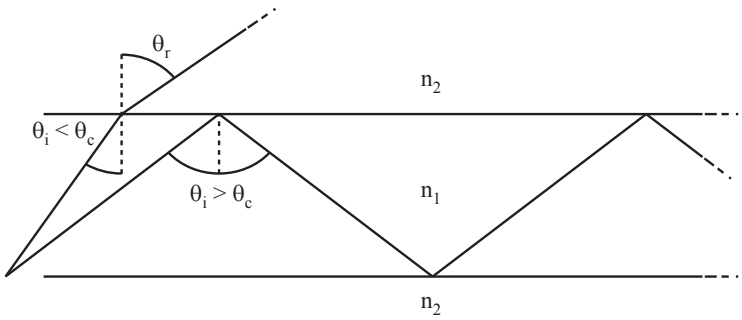

Fig. 2.5: A light beam impinging on a planar interface with an incidence angle less than the critical angle is transmitted through the interface. Another beam with incidence angle greater than the critical angle undergoes total internal reflection and remains inside material 1.

beam will bend away from the interface normal and increasing the angle of incidence will make θ_r approach $\frac{\pi}{2}$. In the special case where the refracted angle is $\frac{\pi}{2}$ eqn. (2.7) describes the critical angle for Total Internal Reflection (TIR) [42], namely

$$\sin(\theta_c) = \frac{n_2}{n_1} \tag{2.8}$$

For $\theta_i > \theta_c$ Snell's law can no longer be fulfilled and the beam is said to undergo total internal reflection, where the transmission coefficient goes to zero. We see from eqn. (2.8) that TIR is only possible if $n_1 > n_2$ as the sine must be less than or equal to 1. Total internal reflection can be used for optical confinement by making a high-index material with parallel interfaces to media with lower refractive index as indicated by figure 2.5. Any beam inside the high-index material, that are propagating at an angle larger than θ_c will be captured inside the high-index material. Indeed, TIR is the underlying principle for light guiding in optical fibers and waveguides as well as in 2D membranized photonic crystals [1, 43] (see below).

Distributed Bragg Reflector

The Distributed Bragg Reflector (DBR) is a 1D periodic structure consisting of layers with alternating refractive indices [31, 44]. For normal incidence, an incoming wave will be partly reflected and transmitted at each layer interface. By choosing the optical thickness of each layer to one quarter of the incident wavelength, the transmitted waves will destructively interfere. A transmitted wave will travel a quarter wavelength, be partly reflected at the next interface with a π phase change and travel another quarter wavelength before returning to the first interface[1]. On the return path, the wave will be π out of phase with the incoming wave which will give destructive interference. The transmitted

[1] More precisely, the reflected field only experiences a π-phase shift at half the interfaces depending on the relative refractive indices.

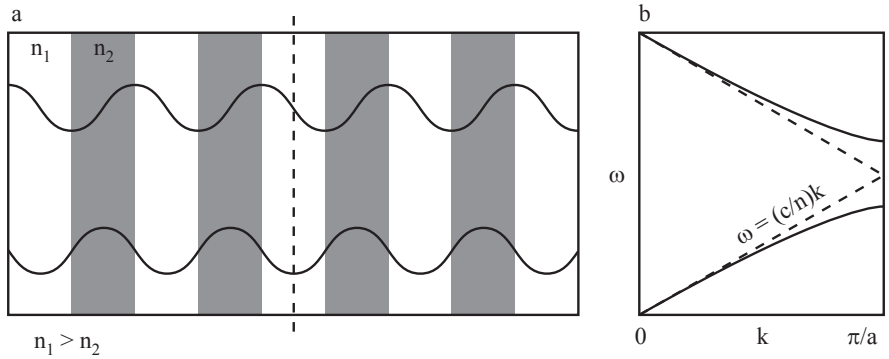

Fig. 2.6: a) A Bragg stack of alternating high (n_1) and low (n_2) refractive index layers. The modes at the Brillouin zone edge are indicated around a symmetry plane (dashed line). b) The dispersion diagram corresponding to the Bragg stack. The dashed line is the dispersion relation for a uniform dielectric.

wave will not be completely suppressed as the reflection at the next interface is not complete, but adding more layers to the structure will lead to a very high total reflection coefficient. The strength of the reflection coefficient is dependent on the refractive index contrast and the number of layers. Typically, 16 layers with an index contrast of 0.5 gives a total reflection coefficient of ≈99.5 % [44]. The strong reflection shows up as a stop-band in the transmission spectrum, i.e. a range of frequencies with nearly zero transmission.

To gain a better understanding of the appearance of the stop-band in this 1D photonic bandgap material, consider figure 2.6a that shows a 1D Bragg stack with lattice constant a and figure 2.6b that shows the dispersion diagram of the Bragg stack. At the edges of the Brillouin zone ($k = \frac{\pi}{a}$) [45], the dispersion diagram deviates from the uniform medium dispersion relation ($\omega = \frac{c}{n}k$) as a bandgap appears where no modes are allowed. At the edge of the Brillouin zone, the modes are standing waves with a wavelength of twice the lattice constant and as the structure is symmetric it is only possible to have the standing waves in two configurations: Either with a node or an anti-node at the symmetry plane In figure 2.6a, the above and below bandgap modes are sketched and we see that one mode have nodes in the low index material and the other in the high index material. The energy of the modes can be calculated from (ignoring the magnetic contribution)

$$U = \frac{1}{2}\int \varepsilon \left|\mathcal{E}\right|^2 dz \tag{2.9}$$

where ε is the dielectric profile. Thus, the mode with nodes in the high index material have a lower energy than the other mode and this produces the bandgap [43].

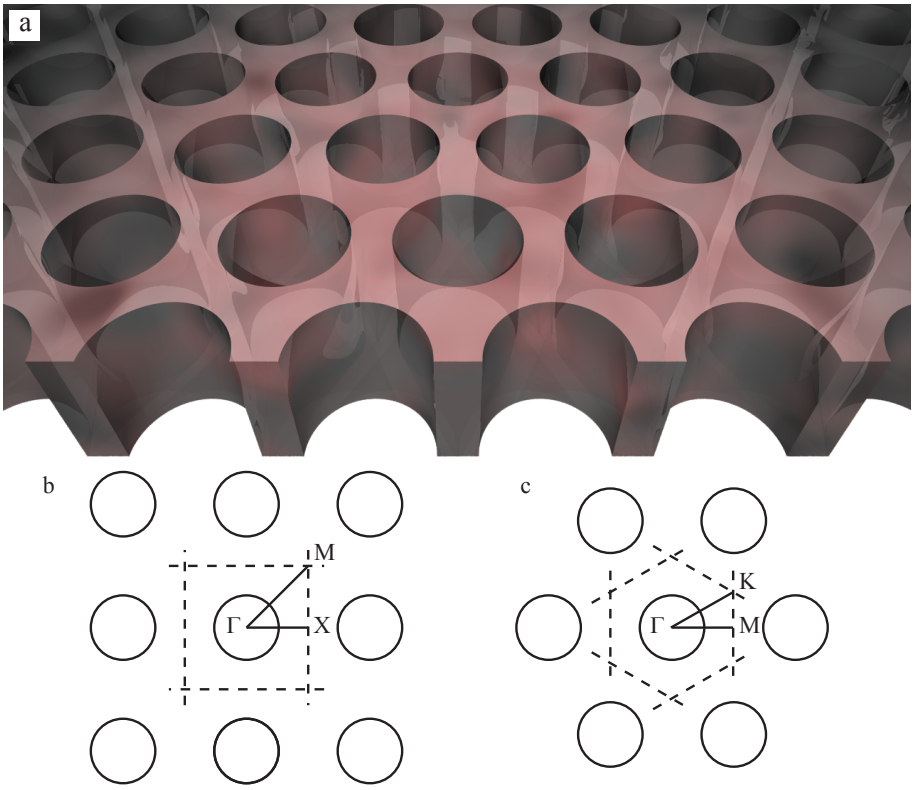

Fig. 2.7: a) An illustration of a 2D photonic crystal. b) The Brillouin zone and symmetry point for a square lattice PhC and c) a hexagonal PhC.

2D Photonic Bandgap Material

Where a DBR can produce a photonic bandgap in one dimension, 2D photonic bandgap materials produce a frequency bandgap in two dimensions. The most straightforward approach is to make a 2D equivalent of the DBR, i.e. concentric circles of transparent materials with alternating refractive indices. However, while this is useful for some applications, e.g. optical cavities with ultra low mode volume [11], such a structure would only produce a bandgap for fields in the center of the structure.

The photonic crystal (PhC) [46–48] is a more general attempt at expanding the DBR to two dimensions. As in the DBR, the PhC consists of a periodic variation of the refractive index, but in the PhC the structure usually consists of low index cylinders (e.g. air holes) in a high index material, see figure 2.7a. Again, the combination of high and low index materials gives rise to high energy and low energy modes that are separated by a photonic bandgap, but in the 2D case the Transverse Electric (TE) modes and Transverse Magnetic (TM) modes behave differently depending on the configuration of the high in-

dex material [43]. TM modes have a bandgap for a structure with isolated spots of high index material, e.g. high index rods in air, while TE modes have a bandgap for structures with connected high index material, e.g. connected veins of high index material [43]. These two seemingly incompatible configurations are combined in the configuration of air holes in a high index material usually employed. It acts as a compromise between the connected and isolated configuration and has a complete photonic bandgap for both TE and TM polarization. Typically, the holes are arranged in two different ways: The square (also called quadratic or rectangular) lattice and the hexagonal lattice. Figures 2.7b and 2.7c show the two hole configurations, the corresponding 1$^{\text{st}}$ Brillouin zone and their high symmetry points.

The 2D photonic crystal can be fabricated using well-known lithographic techniques, but only gives confinement in a plane, while out-of-plane k-vectors can propagate along the direction perpendicular to the plane. For applications, full 3D confinement is desirable, but also difficult to fabricate and this have lead to the development of the membranized photonic crystal, which gives quasi-3D optical confinement. In this structure, a photonic crystal is under-etched to produce a free-standing membrane. This gives TIR confinement in the out-of-plane directions as long as the k-vector is below the critical angle.

This can be seen in another way by considering again the plane interface in figure 2.5. Assuming that $n_1 > n_2 = 1$ and writing a given wave-vector ($\boldsymbol{k}$) in terms of the components parallel ($\boldsymbol{k}_\parallel$) and perpendicular ($\boldsymbol{k}_\perp$) to the interface, we have that

$$k_1^2 = k_{1,\parallel}^2 + k_{1,\perp}^2 \quad \text{(region 1)} \tag{2.10}$$

$$k_2^2 = k_{2,\parallel}^2 + k_{2,\perp}^2 \quad \text{(region 2)} \tag{2.11}$$

where $k^2 = |\boldsymbol{k}|^2$. In region 1, the wavelength is shorter than in region 2 due to the higher refractive index, however, the frequency is conserved, so that $\omega = k_1 v_1 = k_2 c$, where $v_1 = \frac{c}{n_1}$. The parallel component of the k-vector is also conserved across the interface, so that $k_\parallel = k_{1,\parallel} = k_{2,\parallel}$. This yields

$$k_{1,\perp} = \pm\sqrt{\left(\frac{\omega}{v_1}\right)^2 - k_\parallel^2} \quad \text{(region 1)} \tag{2.12}$$

$$k_{2,\perp} = \pm\sqrt{\left(\frac{\omega}{c}\right)^2 - k_\parallel^2} \quad \text{(region 2)} \tag{2.13}$$

From the above equations, we see that for a given $k_\parallel$, the perpendicular component $k_{2,\perp}$ can take on any value for $\omega \geq k_\parallel c$. These are the free radiation modes outside the dielectric material and the region with $k_\parallel < \frac{\omega}{c}$ is called the light cone. For $k_\parallel c \geq \omega \geq k_\parallel v_1$, eqn. (2.13) is imaginary, while eqn. (2.12) remains real. This means that the mode is propagating freely inside the dielectric and only has evanescently decaying perpendicular field components in region 2. For $k_\parallel v_1 \geq \omega$, eqns. (2.12) and (2.13) can no longer be satisfied and no propagating modes exist. This can be summarized as

	Region 1	**Region 2**
$\omega \geq k_{\parallel} c$	Real	Real
$k_{\parallel} c \geq \omega \geq k_{\parallel} v_1$	Real	Imaginary
$k_{\parallel} v_1 \geq \omega$	Imaginary	Imaginary

Thus, only k-vectors in the dielectric with parallel components larger than the light-line (defined by $k_{\parallel} = \frac{\omega}{c}$) are confined inside the structure.

In PhC cavities, the mode volume is typically on the order of several cubic half-wavelengths, because the confinement is due to interference effects of the field scattering of the holes. Mode volumes approaching $1\left(\frac{\lambda}{2n}\right)^3$ have been achieved in PhCs [49] and even sub-wavelength confinement is possible ($\approx 10^{-2}\left(\frac{\lambda}{2n}\right)^3$) [50].

Photonic Crystal Cavity Designs

In photonic crystals, a cavity is formed by a disturbance of the otherwise perfectly regular hole lattice. The disturbance creates a region in the PhC, where light is allowed to propagate, however the region is surrounded by regular PhC, which is impenetrable for light (in the frequency range of the stopband). As the hole lattice can be fabricated with high precision of the hole locations, the confinement can become arbitrarily strong in the in-plane direction and the main loss mechanism is out-of-plane loss. Design of optical cavities with high Q and low mode volume involves adjusting the size and position of individual holes and a large number of different cavity designs can therefore be realized [20, 51–55]. A full treatment is beyond the scope of the present work and we therefore focus a few interesting examples.

One of the simplest cavity designs involves the removal of a single hole in the lattice and is called the H1 cavity. In a rectangular PhC lattice, this produces a cavity that support modes with a strong confinement in the ΓX-direction, which supports the formation of doubly degenerate dipole modes and quadrupole modes [43]. The dipole mode consists of two lobes in the ΓX-direction, which are π out-of-phase and have a node in the cavity center. The quadrupole mode has a four-lobed structure with lobes in the ΓM-direction and a central node.
In hexagonal lattices, the H1 cavity is 60° rotational symmetric, so that the dipole mode is three times degenerate. A hexapole mode (six lobes) is supported in lieu of the quadrupole mode. Both lattices support additional mode, e.g. monopole modes (single central antinode) at low frequencies, but dipole, quadrupole and hexapole modes have high Q and lie inside the stopband of the structures studied later on.

A more complicated cavity structure is represented by the Noda cavity [51], which is based on the L3 cavity, where three on-axis holes have been removed from a hexagonal PhC. Noda *et al.* argued that the out-of-plane loss was due to k-vectors lying within the light cone and that in order to maximize the Q-factor, the k-space distribution should be engineered to exclude k-vectors below

the critical angle. The group showed that the appearance of k-vectors within the light cone, was partially due to the abrupt termination of the cavity and that a more gradual termination of the defect region would lead to better confinement (light should be "confined gently in order to be confined strongly"). Gentle confinement in the Noda cavity was achieved by adjusting the position of the innermost of the on-axis holes slightly away from the cavity. This modification improved the Q-factor by roughly 15 times to about 45000.

A major practical problem for the design of active nanocavity devices lies in the heating of the structure. Typically, only a fraction of the pump power is emitted as useful radiation, while the rest is lost, mainly as heat. The heating of the sample, changes the refractive index of the materials, so that the optical cavity mode is detuned from the laser frequency. Thus, for too high pump, the output power will decrease and in extreme cases will also damage the sample. This is especially a problem for membranized PhCs because the surrounding air has poor heat conduction. For devices with QWs as the active material, part of the problem is that QWs extend outside the optical cavity. Because it is difficult to focus the excitation power, the part of the QWs outside the cavity is also pumped, which generate additional heating. This prompted Notomi *et al.* [21] to fabricate a PhC laser featuring a "buried heterostructure", i.e. a QW that was restricted to a small volume ($4 \times 0.3 \times 0.15$ μm). With this design, the refractive index change of the buried heterostructure acted as an optical cavity, so that the overlap of the optical mode with the excited carrier population was large, i.e. carriers where only excited inside the optical cavity, where recombination lead to useful output. Furthermore, the PhC membrane was fabricated using a InP, which has a 10 times higher thermal conductivity than InGaAsP, which is usually employed. With this promising design, the group demonstrated lasing with a quantum efficiency of 50 % and modulation speeds of 20 GHz at 8.8 fJ/bit.

3. SEMICONDUCTOR LASER MODELING

When investigating laser systems it is necessary to decide on a suitable model. The model should be simple enough to avoid unnecessary complications and still be accurate enough to reproduce all important effects. Nanolaser modeling is still a relatively new topic and it is important to get an understanding of the general behavior of the processes involved. Rather than trying to include every detail of the nanolaser system in a complicated model, we emphasize easy analyzability in order to understand the trends involved. We therefore modify the well-known semiconductor laser rate equations to include the important specifics of nanolasers. The aim is a familiar and readily usable model, where the characteristics of the nanocavity are included as modifications to the laser rate equation terms.

This chapter begins with a summary of the laser rate equations that are used to model conventional semiconductor laser devices and a discussion of the required modifications in order to expand the scope to nanocavity devices. In section 3.2 and 3.3, we derive expressions for the recombination rates and construct the optical and electronic density-of-states. The general characteristics of the modified recombination rates are examined in section 3.4 and 3.5 and the effect of the Purcell effect is discussed. Section 3.6 lists the full model that will be used in the following chapters and in section 3.7, we outline a microscopic theory that will be used as the basis for comparison in section 4.5.

3.1 Laser Rate Equations

The starting point for the model is the Laser Rate Equations (LREs) which have been used extensively and successfully for modeling semiconductor diode lasers. The LRE is a single mode theory that can be derived from e.g. the density matrix equations by assuming that the polarization can be adiabatically eliminated. The distribution of carriers is described by a single quantity, the carrier density (N), which is available for recombination at the laser transition. The photon density (P) describes the occupation of the laser mode and this allows for a description in terms of rates going into and out of the carrier and photon reservoirs (see schematic in figure 3.1). Following ref. [31], the LREs take the form (c.f. figure 3.1)

$$\dot{N} = J - R_{nr} - R_c - R_b - R_{st} \tag{3.1}$$

$$\dot{P} = \Gamma R_c + \Gamma R_{st} - R_p \tag{3.2}$$

Here the symbols are as follows:

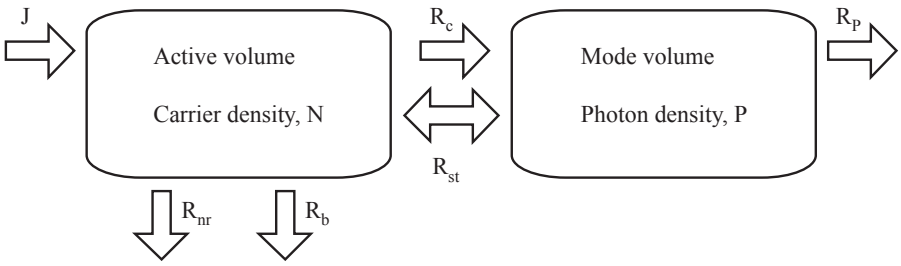

Fig. 3.1: Schematic showing the rates in and out of the laser system in the LREs.

J The carrier injection current density, J, describes the number of carriers per volume that are injected into the active area per time. For electrical pumping, J can be replaced by $\frac{\eta_i I}{V_a q}$, where I is the current at the terminals, V_a is the active volume, q is the charge of the carriers and η_i is the internal quantum efficiency, which describes the fraction of the current at the terminals that generate carriers in the active volume. For optical pumping, the carriers are usually generated by off-resonant pumping, i.e. at a shorter wavelength, so that carriers must first relax into the lowest excited state. In this case, $J = \frac{\eta_e \eta_i P_{in}}{\hbar \omega_{in} V_a}$, where P_{in} is the pump laser output effect, $\hbar\omega_{in}$ is the energy per pump photon and η_e is the external efficiency, i.e. the fraction of P_{in} that generates carriers in the pump level. Now, η_i describes the fraction of the pump carriers that are captured into the lowest excitable energy state in the active region.

R_{nr} The term R_{nr} describes the rate of non-radiative recombination, which usually includes the surface recombination and Auger recombination process. In surface recombination, carriers can recombine via surface states, which mainly appears at interfaces to air, where the termination of the crystal lattice produce dangling bonds. The surface recombination rate is proportional to the ratio of the exposed active area, a_s, to the active volume and is relatively more important for small structures, where this ratio becomes large. For high carrier densities the surface recombination rate is given by $\frac{a_s}{V_a} v_s N = A_s N$, where v_s is the surface recombination velocity and A_s is the surface recombination coefficient.
Auger recombination involves the scattering of two carriers on each other, which sends one to the valence band and the other to a higher conduction band state. The process is dependent on more than one particle and is therefore more important at high carrier densities. The Auger recombination rate can be written $R_A = CN^3$, where C is a constant.
To the non-radiative recombination processes also belongs the defect recombination, which can become important if the active material has many defects, i.e. crack dislocations, dopant atoms or voids. In this type of process, the carriers can recombine via dangling bonds in the material, that is, at defect sites where there is a mismatch of the bonding orbitals. However, with modern growth techniques, the defect recombination pro-

cess is negligible.

R_c and R_b The total spontaneous recombination rate, $R_{sp} = R_c + R_b$, consist of a contribution from the spontaneous emission into the cavity mode, R_c, and into all other modes, R_b. Spontaneous emission requires the presence of both an electron and a hole and is therefore proportional to carrier density squared, $R_{sp} = BN^2$. The proportionality constant, B, is known as the bimolecular recombination coefficient. The spontaneous emission rate is sometimes linearized as $R_{sp} \approx \frac{N}{\tau_{sp}}$, where $\frac{1}{\tau_{sp}} = BN_{th}$ is the spontaneous emission lifetime at threshold. This approximation is reasonable for lasing devices as the carrier density clamps at threshold. The emission into the cavity is described as a fraction of the total spontaneous emission by the spontaneous emission factor, β, i.e. $R_c = \beta R_{sp}$ and thus $R_b = (1 - \beta) R_{sp}$. Although the recombination in general is a two-particle process (presence of both electron and hole required), giving a N^2 dependence on the carrier density, the electrons and holes can form excitons at low temperatures, which recombine as N^1. The same can happen in QDs, where the electrons and holes are captured by the QDs so that they are spatially localized. The recombination is then monomolecular unless the capture time into the QD is long or the carrier density is low.

R_{st} The stimulated recombination rate is noted by the term R_{st} and is proportional to the photon density and the gain, G, i.e. $R_{st} = GP$. The gain can be approximated by a logarithmic relation as $G = v_g G_0 \ln\left(\frac{N+N_s}{N_{tr}+N_s}\right)$, where v_g is the group velocity, G_0 the material gain, N_{tr} the transparency carrier density and N_s is a small parameter to keep the gain finite for $N \ll N_{tr}$. The logarithmic gain can be linearized around the transparency carrier density to give $G \approx \frac{v_g G_0}{N_{tr}+N_s}(N - N_{tr}) = a(N - N_{tr})$, where a is the differential gain. For operation of the laser far above threshold, the stimulated emission process can become so fast that the carrier distribution is depleted around the transition energy. This is known as spectral hole burning and leads to a reduction of the stimulated emission rate. This effect is modeled in the LREs by multiplying the expression for the gain by a factor proportional to the photon density, $\frac{1}{1+\epsilon_{SHB}P}$. Here ϵ_{SHB} is a parameter that governs the onset of spectral hole burning.

R_p The term R_p denotes the photon escape rate and is usually written as $R_p = \frac{P}{\tau_p}$, where τ_p is determined from the cavity Q-factor, i.e. eqn. (2.3).

Γ The confinement factor, Γ, appears as a result of the carrier density being normalized to the active volume, whereas the photon density is normalized to the mode volume. The volume mismatch defines the confinement factor $\Gamma = \frac{V_a}{V}$.

When treating nanocavity devices, the above expressions must be modified to incorporate the characteristics of tight confinement. Most notably among these are the correct treatment of the β-factor and the Purcell enhancement, which affects the recombination rates. For conventional diodes, where the cavities can support many modes, the β-factor is roughly equal to one over the number

of modes. However, this definition breaks down for nanocavity devices, where only one mode is inside the photonic bandgap. In this case, β is better defined as

$$\beta = \frac{R_c}{R_c + R_b} \tag{3.3}$$

However, this definition requires detailed knowledge of R_c and R_b and it is generally dependent on the carrier density as well as the exact form of the electronic and optical DOS. In a nanocavity, we expect R_c to be enhanced by the Purcell factor, so that β increases towards unity. Thus, a first guess at a modified spontaneous recombination expression is simply to introduce the Purcell factor into the expression for spontaneous emission in a conventional diode ($\frac{N}{\tau_{sp}}$) and adjust β to a constant value close to 1 [12, 26], i.e.

$$R_c = \beta F B N^2 \approx \beta F \frac{N}{\tau_{sp}} \qquad \text{(Simple model)} \tag{3.4}$$

$$R_b = (1-\beta)\, B N^2 \approx (1-\beta)\, \frac{N}{\tau_{sp}} \qquad \text{(Simple model)} \tag{3.5}$$

where only emission going into the cavity mode is enhanced by the Purcell factor F. Equations (3.4) and (3.5) have been used recently to investigate the dynamical properties of nanocavity devices [26] and we will refer to them as the simple model, which we will use for comparison later on. Note that the approximations on the right hand side of eqns. (3.4) and (3.5) are valid for QWs close to threshold where the carrier density clamps. In this case, the spontaneous recombination can be written $BN^2 \approx BN_{th}N = 1/\tau_{sp}N$. This approximative form of the recombination rate is useful for simplifying analytical expressions for the behavior of QW devices near threshold.

With modern cavity designs, F can become a very large number (Q-factors reaching into the millions have been reported for PhC cavities [56]) and the spontaneous emission contribution to the total recombination rate therefore also becomes an increasingly larger factor. The below threshold operation thus becomes more important and it has even been suggested that the largest modulation bandwidths are found in this pumping regime [26]. In this scenario, eqns. (3.4) and (3.5) are no longer sufficient to faithfully model the nanocavity system and we therefore in the following sections develop expressions for recombination rates that include details about the electronic and optical density-of-states. This also allows for a separate calculation of R_c and R_b, so that we can abandon the concept of a spontaneous emission factor altogether.

3.2 Einstein's Approach to Radiative Recombination

With offset in the conventional LRE theory, outlined above, we now derive the radiative recombination rates from the Einstein A and B coefficients. The rates can be expressed following Einstein's approach to radiative recombination, where the upwards and downwards transitions are written in terms of

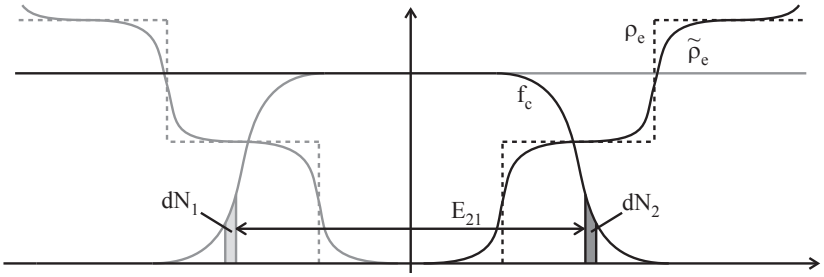

Fig. 3.2: Schematic showing the quasi Fermi functions and the regular and homogeneously broadened electronic density-of-states.

proportionality constants as [31]

$$dR_{sp}^{21} = AdN_2 \tag{3.6}$$
$$dR_{st}^{21} = BW(\nu)\, dN_2 \tag{3.7}$$
$$dR_{st}^{12} = BW(\nu)\, dN_1 \tag{3.8}$$

where the rates are differential as we are considering transitions between the continuous semiconductor conduction (N_2) and valence (N_1) band carrier densities. The term W is the radiation spectral density and the superscripts 21 and 12 separates stimulated emission and absorbtion. The coefficients A and B are associated with the spontaneous and stimulated emission, respectively, and can be shown to be related by

$$A = \rho_o(\nu)\, h\nu B \tag{3.9}$$

where ρ_o is the optical DOS. The differential occupation of the conduction (dN_2) and valence (dN_1) band can be written in terms of the quasi Fermi functions for the conduction and valence band (f_c and f_v) and the reduced electronic DOS for the electron-hole transition pairs (ρ_e)

$$dN_2 = f_c(E_{21})(1 - f_v(E_{21}))\, \rho_e(E_{21})\, L(E_{21} - h\nu)\, dh\nu dE_{21} \tag{3.10}$$
$$dN_1 = f_v(E_{21})(1 - f_c(E_{21}))\, \rho_e(E_{21})\, L(E_{21} - h\nu)\, dh\nu dE_{21} \tag{3.11}$$

The equations express that the carrier density available for recombination within a certain differential energy interval (E_{21} to $E_{21} + dE_{21}$) is proportional to the electronic DOS and the availability of electrons and holes (see figure 3.2). The last term $L(E_{21} - h\nu)$ is the homogeneous broadening, which models the broadening of the energy levels due to phonon interactions. It can be taken to be a Lorentzian with a FWHM equal to the homogeneous linewidth, γ, i.e.

$$L(E_{21} - h\nu) = \frac{1}{\pi} \frac{\frac{\gamma}{2}}{(E_{21} - h\nu)^2 + \left(\frac{\gamma}{2}\right)^2} \tag{3.12}$$

Inserting eqns. (3.10) and (3.11) in eqns. (3.6) - (3.8) and integrating, we have

$$R_{sp} = \int\int A f_c\left(E_{21}\right)\left(1 - f_v\left(E_{21}\right)\right)\rho_e\left(E_{21}\right) L\left(E_{21} - h\nu\right) dh\nu dE_{21} \quad (3.13)$$

$$R_{st}^{21} = \int\int BW\left(h\nu\right) f_c\left(E_{21}\right)\left(1 - f_v\left(E_{21}\right)\right)\rho_e\left(E_{21}\right) \times L\left(E_{21} - h\nu\right) dh\nu dE_{21} \quad (3.14)$$

$$R_{st}^{12} = \int\int BW\left(h\nu\right) f_v\left(E_{21}\right)\left(1 - f_c\left(E_{21}\right)\right)\rho_e\left(E_{21}\right) \times L\left(E_{21} - h\nu\right) dh\nu dE_{21} \quad (3.15)$$

Assuming that the Fermi functions vary slowly compared to the rest of the terms, we can pull them out of the integral over E_{21} and define the homogeneously broadened electronic DOS (see figure 3.2)

$$\tilde{\rho}_e\left(h\nu\right) = \int \rho_e\left(E_{21}\right) L\left(E_{21} - h\nu\right) dE_{21} \quad (3.16)$$

With the net stimulated emission rate, $R_{st} = R_{st}^{21} - R_{st}^{12}$ and the assumption $f_c = 1 - f_v$, we then have

$$R_{sp} = \int A f_c^2\left(h\nu\right)\tilde{\rho}_e\left(h\nu\right) dh\nu \quad (3.17)$$

$$R_{st} = \int BW\left(h\nu\right)\left(2 f_c\left(h\nu\right) - 1\right)\tilde{\rho}_e\left(h\nu\right) dh\nu \quad (3.18)$$

which we will use for calculation of the spontaneous and stimulated emission[1]. In the next section, we specify the terms appearing in the integrals for the recombination rates.

3.3 Optical and Electronic Density of States

In order to proceed any further, we need to specify the details of the electronic DOS and the Einstein coefficients. For the electronic DOS, we will specify ρ_e for a QW and QD system. The QW electronic potential well can be approximated by an infinite-potential barrier, which gives simple expressions for the energy levels [31]. In this approximation the energy levels are given as

$$E_m = m^2 \frac{\hbar^2 \pi^2}{2 m_e^* \ell^2}, \qquad m \in \mathbb{Z}^+ \quad (3.19)$$

where m_e^* is the effective electron mass and ℓ is the QW thickness. From eqn. (3.19) and the phase-space density for a QW, the electronic DOS can be

[1] Notice, that this model assumes bimolecular recombination, which is not always correct for QDs, where the spatially confined electron-hole pairs can recombine as a monomolecular process. This is an issue at large carrier density, but typically the carrier density clamps at threshold so that the error made by using a bimolecular model, rather than the monomolecular equivalent, is small. Furthermore, the exact dependence on the carrier density (N or N^2) will not affect the results and conclusions drawn later on. Therefore, we will use the bimolecular expression for QD recombination.

shown to be [31]

$$\rho_e^{QW}(E) = \frac{m_e^*}{\pi\hbar^2\ell}\sum_m \Theta(E - E_m) \tag{3.20}$$

where the $\Theta(\cdot)$ is the Heaviside step function [57]. An example QW electronic DOS is shown in figure 3.3a. To form the homogeneously broadened QW electronic DOS, we apply eqn. (3.16) together with eqn. (3.12) and find

$$\begin{aligned}\tilde{\rho}_e^{QW}(h\nu) &= \int \rho_e^{QW}(E_{21})\, L(E_{21} - h\nu)\, dE_{21} \\ &= \frac{m^*}{\pi\hbar^2\ell}\sum_m \int_{E_m}^{\infty} \frac{1}{\pi}\frac{\frac{\gamma}{2}}{(E_{21} - h\nu)^2 + \left(\frac{\gamma}{2}\right)^2} dE_{21} \\ &= \frac{m^*}{\pi\hbar^2\ell}\sum_m \left(\frac{1}{2} + \frac{1}{\pi}\arctan\left(\frac{h\nu - E_m}{\frac{\gamma}{2}}\right)\right)\end{aligned} \tag{3.21}$$

where we replaced m_e^* with the reduced effective mass $m^* = \frac{m_e^* m_h^*}{m_e^* + m_h^*}$ as eqn. (3.16) uses the reduced electronic DOS. At first glance, the sum seems to diverge, however, for the energy levels, E_m, far above the relevant photon energy, $h\nu$, $\frac{1}{\pi}\arctan\left(\frac{h\nu - E_m}{\gamma/2}\right) \to -\frac{1}{2}$, so that sum remains finite.

For QD materials, the electronic DOS for a single QD is found simply as the number of electronic states divided by the volume of the dot, V_{QD}. If we consider only the lowest electron energy level (the s-state), which can hold a spin-up and a spin-down electron, we have

$$\rho_e^{QD,1}(E) = \frac{2}{V_{QD}}\delta(E - E_{QD}) \tag{3.22}$$

Here $\delta(E - E_{QD})$ is the Dirac delta function, that ensures that the transition only occur at the lowest QD level energy, E_{QD}. As mentioned in section 2.1, the size and shape of the QDs vary in realistic systems due to the inherent randomness of the fabrication process, which lead to a variation of the energy levels. For a large enough QD ensemble this will lead to an apparent broadening of the QD linewidth known as inhomogeneous broadening. The random origin makes it possible to model the inhomogeneous broadening for large number of QDs (N_{QD}) as a Gaussian distribution with width given by σ as

$$L_{inhom}(E) = \frac{1}{\sqrt{2\pi\sigma^2}} e^{-\frac{(E-E')^2}{2\sigma^2}} \tag{3.23}$$

Thus the inhomogeneously broadened QD electronic DOS is the convolution of eqns. (3.22) and (3.23), i.e.

$$\begin{aligned}\rho_e^{QD,inhom}(E) &= \frac{2}{V_{QD}}\int \frac{1}{\sqrt{2\pi\sigma^2}} e^{-\frac{(E-E')^2}{2\sigma^2}}\delta(E' - E_{QD})\, dE' \\ &= \frac{2}{V_{QD}}\frac{1}{\sqrt{2\pi\sigma^2}} e^{-\frac{\left(E-E_{QD}\right)^2}{2\sigma^2}}\end{aligned} \tag{3.24}$$

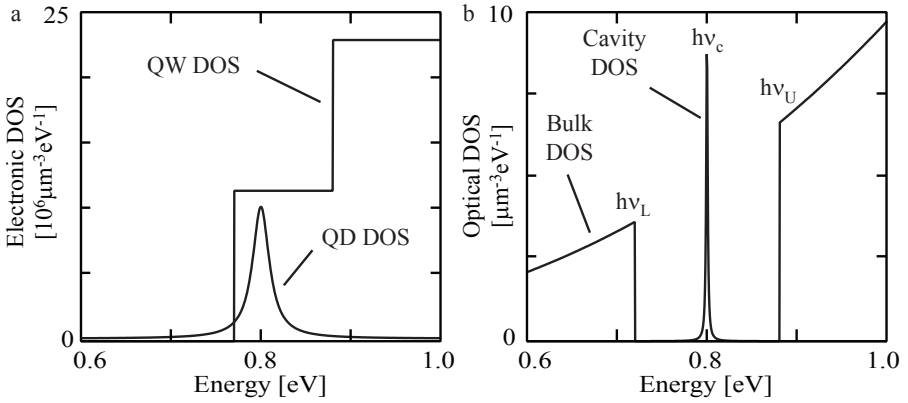

Fig. 3.3: a) The electronic DOS for a QW and QD device. b) The optical DOS for a PhC cavity. The bulk background have a bandgap between $h\nu_L$ and $h\nu_U$ and a Lorentzian shaped cavity is centered at $h\nu_c$.

An example QD electronic DOS is shown in figure 3.3a. To form the homogeneously broadened QD electronic DOS, we again apply eqn. (3.16) and find

$$\tilde{\rho}_e^{QD}(h\nu) = \frac{2}{V_{QD}} F_V(h\nu - h\nu_{QD}, \gamma, \sigma) \tag{3.25}$$

where F_V is the Voigt function defined as [58]

$$\begin{aligned} F_V(x,\gamma,\sigma) &= \int \frac{1}{\sqrt{2\pi\sigma^2}} e^{-\frac{y^2}{2\sigma^2}} \frac{1}{\pi} \frac{\frac{\gamma}{2}}{(x-y)^2 + \left(\frac{\gamma}{2}\right)^2} dy \\ &= \frac{\mathrm{Re}\{w(z)\}}{\sqrt{2\pi\sigma^2}} \end{aligned} \tag{3.26}$$

As indicated in the last line, the Voigt function can be evaluated in terms of the complex error function, $w(z)$, where $z = \frac{x+i\gamma}{\sqrt{2\sigma^2}}$ [58]. Alternatively, the Voigt function can be evaluated by approximating the Gaussian distribution with a Lorentzian with the same FWHM, $\sigma' = 2\sqrt{2\ln(2)}\sigma$, and carrying out the integration in eqn. (3.26)

$$\begin{aligned} F_V(h\nu - h\nu_{QD}, \gamma, \sigma) &\approx \int \frac{1}{\pi} \frac{\frac{\sigma'}{2}}{(E - h\nu_{QD})^2 + \left(\frac{\sigma'}{2}\right)^2} \frac{1}{\pi} \frac{\frac{\gamma}{2}}{(E - h\nu)^2 + \left(\frac{\gamma}{2}\right)^2} dE \\ &= \frac{1}{\pi} \frac{\frac{\gamma}{2} + \frac{\sigma'}{2}}{(h\nu - h\nu_{QD})^2 + \left(\frac{\gamma}{2} + \frac{\sigma'}{2}\right)^2} \end{aligned} \tag{3.27}$$

This is just another Lorentzian with the effective FWHM of $\frac{\gamma+\sigma'}{2}$.

In bulk, the Einstein A coefficient can be taken to be inversely proportional to the spontaneous recombination lifetime in bulk at a certain frequency, ν_{21} [31]

$$A_{21} = \frac{1}{\tau_{21}} \tag{3.28}$$

which means that the Einstein B coefficient is given by eqn. (3.9) as

$$\frac{1}{\tau_{21}} = \rho_o^{bulk}(\nu_{21})\, h\nu_{21} B$$
$$B = \frac{1}{\tau_{21}\rho_o^{bulk}(\nu_{21})\, h\nu_{21}} \tag{3.29}$$

where ρ_o^{bulk} is the bulk optical DOS given by [31]

$$\rho_o^{bulk}(\nu) = \frac{8\pi n^3}{c^3}\nu^2 \tag{3.30}$$

Using eqn. (3.29) to fix the Einstein B coefficient, we can determine the A coefficient from the optical DOS through eqn. (3.9) as

$$A = \rho_o(\nu)\, h\nu B = \frac{1}{\tau_{21}} \frac{h\nu}{h\nu_{21}} \frac{\rho_o(\nu)}{\rho_o^{bulk}(\nu_{21})} \tag{3.31}$$

For PhC bandgap materials, the optical DOS can be taken approximatively as a bulk background optical DOS with a photonic bandgap, i.e.

$$\rho_o^{PhC}(\nu) = \rho_o^{bulk}(\nu)\left[\Theta(\nu_L - \nu) + \Theta(\nu - \nu_U)\right] \tag{3.32}$$

where ν_L and ν_U are the lower and upper edge of the bandgap (see figure 3.3b). Note that we for simplicity neglect the sharp band edge features that appear as a consequence of the sum-rule for the DOS. As we shall see later, these do not influence the emission going into the cavity and therefore do not change the conclusions drawn in section 3.4. Note also that most PhCs do not have a complete bandgap for both TE and TM modes[2]. In the present work only TE-bandgap PhCs are studied and the optical DOS in figure 3.3b therefore refers to this polarization and it is assumed that the active material emits TE polarized light[3]. Materials emitting in more than one polarization can effectively be modeled by including a bandgap floor in the optical DOS, i.e. an imperfect bandgap. Inclusion of a bandgap floor would give rise to a larger emission to other modes than the cavity mode (R_b), mimicking the expected behavior as emission to other polarizations would be lost. Inserting eqn. (3.32) in eqn. (3.31) gives

$$A_{PhC} = \frac{1}{\tau_{21}} \left(\frac{\nu}{\nu_{21}}\right)^3 \left[\Theta(\nu_L - \nu) + \Theta(\nu - \nu_U)\right] \tag{3.33}$$

Introduction of a cavity into the center of the bandgap can be modeled in a similar way by a Lorentzian with a FWHM corresponding to the cavity quality factor (c.f. eqn. (2.4)). The lifetime at the spectral maximum of the cavity should equal the bulk lifetime at the same frequency times the enhancement

[2] An exception is triangular lattice PhCs with high filling factors, where the bandgap for TE and TM modes overlaps [43]

[3] For QWs the polarization of the emitted light can be controlled via the strain as the light-hole valence band (favoring TE polarized emission) experiences a larger shift than the heavy-hole band (favoring TM polarized emission) when the material is strained [59].

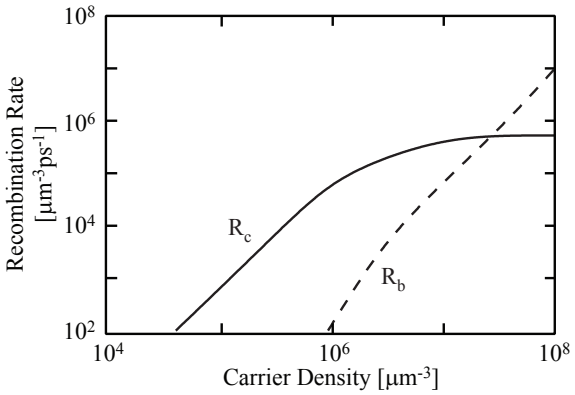

Fig. 3.4: The cavity spontaneous emission, R_c, and background spontaneous emission, R_b, calculated for a quantum well device in the full model. *Parameters in table E.1.*

due to the Purcell effect [24, 38]. Therefore, the Einstein A coefficient for a PhC cavity system can be written as (choosing $\nu_{21} = \nu_c$, so that τ_{21} is the recombination time in bulk at the cavity frequency)

$$A = \frac{1}{\tau_{21}} \left[\left(\frac{\nu}{\nu_c} \right)^3 \left[\Theta\left(\nu_L - \nu\right) + \Theta\left(\nu - \nu_U\right) \right] + \frac{F\left(\frac{1}{2}\delta\nu_c\right)^2}{\left(\nu - \nu_c\right)^2 + \left(\frac{1}{2}\delta\nu_c\right)^2} \right] \quad (3.34)$$

where $h\delta\nu_c = \hbar\delta\omega_c = \delta E_c = \frac{E_c}{Q}$. The optical DOS for a PhC cavity is shown in figure 3.3b. Note that the lifetime in bulk, τ_{21}, is at the specific frequency, ν_c, and must be chosen, so that the total spontaneous emission lifetime in bulk, τ_{sp} is recovered when using a bulk DOS.

3.4 Spontaneous Emission

With the electronic DOS and the Einstein A coefficient defined in eqns. (3.21), (3.25) and (3.34), we can now calculate the spontaneous emission rate for a nanocavity QW or QD device using eqn. (3.17). Examining first the QW device, we use the electronic DOS given in eqn. (3.21) and calculate the spontaneous emission rate as a function of carrier density. The result is shown in figure 3.4 for the spontaneous emission going into the cavity (cavity emission) and into all other modes (background emission).

For low carrier densities, we see that the cavity emission is proportional to $\propto N^2$ and that R_b is negligible, but for $N \gtrsim N_{tr}$, the cavity emission levels off and instead the background emission increases sharply. This can be understood from the relative positions of the cavity resonance, the photonic bandgap edges and the QW states, which can be seen from figure 3.3. For low carrier densities, the quasi Fermi level separation is smaller than the cavity resonance and as the optical DOS is zero in the photonic bandgap, the contribution to the

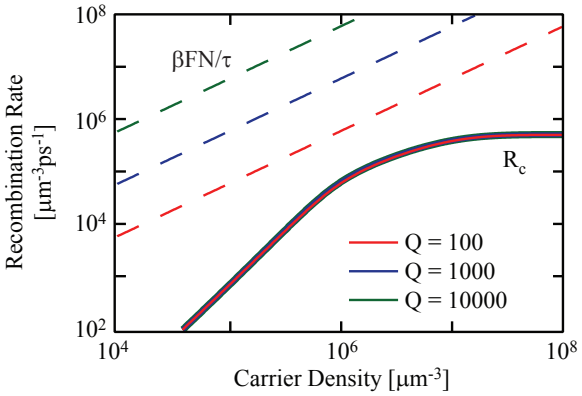

Fig. 3.5: The cavity spontaneous emission, R_c, calculated for a quantum well device in the full and the simple model for three different Q-factors. Note that the three curves for the full model lies on top of each other. *Parameters in table E.1.*

background emission can only come from the tail of the quasi Fermi function. Therefore, the R_b is very low for low carrier densities. At high carrier densities, the quasi Fermi level separation moves far above the cavity resonance, so that $f_c(h\nu_c) \approx 1$. This means that increasing the carrier density further, will not further increase the cavity emission and R_c levels off. The background emission on the other hand increases sharply as the quasi Fermi function now has a significant value above $h\nu_U$.

In figure 3.5, we compare the spontaneous cavity emission calculated in the full (eqn. (3.17)) and simple model (eqn. (3.4)) for three different Q-factors. The figure underlines the importance of correct modeling of spontaneous emission in nanocavities as R_c is markedly different in the two models. Of special interest is the Purcell enhancement, which in the simple model increases R_c linearly with the Q-factor. In the full model, however, we notice that all three curves lie on top of each other, which means that R_c apparently is independent of the Q-factor in this case. This can be understood from an approximate expression for the spontaneous emission.

Consider the spontaneous emission into the cavity, eqn. (3.17). For QWs and high Q cavities, we can assume that the optical DOS is varying faster than both the quasi Fermi functions and the electronic DOS. We then have

$$\begin{aligned} R_c &\approx f_c^2(h\nu_c)\,\tilde{\rho}_e(h\nu_c)\,\frac{F}{\tau_{21}}\int \frac{\left(\frac{1}{2}\delta\nu_c\right)^2}{(\nu-\nu_c)^2+\left(\frac{1}{2}\delta\nu_c\right)^2}dh\nu \\ &= f_c^2(h\nu_c)\,\tilde{\rho}_e(h\nu_c)\,\frac{F}{\tau_{21}}\pi\frac{\nu_c}{2Q} \\ &= \frac{1}{\tau_{21}}\frac{3\nu_c}{\pi V_n}f_c^2(h\nu_c)\,\tilde{\rho}_e(h\nu_c) \end{aligned} \tag{3.35}$$

Here, we see that because the cavity line width is narrow compared to the electronic DOS (and the quasi Fermi function), the integral is effectively over the Lorentzian shaped cavity. This integral is proportional to Q^{-1} which cancels the Q in the Purcell factor and makes eqn. (3.35) independent of the cavity quality factor. This means that increasing the quality factor above the point where the cavity optical DOS becomes delta-like compared to the electronic DOS, will not change the spontaneous emission rate [49, 50, 60]. This result is very important for understanding the behavior of nanolasers and is markedly different from the behavior of the simple model, which does not feel this type of reduction of the Purcell enhancement. Note that even though the spontaneous emission rate becomes independent of the Q-factor, R_c is still dependent on the mode volume and the Purcell enhancement can be affected through V. The reduction of the Purcell enhancement stems from the optical DOS being sharply peaked compared to electronic DOS, therefore any sharp features in the electronic DOS near the optical DOS maximum will soften the reduction of the Purcell enhancement. Such sharp features can arise in quantum wells e.g. at low temperatures, where the electrons and holes can form excitons, that appear as sharp peaks in the electronic DOS [45].

We can quantify the reduction of the Purcell effect by introducing an effective Purcell factor, F_{eff}, defined as the emission into the cavity relative to the corresponding emission in bulk, i.e. in the absence of a cavity and PhC, so that eqn. (3.30) is appropriate for the optical DOS

$$F_{eff} = \frac{R_c}{R_{bulk}} \tag{3.36}$$

Notice that in the simple model $R_{bulk} = BN^2$, so that $F_{eff} = F$ in this case. In figure 3.6a, the effective Purcell factor as a function of the carrier density has been calculated for a quantum well device. Compared to the normal Purcell factor, F_{eff} is clearly reduced even for a Q-factor of 2000, which is a typical PhC cavity quality factor. The effective Purcell factor drops off at high carrier density due to the bandfilling effect discussed in connection with figure 3.4. Figure 3.6b shows the effective Purcell factor as a function of the Q-factor and in this figure it is apparent that F_{eff} is reduced relative to the normal Purcell factor for $Q \gtrsim 10$. As typical PhC cavities have Q-factors of several thousands, this reduction in the Purcell effect is quite significant. Note that although F_{eff} is reduced relative to F, there is still some enhancement (roughly a factor of 20 for these parameters), but striving to increase the Purcell enhancement through engineering the Q-factor, as is often done in the literature, is futile.

Returning to figure 3.4, we see that for $N \lesssim N_{tr}$ the cavity emission increases as $R_c \propto N^2$. We can derive an approximate expression for the cavity emission in the full model for low carrier density, i.e. eqn. (3.35) by expressing the quasi Fermi function in terms of the carrier density. For low homogeneous broadening

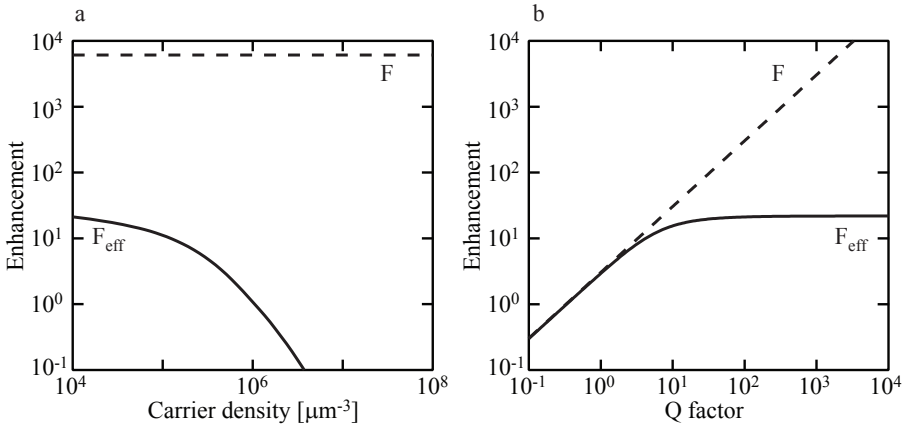

Fig. 3.6: The effective Purcell factor (solid line) compared to the normal Purcell factor (dashed line) for a quantum well device as a function of a) the carrier density and b) Q-factor. *Parameters in table E.1*

we can use eqn. (3.20) and write

$$\begin{aligned} N &\approx \int \rho_e^{QW}(E)\, f_c(E)\, dE \\ &= \frac{m_e^*}{\pi\hbar^2\ell} \sum_{m=1}^{\infty} \int \Theta(E - E_m)\, f_c(E)\, dE \\ &= \frac{m_e^*}{\pi\hbar^2\ell} \sum_{m=1}^{\infty} \int_{E_m}^{\infty} f_c(E)\, dE \end{aligned} \tag{3.37}$$

The integral over the quasi Fermi function evaluates as

$$\begin{aligned} \int_{E_m}^{\infty} f_c(E)\, dE &= \int_{E_m}^{\infty} \frac{1}{1 + e^{\frac{E - E_f}{k_B T}}} dE \\ &= -(E_m - E_f) + k_B T \ln\left(1 + e^{\frac{E_m - E_f}{k_B T}}\right) \\ &= k_B T \ln\left(1 + e^{-\frac{E_m - E_f}{k_B T}}\right) \end{aligned} \tag{3.38}$$

If we assume $N \ll N_{tr}$, so that $f_c(E_n) \ll \frac{1}{2}$, we can write

$$\begin{aligned} \int_{E_m}^{\infty} f_c(E)\, dE &= k_B T \ln\left(1 + e^{-\frac{E_m - E_f}{k_B T}}\right) \\ &= k_B T \ln\left(\frac{1}{1 - f_c(E_m)}\right) \\ &\approx k_B T f_c(E_m) \end{aligned} \tag{3.39}$$

Inserting eqn. (3.39) in eqn. (3.37), we find

$$\begin{aligned} N &\approx \frac{m_e^*}{\pi\hbar^2\ell}\sum_{m=1}^{\infty} k_B T f_c\left(E_m\right) \\ &\approx \frac{m_e^*}{\pi\hbar^2\ell} k_B T f_c\left(E_1\right) \end{aligned} \tag{3.40}$$

where the last step is valid for low carrier densities. We need to evaluate $f_c\left(E_1\right)$ at the energy of the cavity, so using eqn. (2.1), we write

$$f_c\left(E_1\right) = \left[1 + e^{\frac{E_1 - E_c}{k_B T}}\left(\frac{1}{f_c\left(E_c\right)} - 1\right)\right]^{-1} \approx e^{\frac{E_c - E_1}{k_B T}} f_c\left(E_c\right) \tag{3.41}$$

Now, we can express R_c in terms of the carrier density for $N \ll N_{tr}$ and for sufficiently high Q

$$\begin{aligned} R_c &= \frac{1}{\tau_c}\frac{3\nu_c}{\pi V_n}\tilde{\rho}_e\left(h\nu_c\right)\left(e^{\frac{E_1 - E_c}{k_B T}}\frac{\pi\hbar^2\ell}{k_B T m_e^*}\right)^2 N^2 \\ &= \frac{F}{Q} B' N^2 \end{aligned} \tag{3.42}$$

where we have written explicitly the F and Q dependence and collected the rest of the terms in B'. This expression shows that for low carrier density and for Q-factors typical for PhC cavities, the spontaneous emission rate can be written in the form that was used in the simple model (FBN^2). However, the appearance of the Q-factor in the denominator reduces the Purcell factor considerably as discussed above.

The spontaneous emission rate for QD devices is calculated similarly using eqn. (3.17) together with eqns. (3.25) and (3.34). Here, the electronic DOS is much narrower than in the QW case discussed above and the reduction of the Purcell enhancement should be correspondingly weaker. Figure 3.7 shows the spontaneous emission into the cavity and background for a QD device. Compared to the quantum well device in figure 3.4, figure 3.7 shows a similar behavior, but with a much sharper bandfilling. This is consistent with the narrow QD electronic DOS. The effective Purcell factor is calculated in figure 3.8 as a function of carrier density and cavity Q-factor. For the dependence on the carrier density in figure 3.8a, the effective Purcell factor drops off more rapidly than in the QW case, corresponding to the more abrupt bandfilling effect. In figure 3.8b the same dependence on the Q-factor as in the QW is seen, but now, due to the narrower electronic DOS, the effective Purcell factor saturates at a higher Q-factor (≈ 10000 for this broadening). Thus, for QD devices F_{eff} can become much larger than for QW devices for the same cavity. Note that different mode volumes were used to calculate figures 3.6 and 3.8. The QD device has a mode volume of $V_n = 4.4$, while the QW device has $V_n = 0.2$. If a mode volume of $V_n = 4.4$ had been used for the QW device, R_c in figure 3.6 would have been 22 times lower.

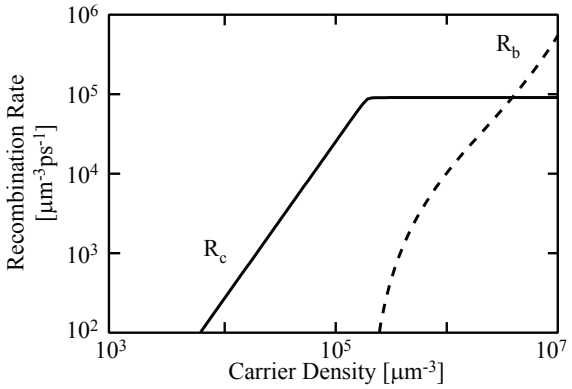

Fig. 3.7: The cavity spontaneous emission, R_c, and background spontaneous emission, R_b, calculated for a quantum dot device in the full model. *Parameters in table E.2.*

3.5 Stimulated Emission

Turning now to the stimulated emission rate in eqn. (3.18), we need to specify the radiation spectral density, W, before we can evaluate the integral. Often, the radiation spectral density is taken as $W(\nu) = h\nu P\delta(\nu - \nu_c)$, which mimics the narrow laser linewidth found above threshold [31]. Using this expression and the electronic DOS defined in section 3.3, we can calculate the stimulated emission for a QW or QD device. Figure 3.9 shows the calculated normalized gain for a QW device in a PhC cavity as a function of carrier density. The behavior in figure 3.9 is often approximated by the logarithmic expression mentioned in section 3.1, namely

$$G = v_g G_0 \ln\left(\frac{N + N_s}{N_{tr} + N_s}\right) \tag{3.43}$$

It can be fitted to experimental measurements of the gain and provides a simple expression for use in the LREs.

The relation between the Purcell factor and the stimulated emission rate has been the matter of some confusion in the literature. In LRE modeling, the most common approach is to include the Purcell enhancement in the terms pertaining to the spontaneous emission process and leave stimulated emission unchanged [12, 26]. However, the Purcell effect is an enhancement of the light-matter coupling which is the same for both the spontaneous and stimulated emission process. Indeed, in derivations of the light-matter interaction from a quantization of the electromagnetic field, the same prefactor, A_{QO}, scales the two recombination processes

$$A_{QO}(n_p + 1) \tag{3.44}$$

where n_p here is the number of photons that leads to stimulated emission and the 1 leads to spontaneous emission. Thus, if spontaneous emission is Pur-

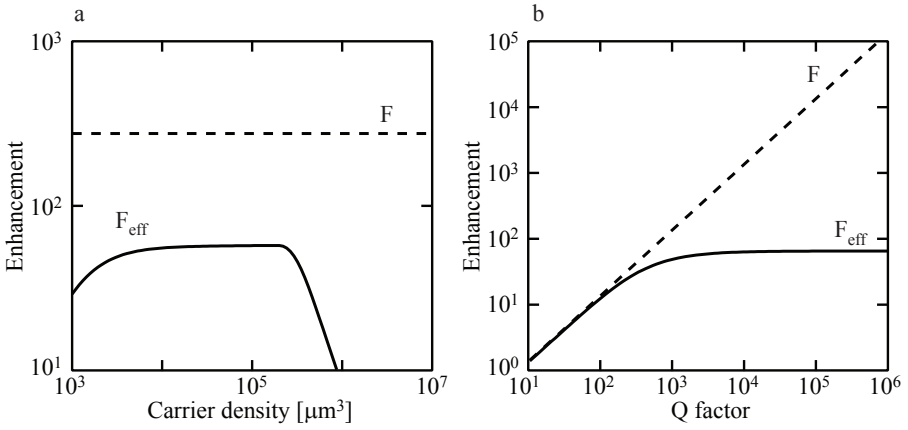

Fig. 3.8: The effective Purcell factor (solid line) compared to the normal Purcell factor (dashed line) for a quantum dot device as a function of a) the carrier density and b) Q-factor. *Parameters in table E.2.*

cell enhanced in a nanocavity, so should stimulated emission be. This view have been suggested before by Brorson and Yokoyama [25] and there have also been experimental data, that seemingly can only be understood if stimulated emission experiences an enhancement [61, 62]. In the literature dealing with microscopic modeling of semiconductor devices, it is even the default premise that both spontaneous and stimulated emission feel the same enhancement [63]. These points all suggest that the Purcell enhancement should be treated equally in spontaneous and stimulated emission.

With the above indications, we feel confident that stimulated emission should be Purcell enhanced. In appendix A is outlined a formalism by N. Gregersen *et al.* [64], where the derivation of the recombination rates presented in section 3.2 is modified to include the Purcell enhancement in both spontaneous and stimulated emission. As outlined in the appendix, the spectral radiation density must be expressed in terms of the optical local density-of-states (LDOS), ρ_L, as

$$W\left(\hat{\boldsymbol{d}}, \boldsymbol{r_0}, \nu\right) = \hbar\nu P \rho_L\left(\hat{\boldsymbol{d}}, \boldsymbol{r_0}, \nu\right) \tag{3.45}$$

where $\hat{\boldsymbol{d}}$ and $\boldsymbol{r_0}$ are the dipole orientation and position. Using this expression for the spectral radiation density and following the same steps as in section 3.2, the stimulated recombination rate can be written

$$\begin{aligned} R_{st} = \rho_L\left(\hat{\boldsymbol{d}}, \boldsymbol{r_0}, \nu_c\right) B^G P \int & \frac{\delta\nu_c^2}{\left(h\nu - h\nu_c\right)^2 + \delta\nu_c^2} \\ & \times h\nu \left(2 f_c\left(E_{21}\right) - 1\right) \rho_e\left(E_{21}\right) \\ & \times L\left(h\nu - E_{21}\right) dh\nu dE_{21} \end{aligned} \tag{3.46}$$

where $B^G = nn_g B$ and n_g is the group index. The factor nn_g appears because ρ_L includes the general non-uniform dielectric constant in its normal-

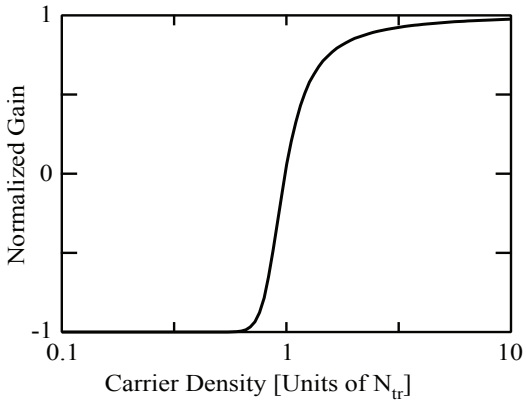

Fig. 3.9: The gain as a function of carrier density for a quantum well device in a photonic crystal cavity calculated in the full model. *Parameters in table E.1.*

ization. Here, both recombination rates are scaled by the same prefactor, $\rho_L(\hat{\boldsymbol{d}}, \boldsymbol{r_0}, \nu_c)B^G$, which we will write as

$$\rho_L\left(\hat{\boldsymbol{d}}, \boldsymbol{r_0}, \nu_c\right) B^G = \frac{F}{\tau_{21}} \tag{3.47}$$

Comparing to the corresponding expression for spontaneous emission, i.e. eqn. (3.17), we see that the dependence on the cavity lineshape is identical. We therefore expect the same reduction of the effective Purcell enhancement for broad electronic DOS as was seen for spontaneous emission. Thus, inclusion of the Purcell effect should primarily be a factor for QD devices. As the Purcell factor is multiplied onto the expression for the stimulated emission it merely enhances the maximum gain while the threshold is unchanged. Therefore, eqn. (3.46) follows the same general behavior seen in figure 3.9.

The fact that stimulated emission is Purcell enhanced, was not realized until late in the Ph.D., where most of the analysis of the QW devices was finished. For these devices, the logarithmic gain expression in eqn. (3.43) was used and unfortunately, there was not enough time for a reexamination of the QW results in the light of the altered stimulated emission rate. However, since the Purcell enhancement is severely reduced for QW devices, we feel that the conclusions drawn in the following sections dealing with QW devices (sections 4.1 and 4.2) are still valid.

3.6 Full Model

With the expressions for the spontaneous and stimulated emission in place, the full LRE model that will be used in the subsequent chapters can be summed up as follows.

The basic LREs are

$$\dot{N} = J - R_{nr} - R_c - R_b - R_{st} \tag{3.48}$$

$$\dot{P} = \Gamma R_c + \Gamma R_{st} - R_p \tag{3.49}$$

and the spontaneous emission rates are given by

$$R_c = \frac{F}{\tau_{21}} \int \frac{\left(\frac{1}{2}\delta\nu_c\right)^2}{\left(\nu - \nu_c\right)^2 + \left(\frac{1}{2}\delta\nu_c\right)^2} f_c^2\left(h\nu\right) \tilde{\rho}_e\left(h\nu\right) dh\nu \tag{3.50}$$

$$R_b = \frac{1}{\tau_{21}} \int \left(\frac{\nu}{\nu_c}\right)^3 \left[\Theta\left(\nu_L - \nu\right) + \Theta\left(\nu - \nu_U\right)\right] f_c^2\left(h\nu\right) \tilde{\rho}_e\left(h\nu\right) dh\nu \tag{3.51}$$

with the electronic DOS given by

$$\tilde{\rho}_e^{QW}\left(h\nu\right) = \frac{m^*}{\pi\hbar^2\ell} \sum_m \left(\frac{1}{2} + \frac{1}{\pi}\arctan\left(\frac{h\nu - E_m}{\frac{\gamma}{2}}\right)\right) \tag{3.52}$$

for a QW device and

$$\tilde{\rho}_e^{QD}\left(h\nu\right) = \frac{2}{V_{QD}} F_V\left(h\nu - h\nu_{QD}, \gamma, \sigma\right) \tag{3.53}$$

for QD device. The stimulated emission rate is given by the logarithmic gain for QW devices, i.e.

$$R_{st} = P v_g G_0 \ln\left(\frac{N + N_s}{N_{tr} + N_s}\right) \tag{3.54}$$

and by the Purcell Enhanced Stimulated Emission (PESE) expression for QD devices, i.e.

$$R_{st} = P\frac{F}{\tau_{21}} \int \frac{\left(\frac{1}{2}\delta\nu_c\right)^2}{\left(h\nu - h\nu_c\right)^2 + \left(\frac{1}{2}\delta\nu_c\right)^2} h\nu \left(2f_c\left(h\nu\right) - 1\right) \tilde{\rho}_e\left(h\nu\right) dh\nu \tag{3.55}$$

Gain suppression effects are neglected except in section 4.2, where we treat QW devices and include them in eqn. (3.54) as

$$R_{st,gs} = \frac{1}{1 + \varepsilon_{SHB} P} R_{st} \tag{3.56}$$

The photon loss is given by

$$R_p = \frac{P}{\tau_p} \tag{3.57}$$

The non-radiative losses will, for the most part, be ignored, but when it is included it is given by the linear expression

$$R_{nr} = A_s N + C N^3 = \frac{N}{\tau_{nr}} \tag{3.58}$$

where $\frac{1}{\tau_{nr}} = A_s + C N_{tr}^2$. These equations constitute the full model that will be used throughout this thesis.

3.7 Cluster Expansion Model

As mentioned above, the LREs are phenomenological equations that have been developed over time to mimic the behavior of semiconductor laser devices. While simple in form and relatively easily analyzed, they are also highly parameterized and therefore prone to misinterpretation. For example, the LREs can be brought to fit almost any measured I/O curve by adjusting parameters, whose true values may be different from the ones chosen. Furthermore, the available experimental results for nanocavity lasers are rather scarce and usually the Purcell factor is so low that any effect on the I/O curve could be contributed to other effects. Therefore, we cannot ascertain from comparison to experiments if our implementation of the PESE term is correct.

As an alternative, we can compare the full model to microscopic models, which are derived from a fundamentally different starting point. Microscopic modeling starts from e.g. the Schrödinger equation and include all relevant interactions in the system Hamiltonian. In this way, all processes are derived from first principle, rather than included as phenomenological terms. Although this method of checking the model is not ideal, it is probably the best available alternative. Below, we make a brief outline of the microscopic Cluster Expansion Model (CEM) [65–67], which has been used to successfully model semiconductor laser devices [63]. Comparison of the LRE model and the CEM is presented in section 4.5.

Microscopic modeling generally starts out from the Schrödinger equation by setting up the Hamiltonian for the system in question. The Hamiltonian consists of terms for the isolated subsystems (e.g. electrons, photons and phonons) and all relevant interactions. The spontaneous emission process is founded in interaction with the vacuum field and is thus an inherent quantum mechanical process. Therefore, it is necessary to include the full quantization of the electromagnetic field in laser modeling in order to capture the correct spontaneous emission behavior [32].

A typical approach is to calculate equations of motion for the quantities of interest (usually expectation values for the electron and photon number operators) using the Heisenberg equation of motion

$$i\hbar d_t \hat{\mathcal{O}} = \left[\hat{H}, \hat{\mathcal{O}}\right] \tag{3.59}$$

where $\hat{\mathcal{O}}$ is an operator for the physical quantity of interest and $\hat{H}$ is the Hamiltonian. Evaluating the commutator relation for a given operator results in equations of motions, which in general involves higher order expectation values. Equations of motions for a singlet[4] quantity (e.g. $\langle c^\dagger c\rangle$, denoted $\langle 1\rangle$), will typically involve expectation values of doublet quantities ($\langle 2\rangle$, e.g. $= \langle b^\dagger v^\dagger c\rangle$).

[4] Here, the classification into singlets, doublets, triplets, etc. arises from the fact that the transition of a conduction band electron to the valence band ($v^\dagger c$) is always accompanied with the creation of a photon ($b^\dagger$). Thus, if $\langle c^\dagger c\rangle$ and $\langle v^\dagger v\rangle$ are denoted singlet quantities then $\langle b^\dagger v^\dagger c\rangle$ must refer to a doublet.

Calculating equations of motion for the doublet quantities results in even higher order quantities, which needs to be calculated and so on *ad infinitum*. This results in an infinite hierarchy of linked equations, that involves higher and higher order quantities. In usual microscopic models, the chain is truncated at some point by setting a quantity to zero, resulting in a closed set of equations.

In the CEM, the strategy is to rewrite the higher order expectation values in terms of combinations of the known lower order expectation values and unknown correlation functions. Schematically, the expectation values can be written as [63]

$$\begin{aligned}
\langle 1\rangle &= \delta\langle 1\rangle \\
\langle 2\rangle &= \langle 1\rangle\langle 1\rangle + \delta\langle 2\rangle \\
\langle 3\rangle &= \langle 1\rangle\langle 1\rangle\langle 1\rangle + \langle 1\rangle\delta\langle 2\rangle + \delta\langle 3\rangle \\
\langle 4\rangle &= \langle 1\rangle\langle 1\rangle\langle 1\rangle\langle 1\rangle + \langle 1\rangle\langle 1\rangle\delta\langle 2\rangle \\
&\quad + \langle 1\rangle\delta\langle 3\rangle + \delta\langle 2\rangle\delta\langle 2\rangle + \delta\langle 4\rangle \\
&\quad \vdots
\end{aligned}$$

where $\delta\langle N\rangle$ denotes the correlation function of order N. This scheme allows for a truncation of the chain, not at a higher order expectation value, but at a higher order correlation function. In this way, more information about collision terms and energy renormalization is retained up to the truncation order. From the truncated equation of motion chain, equations for the evolution of the photon number and electron states occupation can be derived [63].

For an ensemble of N_{QD} QDs (with s- and p-shell states) without inhomogeneous broadening, coupled to a single mode nanocavity (assumed on resonance with the s-state), the equations take the form[5]

$$\dot{f}_p = \left(1 - f_p - f_p^h\right) p - s\left(1 - f_s\right) f_p \tag{3.60}$$

$$\dot{f}_s = 2s\left(1 - f_s\right) f_p - \frac{2}{\hbar}\left|g\right|^2 \left\langle b^\dagger v^\dagger c\right\rangle - \frac{1-\beta}{\tau_{sp}} f_s f_s^h \tag{3.61}$$

$$\dot{n}_p = \frac{2}{\hbar} N_{QD} \left|g\right|^2 \left\langle b^\dagger v^\dagger c\right\rangle - \frac{2}{\hbar}\kappa n_p \tag{3.62}$$

where f_p and f_s are the electron occupation of the p- and s-state, $n_p = \left\langle b^\dagger b\right\rangle$ is the photon number, s is the scattering rate, τ_{sp} is the radiative lifetime, $\kappa = \frac{\hbar\omega_c}{2Q}$ is the photon loss rate and superscript h denotes hole quantities. The factor of 2 in the first term of eqn. (3.61) is present because electrons scatter into the s-state from two distinct p-states. The dipole coupling constant, g, is given by

$$\left|g\right|^2 = \frac{\hbar}{2}\frac{\beta\kappa}{\tau_{sp}} \tag{3.63}$$

[5] The model also includes corresponding equations for the hole quantities. They are similar in form as the electron equations and as we are not going to use them explicitly in the following, they are not shown here.

Here the dipole coupling strength is chosen to reproduce the total radiative lifetime τ_{sp}. The photon assisted polarization, $\langle b^\dagger v^\dagger c\rangle$, is determined by a separate differential equation

$$d_t \langle b^\dagger v^\dagger c\rangle = -\frac{\kappa+\Gamma_H}{\hbar}\langle b^\dagger v^\dagger c\rangle + \frac{1}{\hbar}\left(f_s f_s^h - \left(1-f_s-f_s^h\right)n_p\right) + \delta\langle b^\dagger b c^\dagger c\rangle - \delta\langle b^\dagger b v^\dagger v\rangle \quad (3.64)$$

where $\Gamma_H = \frac{\gamma}{2}$ is the homogeneous broadening. The two last terms in eqn. (3.64) are correlation functions for the doublet quantities $\langle b^\dagger b c^\dagger c\rangle$ and $\langle b^\dagger b v^\dagger v\rangle$. These terms are determined by separate differential equations, that include non-Markovian terms and which are not shown here [63]. The total radiative lifetime τ_{sp} contains contributions from the emission to the laser mode $\left(\tau_l = \frac{\tau_{bulk}}{F}\right)$ and all other modes $\left(\tau_{nl} = \frac{\tau_l}{\frac{1}{\beta}-1}\right)$, so that

$$\frac{1}{\tau_{sp}} = \frac{1}{\tau_l} + \frac{1}{\tau_{nl}} = \frac{F}{\beta\tau_{bulk}} \quad (3.65)$$

where τ_{bulk} is the spontaneous emission lifetime in bulk.

For low pumping where $f_s \ll 1$, $f_p \ll 1$ and $n_p \ll 1$ and in steady-state, where $\delta\langle b^\dagger b c^\dagger c\rangle$ and $\delta\langle b^\dagger b v^\dagger v\rangle$ approach zero, we can simplify eqn. (3.64) as

$$0 = d_t\langle b^\dagger v^\dagger c\rangle \approx -\frac{\kappa+\Gamma_H}{\hbar}\langle b^\dagger v^\dagger c\rangle + \frac{1}{\hbar} f_s f_s^h$$
$$\langle b^\dagger v^\dagger c\rangle = \frac{f_s f_s^h}{\kappa+\Gamma_H} \quad (3.66)$$

so that eqns. (3.60)-(3.62) in steady-state can be written as

$$0 = \dot{f}_p \approx p - s f_p \quad (3.67)$$

$$0 = \dot{f}_s \approx 2s f_p - \frac{\beta}{\tau_{sp}}\frac{\kappa}{\kappa+\Gamma_H} f_s f_s^h - \frac{1-\beta}{\tau_{sp}} f_s f_s^h \quad (3.68)$$

$$0 = \dot{n_p} \approx N_{QD}\frac{\beta\kappa}{\tau_{sp}}\frac{f_s f_s^h}{\kappa+\Gamma_H} - \frac{2}{\hbar}\kappa n_p \quad (3.69)$$

From these equations, we find the approximate steady-state photon density for low pump

$$n_p = \frac{\hbar N_{QD}}{\kappa+\Gamma_H}\frac{p}{\frac{\kappa}{\kappa+\Gamma_H}+\frac{1-\beta}{\beta}} \quad (3.70)$$

4. NANOLASER AND NANOLED RESULTS

In this chapter, we analyze the model developed in chapter 3 and summarized in section 3.6 by studying quantum well (section 4.1-4.3) and quantum dot systems (section 4.4 and 4.5). We begin by studying the general properties of the I/O curve and modulation response of quantum well devices. In section 4.2, we present a thorough study of nanocavity LEDs and lasers in context of the papers by Altug *et al.* [12] and Lau *et al.* [26]. In section 4.3, a simplified version of the full model is used for fitting measured I/O curves for lasing in Anderson localized modes. Quantum dot nanoLEDs are studied in section 4.4 and in section 4.5, the validity range of the full model is discussed by comparing to the cluster expansion model outlined in section 3.7.

4.1 Quantum Well Devices

With the full model specified in section 3.6, we now proceed to calculate I/O curves and the dynamical properties of the QW systems. For a first calculation, we obtain a standard I/O curve for a typical nanocavity laser using the parameters listed in table E.1 in appendix E. The result is shown in figure 4.1a. In order to see the variation of the β-factor with the input, the corresponding curve calculated using a fixed β-factor of 0.14 is shown as well. To make the β-factors be equal at threshold, a small background optical DOS has been added to the bandgap floor in the full model for this calculation. Both curves follow the S-shaped curve, characteristic for the threshold behavior for I/O curve on a double logarithmic scale and the slight deviation at low current corresponds to the difference in the β-factors shown in figure 4.1. The decrease of the varying β in figure 4.1b is due to the emission into the cavity, R_c, beginning to saturate just before threshold.

The features seen in figure 4.1a can be understood from steady-state solutions to the governing differential equations. Using the general expressions in eqns. (3.48) and (3.49), we find in steady-state ($\dot{N} = 0$ and $\dot{P} = 0$)

$$J - R_{nr} - R_b = R_c + R_{st} \tag{4.1}$$

$$R_p = \Gamma \left(J - R_{nr} - R_b \right) \tag{4.2}$$

Ignoring non-radiative losses, inserting eqn. (3.57) for R_p in eqn. (4.2) and taking the carrier density to be clamped far above threshold, we find expressions for the above and below threshold steady-state photon density

$$P = \Gamma \tau_p \left(J - R_b \right) \approx \begin{cases} \Gamma \tau_p \beta J & \text{for } J \ll J_{th} \\ \Gamma \tau_p J & \text{for } J \gg J_{th} \end{cases} \tag{4.3}$$

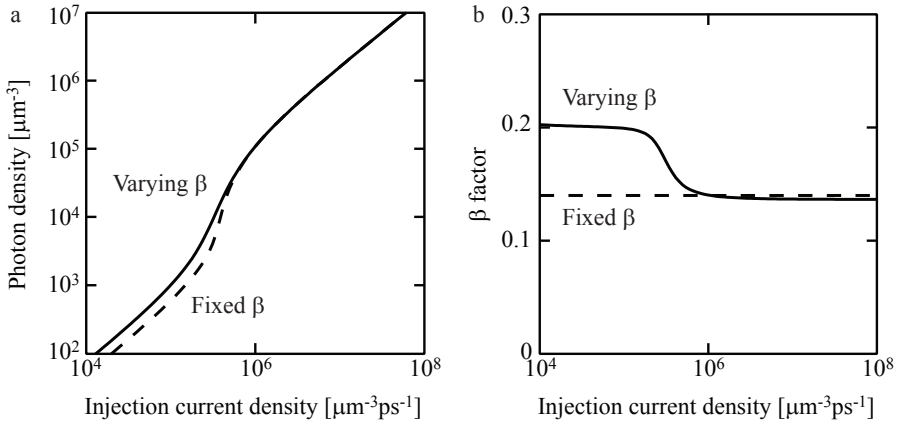

Fig. 4.1: a) The I/O curve and b) the β-factor for a typical QW device as a function of the injection current density. The dashed curves are calculated with a fixed β-factor ($\beta = 0.14$) while in the solid curves β was allowed to vary and is calculated from $\beta = \frac{R_c}{R_c+R_b}$. *Parameters in table E.1.*

This expression fits well with the overall behavior in figure 4.1a, where the deviation from a straight line (in the double logarithmic plot) is controlled by the magnitude of the emission to the background, R_b, which is related to the β-factor.

As mentioned in section 3.4, the Purcell enhancement in a nanocavity is strongly dependent on the relative widths of the electronic and optical DOS. In the case of a QW device, which has a broad electronic DOS, the Purcell enhancement is severely reduced compared to the ideal value and this influences the properties of the device. In figure 4.2, we explore the effect on the I/O curve and the β-factor for Q-factors varying from 100 to 10000. Only small variations of the I/O curves are observed below $J = 10^6$ $\mu\text{m}^{-3}\text{ps}^{-1}$, which are mainly due to the change in the photon lifetime, $\tau_p = \frac{Q}{\omega_c}$. This is in correspondence with the effective Purcell factor being almost independent of Q for cavity quality factors larger than a few hundred (c.f. fig. 3.6b). The corresponding curves for the β-factor reflect this fact by being almost unchanged for low pumping. Above $J = 10^6$ $\mu\text{m}^{-3}\text{ps}^{-1}$, the I/O curve evolves from non-lasing to lasing behavior with increasing Q-factor, which is due to the photon loss being inversely proportional to the cavity Q. In fig. 4.2b, the β-factor evolves from a strong to a weaker dependence on pump for increasing Q-factor. At high Q, the system is lasing, so that the carrier density clamps at its threshold value. This fixes R_c and R_b to their respective threshold values and β thus remains at a high value. For low Q-factors, the system is non-lasing, so that the carrier density can increase for $J > 10^6$ $\mu\text{m}^{-3}\text{ps}^{-1}$. Thus, as R_c saturates due to the band-filling effect, R_b increases rapidly giving rise to the fast decrease of the β-factor.

Although F_{eff} is effectively independent of the Q-factor, the Purcell enhance-

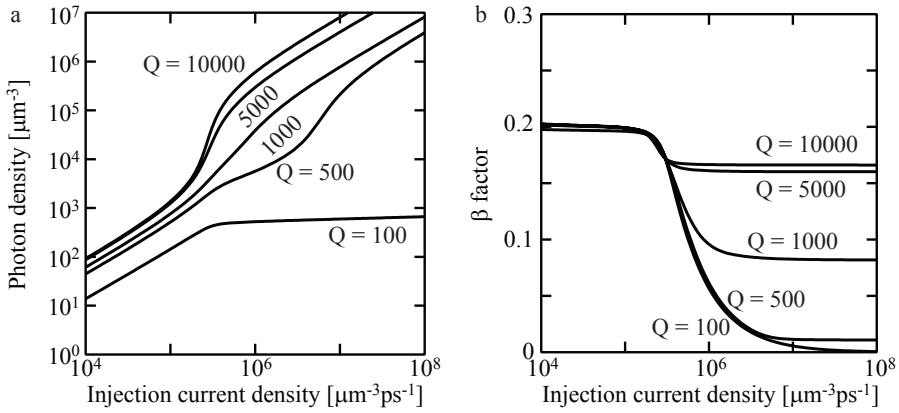

Fig. 4.2: a) The I/O curve and b) the β-factor for a range of QW devices with varying Q-factors as a function of the injection current density. *Parameters in table E.1.*

ment can still be affected by varying the modal volume. To study the effect of the Purcell enhancement, we therefore vary V_n from 0.01 to 10 in figure 4.3 and plot the I/O curves and the β-factors. Changing the modal volume yields almost no change of the above threshold behavior, while the change in the below threshold I/O curves is significant. Decreasing the modal volume, makes the effective Purcell factor go up, so that the β-factor increases towards unity. This accounts for the change in the I/O curve towards a straight line in the double logarithmic plot.

The dynamical properties of the devices can be explored through the modulation response, which can be obtained in several ways in numerical simulations. In direct modulation, a sinusoidal perturbation is applied to the system in steady-state and the output is measured. From this, the modulation response is determined as

$$H_{DM}(\omega) = \frac{\max\{P(t)\} - \min\{P(t)\}}{\max\{J(t)\} - \min\{J(t)\}} \tag{4.4}$$

Although this method is simple and robust, it is also slow as the modulation response must be calculated for each frequency of interest in order to obtain curves like figure 2.3. An alternative method consists of applying a δ-like pulse to the steady-state input and Fourier transforming the output. In linear response theory, the output can be written as a convolution of the input and the response function as

$$P(t) = \int J(t') H(t - t') dt' \tag{4.5}$$

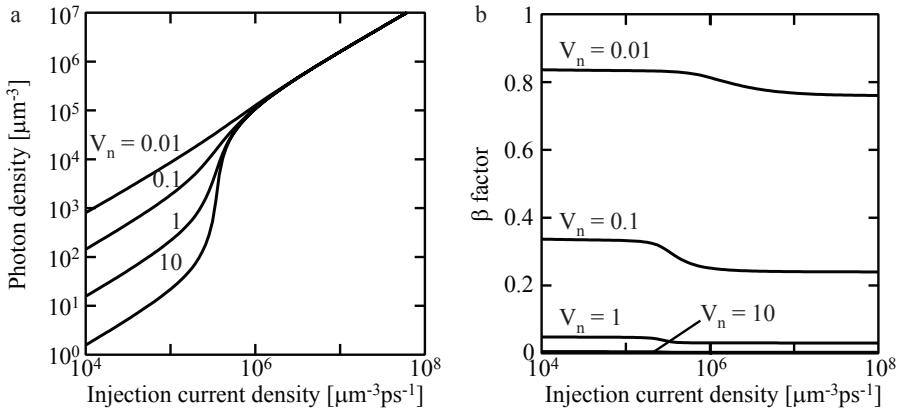

Fig. 4.3: a) The I/O curve and b) the β-factor for a range of QW devices with varying modal volumes as a function of the injection current density. *Parameters in table E.1.*

Applying a δ-pulse to the input in a system in steady-state (ss) gives

$$\begin{aligned} P(t) &= \int \left(J_{ss}(t') + \delta(t')\right) H(t-t')\, dt' \\ &= P_{ss}(t) + H(t) \end{aligned} \tag{4.6}$$

Thus, by subtracting the steady-state part of the output and Fourier transforming the rest, the frequency modulation response can be obtained from a single calculation.

$$H_\delta(\omega) = \frac{1}{2\pi} \int H(t)\, e^{-i\omega t} dt \tag{4.7}$$

A third option is to perform a small-signal analysis of the differential equations involved. The small-signal analysis begins by taking the total differential of the differential equations, i.e. eqns. (3.48) and (3.49) as

$$d\dot{N} = dJ - dR_{nr} - dR_c - dR_b - dR_{st} \tag{4.8}$$

$$d\dot{P} = \Gamma dR_c + \Gamma dR_{st} - dR_p \tag{4.9}$$

where we can expand the derivatives based on the dependence on the variables

$$\begin{aligned} dR_{nr} &= \frac{\partial R_{nr}}{\partial N} dN \\ dR_c &= \frac{\partial R_c}{\partial N} dN \\ dR_b &= \frac{\partial R_b}{\partial N} dN \\ dR_{st} &= \frac{\partial R_{st}}{\partial N} dN + \frac{\partial R_{st}}{\partial P} dP \\ dR_p &= \frac{\partial R_p}{\partial P} dP \end{aligned}$$

Assuming further that $dJ = \Delta J e^{i\omega t}$, $dN = \Delta N e^{i\omega t}$ and $dP = \Delta P e^{i\omega t}$, the total differentials can be written as

$$\begin{bmatrix} \Delta J \\ 0 \end{bmatrix} = \begin{bmatrix} i\omega + \gamma_{NN} & \gamma_{NP} \\ -\gamma_{PN} & i\omega + \gamma_{PP} \end{bmatrix} \begin{bmatrix} \Delta N \\ \Delta_P \end{bmatrix} \tag{4.10}$$

where the matrix elements are

$$\gamma_{NN} = \partial_N R_{nr} + \partial_N R_c + \partial_N R_b + \partial_N R_{st} \tag{4.11}$$
$$\gamma_{NP} = \partial_P R_{st} \tag{4.12}$$
$$\gamma_{PN} = \Gamma \partial_N R_c + \Gamma \partial_N R_{st} \tag{4.13}$$
$$\gamma_{PP} = \partial_P R_p - \Gamma \partial_P R_{st} \tag{4.14}$$

We solve for ΔP using Cramer's rule [68], which involves the determinant of the coefficient matrix in eqn. (4.10)

$$\begin{aligned} \Delta &= \begin{vmatrix} i\omega + \gamma_{NN} & \gamma_{NP} \\ -\gamma_{PN} & i\omega + \gamma_{PP} \end{vmatrix} \\ &= (i\omega)^2 + i\omega(\gamma_{NN} + \gamma_{PP}) + \gamma_{NN}\gamma_{PP} + \gamma_{NP}\gamma_{PN} \end{aligned} \tag{4.15}$$

and the determinant

$$\Delta_P = \begin{vmatrix} (i\omega + \gamma_{NN}) & \Delta J \\ -\gamma_{PN} & 0 \end{vmatrix} = \Delta J \gamma_{PN} \tag{4.16}$$

Then according to Cramer's rule $\Delta P = \frac{\Delta_P}{\Delta}$ and we can get the modulation response function as $H(\omega) = \frac{\Delta P}{\Delta J}$.

$$H(\omega) = \frac{\gamma_{PN}}{(i\omega)^2 + i\omega(\gamma_{NN} + \gamma_{PP}) + \gamma_{NN}\gamma_{PP} + \gamma_{NP}\gamma_{PN}} \tag{4.17}$$

Normalizing to the DC response, we finally find

$$\begin{aligned} h(\omega) = \frac{H(\omega)}{H(0)} &= \frac{\gamma_{NN}\gamma_{PP} + \gamma_{NP}\gamma_{PN}}{(i\omega)^2 + i\omega(\gamma_{NN} + \gamma_{PP}) + \gamma_{NN}\gamma_{PP} + \gamma_{NP}\gamma_{PN}} \\ &= \frac{\omega_R^2}{\omega_R^2 - \omega^2 + i\omega\gamma_R} \end{aligned} \tag{4.18}$$

where

$$\omega_R^2 = \gamma_{NN}\gamma_{PP} + \gamma_{PN}\gamma_{NP} \tag{4.19}$$
$$\gamma_R = \gamma_{NN} + \gamma_{PP} \tag{4.20}$$

are the relaxation frequency and the decay coefficient. Often, the frequency at which the modulation response drops below $\frac{1}{2}$ ($\approx$ -3dB) is taken as a measure of the modulation bandwidth. The 3dB-frequency, f_{3dB}, is then found from

$$\begin{aligned} \frac{1}{2} &= |h(\omega_{3dB})|^2 = \frac{\omega_R^4}{(\omega_R^2 - \omega^2)^2 + \omega^2\gamma_R^2} \\ 0 &= \omega^4 - \left(2\omega_R^2 - \gamma_R^2\right)\omega^2 - \omega_R^4 \end{aligned} \tag{4.21}$$

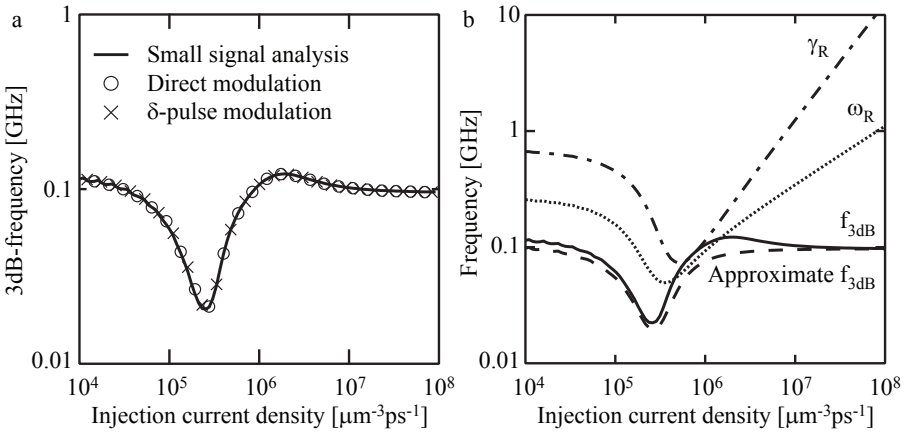

Fig. 4.4: a) 3dB-frequency versus injection current density calculated using a small signal model (solid line), a direct modulation method (circles) and a δ-pulse modulation method (crosses). b) The small signal f_{3dB} (solid), the relaxation frequency ω_R (dotted), the damping γ_R (dot-dashed) and the approximative expression for the 3dB-frequency, $f_{3dB} \approx \frac{1}{2\pi}\frac{\omega_R^2}{\gamma_R}$ (dashed). *Parameters in table E.1.*

which is solved to

$$f_{3dB} = \frac{1}{2\pi}\sqrt{\omega_R^2 - \frac{\gamma_R^2}{2} + \sqrt{\left(\omega_R^2 - \frac{\gamma_R^2}{2}\right)^2 + \omega_R^4}} \tag{4.22}$$

For nanocavity devices, we often have that the damping is much larger than the relaxation frequency, i.e. $\gamma_R \gg \omega_R$. In such cases, we can write

$$\begin{aligned} f_{3dB} &\approx \frac{1}{2\pi}\sqrt{\omega_R^2 - \frac{\gamma_R^2}{2} + \left|\omega_R^2 - \frac{\gamma_R^2}{2}\right|\left(1 + \frac{1}{2}\frac{\omega_R^4}{\left(\omega_R^2 - \frac{\gamma_R^2}{2}\right)^2}\right)} \\ &= \frac{1}{2\pi}\sqrt{\frac{1}{2}\frac{\omega_R^4}{\frac{\gamma_R^2}{2} - \omega_R^2}} \approx \frac{1}{2\pi}\frac{\omega_R^2}{\gamma_R} \end{aligned} \tag{4.23}$$

In figure 4.4a is shown the f_{3dB} curve for the same device as in figure 4.1 (with varying β) calculated using the three methods listed above. The figure shows perfect agreement between the 3dB-frequency calculated using the three methods. Which method to use is a matter of preference, however, the small signal expression allows for easy analysis to connect the LRE terms to the features of the 3dB-frequency. We therefore use the small signal expression in the following sections, where the modulation response for QW and QD devices is analyzed. For now, we note that the dip in the modulation response in figure 4.4a appears because the 3dB-frequency is governed at low pump by $\partial_N R_c$ and

$\partial_N R_b$, which decrease to zero as the bandfilling effect discussed in section 3.4 begins to set in. For higher pump, stimulated emission dominates and the f_{3dB} returns to the high value.

In figure 4.4b, the small signal f_{3dB} is plotted together with the relaxation frequency and damping as a function of the injection current density. Also shown is the approximate expression for the small signal f_{3dB}, which is valid for $\gamma_R \gg \omega_R$ (eqn. (4.23)). Notice that the modulation bandwidth calculated here, does not include parasitic effects from the electronic circuits driving the device. These effects make the performance depart from that of an ideal device and reduce the practically obtainable bandwidth. Thus, all modulation bandwidths calculated in this work represent "best case scenarios".

4.2 Modulation Response of NanoLEDs and Nanolasers

The above discussion shows that the small signal expression for the 3dB-frequency gives reliable results and we therefore move on and apply the model to a specific problem, namely the maximum attainable modulation bandwidth in QW nanocavity devices. This issue has been the focus of some debate since 2006, where Altug *et al.* [12] presented measurements on QW PhC nanolasers, that suggested that modulation speeds exceeding 100 GHz was possible using nanoscale devices. Their structure consisted of four 8 nm $In_{0.2}Ga_{0.8}As$ quantum wells embedded in a freestanding PhC membrane. Both single H1 cavities and arrays of coupled cavities were investigated and the group reported lasing from both types of structures and a measured Purcell enhancement of 76. This is a surprisingly high (effective) Purcell factor for quantum well devices for the reasons discussed in section 3.4. We note that the experiments were performed at cryogenic temperatures, where exciton peaks may possibly provide sharp features in the electronic DOS [45], giving a higher effective Purcell enhancement.

By pumping the structure with ultra short pulses, the group attempted to directly measure the modulation bandwidth and they claimed that the device response was faster than the pump, i.e. exceeding 100 GHz. The ultra fast modulation speed reported by Altug *et al.* was disputed in 2009 by Lau *et al.* [26], who pointed out that ultra short pump-probe measurements have been known to produce ultra fast response functions through gain switching. Furthermore, gain compression effects, which lead to a reduction of the modulation bandwidth at high photon densities, was not taken into account in the theoretical model. In their subsequent analysis, Lau *et al.* showed that using a model with spectral hole burning in the expression for the gain would lead to a reduction of the modulation bandwidth for increasing input power, contrary to the conventional result. The largest modulation bandwidth was found below threshold in the LED regime.

In their model, Lau *et al.* used the simple model for the spontaneous emission

in eqns. (3.4) and (3.4), i.e.

$$R_c + R_b = \beta F \frac{N}{\tau_{sp}} + (1-\beta)\frac{N}{\tau_{sp}} \tag{4.24}$$

However, this expression has a limited validity range and cannot faithfully be used to argue about the relative size of the recombination rates over the 6 orders of magnitude pump range considered in the paper. We therefore reexamine the system using the modified expression for the spontaneous emission presented in eqns. (3.50) and (3.51) [60]. Following Lau *et al.*[1], the logarithmic gain expression in eqn. (3.54) is modified to include the gain compression effects that appear at high photon densities (eqn. (3.56)).

$$G = v_g G_0 \frac{1}{1+\varepsilon_{SHB} P} \ln\left(\frac{N+N_s}{N_{tr}+N_s}\right) \tag{4.25}$$

We calculate the modulation bandwidth in the small-signal model (eqn. (4.22)) and using eqns. (4.11)-(4.14), the relaxation frequency and damping becomes

$$\omega_R^2 = \frac{1}{\tau_p}(aP_0 + R_{c,N}) + \Gamma\left(\frac{1}{\tau_{nr}} + R_{b,N}\right)\left(a_p P_0 + \frac{R_c}{P_0}\right) \tag{4.26}$$

$$\gamma_R = \frac{1}{\tau_{nr}} + R_{c,N} + R_{b,N} + P_0(a + \Gamma a_p) + \frac{\Gamma R_c}{P_0} \tag{4.27}$$

where N_0 and P_0 are steady-state carrier and photon densities and $a = \frac{\partial G}{\partial N}$, $a_p = -\frac{\partial G}{\partial P}$, $R_{c,N} = \frac{\partial R_c}{\partial N}$ and $R_{b,N} = \frac{\partial R_b}{\partial N}$.

We now proceed to calculate the steady-state carrier and photon densities, the spontaneous and stimulated emission and the 3dB-bandwidth for two specific devices in the simple and full model. To ease comparison, the (freely varying) β-factor calculated from the full model is used in the simple model. Device A has a Q-factor of 10^4 and a mode volume of 10 (full parameter set in table E.3) and device B has a Q-factor of 10^2 and a mode volume of 0.1 (table E.4). The results for device A are plotted in figure 4.5a-c, and for device B in figure 4.5d-f.

In figure 4.5a the carrier and photon densities are shown as a function of the pump (in units of $J_0 = \frac{N_{tr}}{\tau_{sp}}$). For $J < J_0$ the carrier density in the simple model is much lower than in the full model. This is an effect of the reduction of the effective Purcell factor for high Q-factors in the full model, which limits F_{eff} to ~ 1 for low carrier density, whereas $F_{eff} \sim 610$ in the simple model. The higher spontaneous emission rate in the simple model explains the lower carrier density. The carrier density in the full model clamps for $J \sim J_0$, when lasing sets in, and remains constant until $J \sim 100 J_0$, where it again begins to increase. This increase is due to the gain suppression that becomes a significant process

[1] As mentioned in section 3.5, these calculations were done before it was realized that stimulated emission should include the Purcell enhancement. Therefore, we use the same gain model as in the paper by Lau *et al.* and note that due to the reduction of the effective Purcell enhancement for QW devices, the error made by doing so will not be too severe.

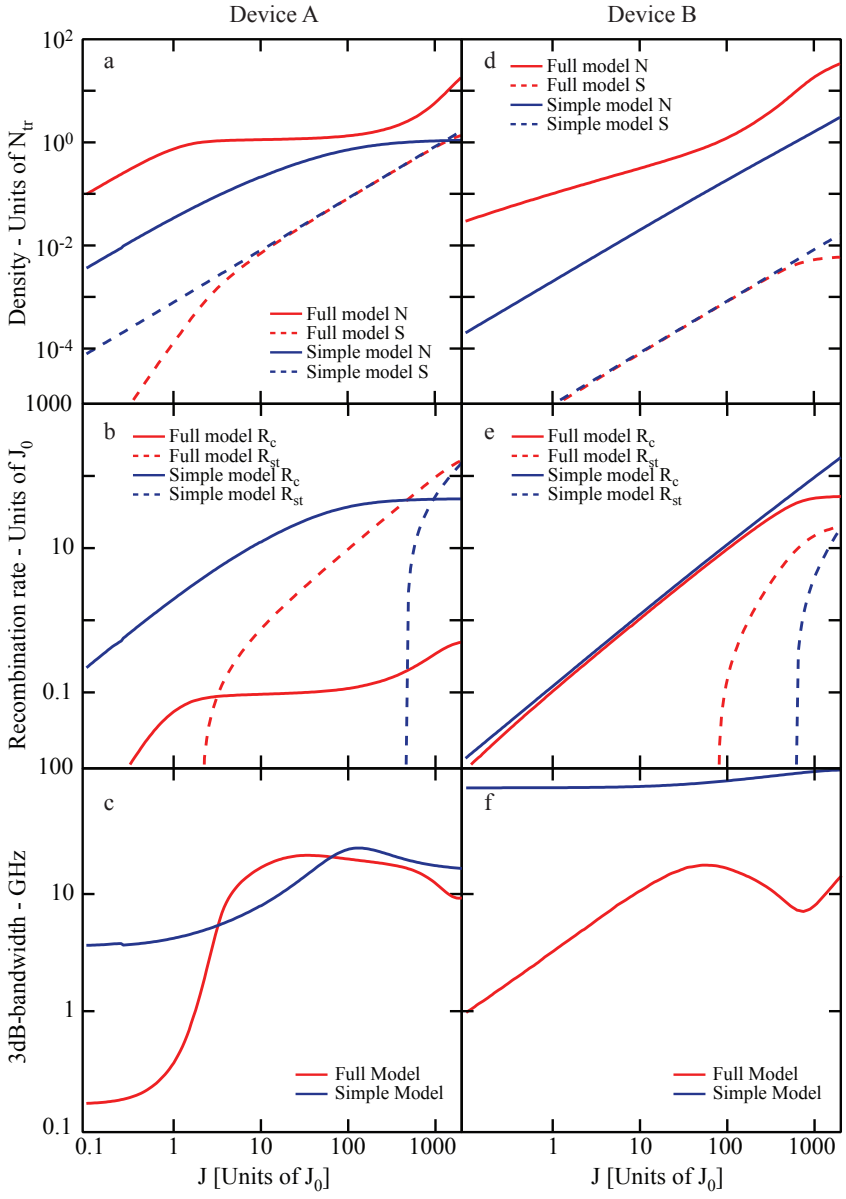

Fig. 4.5: Results from device A with $Q = 10^4$ and $V_n = 10$ and device B with $Q = 10^2$ and $V_n = 0.1$ plotted against pump (in units of $J_0 = \frac{N_{tr}}{\tau_{sp}}$). a) The carrier (solid) and photon (dashed) densities for device A, b) the spontaneous (solid) and stimulated (dashed) emission for device A and c) the 3dB-bandwidth for device A. d-f) are the same as a-c) but for device B. Both the full model (red) and the simple model (blue) are shown. *Parameters in tables E.3 and E.4.*

for $P_0 \sim \varepsilon_{SHB}^{-1} \sim 0.05 N_{tr}$ and must be compensated by an increase of the linear gain. The β-factor is close to unity for the entire pumping range, which explains why the photon densities for the two models are equal for $J > 10J_0$ even though the simple model is dominated by spontaneous emission, while the full model is dominated by stimulated emission.

Figure 4.5b compares the spontaneous and stimulated emission for the two models. In the full model the spontaneous emission increases strongly until the carrier density clamps, where after the stimulated emission becomes dominant. The spontaneous emission remains constant until $J \sim 100J_0$, where the carrier density begins to increase again due to the gain suppression effect discussed above. In the simple model, the carrier density is much lower than in the full model, giving a lower stimulated emission. This pushes the threshold pump up to around $J \sim 1000J_0$.

Several features observed in figure 4.5a and b are also found in the 3dB-bandwidth in figure 4.5c. In the full model, the 3dB-bandwidth is dominated by spontaneous emission until $J \sim J_0$, after which stimulated emission dominates until gain suppression becomes important around $J \sim 100J_0$. Over the entire pumping range the 3dB-bandwidth does not exceed 20 GHz. In the simple model, the high 3dB-bandwidth for $J < 100J_0$ is due to the high spontaneous emission and the drop-off for $J > 100J_0$ is due to the damping rate (γ_R) increasing more rapidly than the resonance frequency (ω_R) as explained in ref. [26].

The results for device B are shown in figure 4.5d-f, where both the Q-factor and mode volume, V_n, are 100 times lower than in device A, so that F_{eff} remains ~ 610 in the simple model, but changes to ~ 70 in the full model (for low carrier density). For this device, the photon loss is 100 times larger than for device A and therefore the photon densities for the two models in figure 3d are 100 times lower. In the simple model, the relatively lower photon density is reflected in the carrier density, which is also lowered to balance the photon loss. In the full model, the carrier density is only slightly lower than for device A for $J < J_0$. This is because the spontaneous emission rate in the full model follows another dependence on N (approximately N^2, see eqn. (3.42)) than in the simple model and therefore a smaller adjustment of N is necessary to compensate the lower photon density.

In figure 4.5e the spontaneous emission rate in the simple model is lower by a factor corresponding to the lowering of carrier density compared with device A. In the full model, the spontaneous emission almost follows the increase in F_{eff}, but is also modified by the lower carrier density. In neither models, the gain becomes large enough to initiate lasing and this is reflected in the carrier densities, which do not clamp in this device.

Figure 4.5f shows that the 3dB-bandwidth calculated in the two models differs significantly. The 3dB-bandwidth is almost an order of magnitude lower in the

full model compared to the simple model. This can be explained by studying eqn. (4.22) in the LED regime, i.e. for dominating spontaneous emission. For the simple model eqn. (4.22) reduces to

$$f_{3dB} \approx \frac{1}{2\pi} \frac{1}{\sqrt{\tau_p^2 + \tau_{eff}^2}} \tag{4.28}$$

with the effective carrier lifetime

$$\frac{1}{\tau_{eff}} \approx \frac{F}{\tau_{sp}} \tag{4.29}$$

Thus, the high bandwidth observed in figure 4.5f is due to the Purcell factor growing large. In the full model, the 3dB-bandwidth is also given by eqn. (4.28), but in this model we have

$$\frac{1}{\tau_{eff}} = F_{eff} \frac{dR_{bulk}}{dN} + \frac{dF_{eff}}{dN} R_{bulk} + \frac{dR_b}{dN} + \frac{1}{\tau_{nr}} \tag{4.30}$$

where we used eqn. (3.36) to separate $R_{c,N}$ into contributions from the effective Purcell enhancement and the recombination in the bulk region. From eqn. (4.28), eqn. (4.30) and figure 3.6a, the behavior of the 3dB-bandwidth in the full model now becomes clear ($J_0 = 1.2 \times 10^3\ \mu\text{m}^{-3}\text{ps}^{-1}$).

For $J < 50J_0$, the effective Purcell factor is almost constant and $R_{b,N} \approx 0$, so that the first term in eqn. (4.30) determines τ_{eff}. For $50J_0 < J < 800J_0$ the term $R_{b,N}$ is still low, while F_{eff} starts to decrease so that the first term of eqn. (4.30) becomes smaller and the second term becomes negative, leading to a decrease in the 3dB-bandwidth. For $J > 800J_0$, the background emission increases sharply, making τ_{eff} decrease and leading to the final increase in the 3dB-bandwidth. Thus, the 3dB-bandwidth in the full model is roughly an order of magnitude lower than in the simple model and this clearly underlines the necessity for a detailed description of the spontaneous emission.

The same analysis can be made for figure 4.5c for $J < 2J_0$, as spontaneous emission is also dominant in this pumping range. Here, the effective Purcell factor in the full model is 100 times lower than for device B, making $\frac{1}{\tau_{nr}}$ the dominating term in eqn. (4.30) and giving the low 3dB-bandwidth compared to device B. Another way of expressing the behavior is that the Purcell enhancement only affects the carriers associated with transitions within the bandwidth of the cavity resonance. When the cavity resonance is much narrower than the electronic bandwidth, the influence from the enhanced spontaneous emission only has a small effect on the total carrier density lifetime and therefore also the speed.

In order to examine the modulation bandwidth for a large range of devices, the 3dB-bandwidth has been calculated in the full model versus Q-factor and mode volume for a range of devices and the result is plotted in figure 4.6 for $J = J_0$ and $J = 100J_0$. The white line in the figure shows, for the given

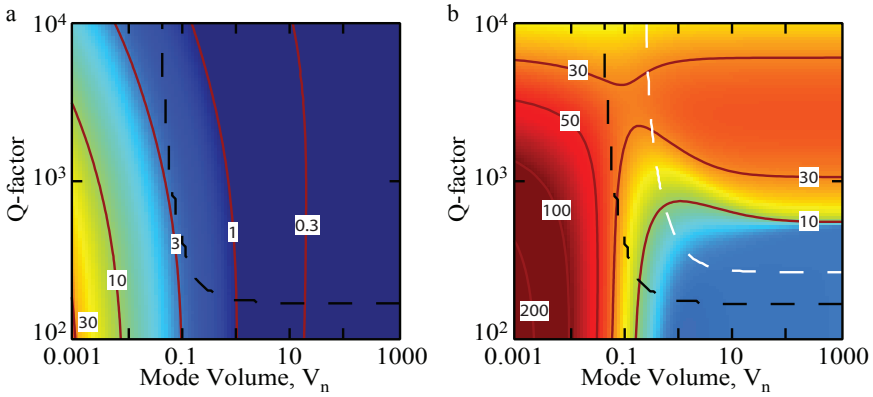

Fig. 4.6: The 3dB-bandwidth for a) $J = J_0$ and b) $J = 100J_0$. The red lines are contours of equal 3dB-bandwidth (numbers in units of GHz). The black line separates the potential laser devices from the LED devices and the white line indicates which of the laser devices have larger stimulated emission than spontaneous emission at the given pump. *Parameters in table E.3*

pump current, the device parameters for which stimulated and spontaneous emission are equal in magnitude. Devices to the right of this boundary are dominated by stimulated emission. The black line shows the limiting value of this boundary for large pump current, i.e. devices to the left of this line will always be dominated by spontaneous emission, independently of the strength of the pump, and are thus always in the LED regime. All the devices in figure 4.6a are dominated by spontaneous emission for the given pump and are therefore in the LED regime. It is seen that the 3dB-bandwidth is below 3 GHz for most devices, except at extremely low mode volumes, which are probably unattainable in practice, where the bandwidth starts to increase. This is due to the effective Purcell factor, which is large at low mode volumes, so that the first term in eqn. (4.30) dominates. The slight dependence on Q is due to the photon life time that becomes smaller at low Q and thereby increases the 3dB-bandwidth in eqn. (4.28).

The same dependence on Q is seen in figure 4.6b, where the 3dB-bandwidth exceeds 200 GHz in the lower left corner, i.e. in the LED regime. In the top right area, which corresponds to conventional laser structures, the effective Purcell factor saturates at a Q of a few hundreds and the stimulated emission therefore becomes the dominant recombination process so that the term $\frac{aP_0}{\tau_p}$ in eqn. (4.26) becomes large, giving the large modulation speed in this area. In the lower right corner, the photon loss is too large to meet the lasing condition and the effective Purcell factor is low, giving the lower 3dB-bandwidth. In general the ultrahigh modulation speeds previously reported [26] are not seen, neither at low or high pump, because the effective Purcell factor saturates and becomes independent of the Q-factor as discussed above.

We note that for two-level structures, such as quantum dot devices, the upper left corner of figure 4.6a and b may correspond to devices operating in the strong coupling regime [38], where the calculated 3dB-bandwidth would be invalid. However, for quantum well structures and operation at room temperature, as considered here, this is not considered to be an issue.

In conclusion, the limited effective Purcell enhancement entails that for devices with mode volumes attainable with today's technology the highest modulation bandwidth is found above threshold and limited by well-known damping effects due to gain nonlinearities [26, 69]. The ultra fast modulation speeds previously reported in ref. [26] are only found in devices with extremely low mode volume and even for these devices, the 3dB-bandwidth is below a few hundred GHz and the spectral bandwidth is very broad making wavelength division multiplexing systems difficult.

In section 4.4, we examine the modulation bandwidth for QD LEDs that can have higher effective Purcell enhancements than is possible for QW devices. As we discuss in that section, this fact leads to modulation bandwidths exceeding those usually found for conventional light emitting devices.

4.3 Random Lasing in Quantum Well Devices

As a specific example of a PhC QW structure, we now investigate lasing from Anderson localized modes in randomized PhC waveguides. We fit experimental data measured at DTU Fotonik by PhD. student Jin Liu using the simple model for spontaneous emission and the logarithmic gain model where the effective Purcell enhancement is included.

In PhC structures, design of cavities with high Q and low mode volume is critically dependent upon the exact position and uniformity of the holes. Even small deviations from the design position of the holes can drastically reduce the theoretically possible values. Due to imperfections in the fabrication procedures, small variations in the parameters for the individual hole (position, roundness, etc.) is always present and much effort have gone into reducing the fabrication noise.

It has been shown in PhC waveguides that if the fabrication disorder is enhanced rather than suppressed, Anderson localized modes are formed [70–72]. Anderson localized modes appear in randomly disordered structures, where scattering of the holes can capture the light in random closed paths. Due to the inherent randomness of this approach, exact predictions about the location and quality of the modes are difficult. However, for large enough structures, the probability of having a cavity with the desired Q factor and mode volume becomes reasonable high.

The structures studied here were fabricated at DTU Fotonik and consist of InGaAsP PhC waveguides, where the position of the holes is varied randomly

from the perfect regularity following a Gaussian distribution with 1 % standard deviation [72]. Embedded in the PhC membrane are 10 layers of QWs that provide carriers for recombination. Figure 4.7a (top) shows a Scanning Electron Microscopy (SEM) image of a waveguide with lattice constant $a = 380$ nm and radius $r = 0.26a$ and figure 4.7a (middle) displays FDTD calculations of the modes of a corresponding random waveguide. Optically pumping the structure from above with a pulsed laser and measuring the photoluminescence as a function of wavelength and position, the hotspots indicated in figure 4.7a (bottom) were found. Each hotspot corresponds to an Anderson localized mode within the waveguide. Several structures were fabricated and for each structure the I/O curves from promising modes were measured [72].

The data is fitted using the LRE model (eqns. (3.48) and (3.49)), but as the optical DOS for a PhC waveguide is different from the DOS presented in figure 3.3, the recombination rate will have a different behavior than discussed in section 4.1. Instead of the full model, we use the linearized form of the simple model for the spontaneous emission (eqns. (3.4) and (3.5)), which is permissible for laser structures close to threshold[2]. We multiply the effective Purcell enhancement onto the expression for the gain in eqn. (3.54), so that the Purcell effect is qualitatively taken into account in the recombination rates. Non-radiative recombination is included so that the rates are given by [72]

$$R_{nr} = \frac{N}{\tau_{nr}} \tag{4.31}$$

$$R_c = F_{eff}\frac{N}{\tau_{sp}} \tag{4.32}$$

$$R_b = \left(\frac{1}{\beta} - 1\right) R_c \tag{4.33}$$

$$R_s = F_{eff} v_g G_0 \ln\left(\frac{N}{N_{tr}}\right) P \tag{4.34}$$

$$R_p = \frac{N}{\tau_p} \tag{4.35}$$

Thus, both spontaneous and stimulated emission are enhanced with the effective Purcell factor, F_{eff}, which is expected to be reduced from the ideal case Purcell factor, F, due to the presence of the broad QW electronic DOS. The β-factor is a fixed number and the emission to the background is calculated using eqn. (4.33). Using this model and F_{eff} and β as fitting parameters, the measured data are fitted using the least squares method. The Q-factor was extracted from the photoluminescence data. A pulsed injection current density was used to mimic the experiment and the output photon density was scaled to fit the data due to the presence of unknown quantities (absorption of pump, pumped area, quantum efficiency, etc.) An example of the measured data ($Q = 1600$) with fitted I/O curve is shown in figure 4.7b.

[2] The fitting was done using both the bimolecular expression for the spontaneous emission as well as the linearized form, however, both models were found to fit the data equally well. In order to keep the model as simple as possible, the linearized spontaneous emission model was used.

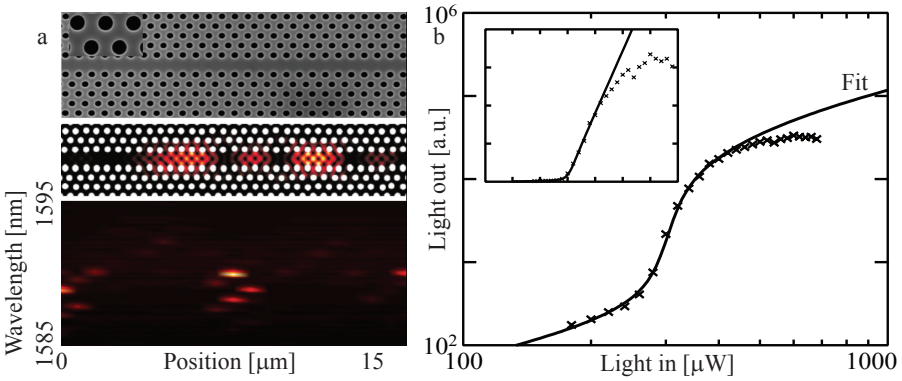

Fig. 4.7: a) SEM image of a waveguide with a random distribution of hole positions (top), FDTD simulations of the modes in a similar structure (middle) and photoluminescence measurements of the modes (bottom). b) I/O curve for an Anderson localized mode in a random PhC waveguide. The measured data (crosses) are fitted using the LRE model (solid). The inset shows the I/O curve on a linear scale. *Parameters in table E.5. Experimental data by courtesy of Jin Liu.*

The model fits the data very well using the parameters in table E.5 except at high pump where the experimental I/O curve saturates due to heating effects that are not included in the LRE model. The fit gives $F_{eff} = 2.5$ and $\beta = 0.13$, which is reasonable for this type of structure. The threshold is estimated by extrapolating the above threshold slope in the linear plot to intersect with the abscissa. In this case, it is close to 300 μW.

Due to the randomness of the Anderson localized modes, a single device is not necessarily representative for the possible cavity parameters. To gain more insight into the localized modes of the structure, 30 individual I/O curves were measured and F_{eff}, β and threshold parameters was extracted by fitting with the LRE model. In figure 4.8, the measured Q and extracted parameters are presented in histograms showing the distribution of the parameters.

The Q and β-factors lie in a range that is expected for nanocavity lasers with maxima around 1000-2000 and 0.05-0.1, respectively. The Purcell enhancement is relatively large compared to what is expected from the discussion of the reduction of the Purcell enhancement in QW devices in section 3.4. Of course, the mode volume is not known in the Anderson localized modes and it is possible that the effective Purcell enhancement stems from a generally low mode volume of this type of mode. If we speculate that the cavity with the best properties will always be the first to lase when an entire waveguide is pumped, then it would probably be the cavities with the lowest mode volume as low mode volume is more important for the effective Purcell enhancement in QW devices. In that case, high effective Purcell enhancements should be expected

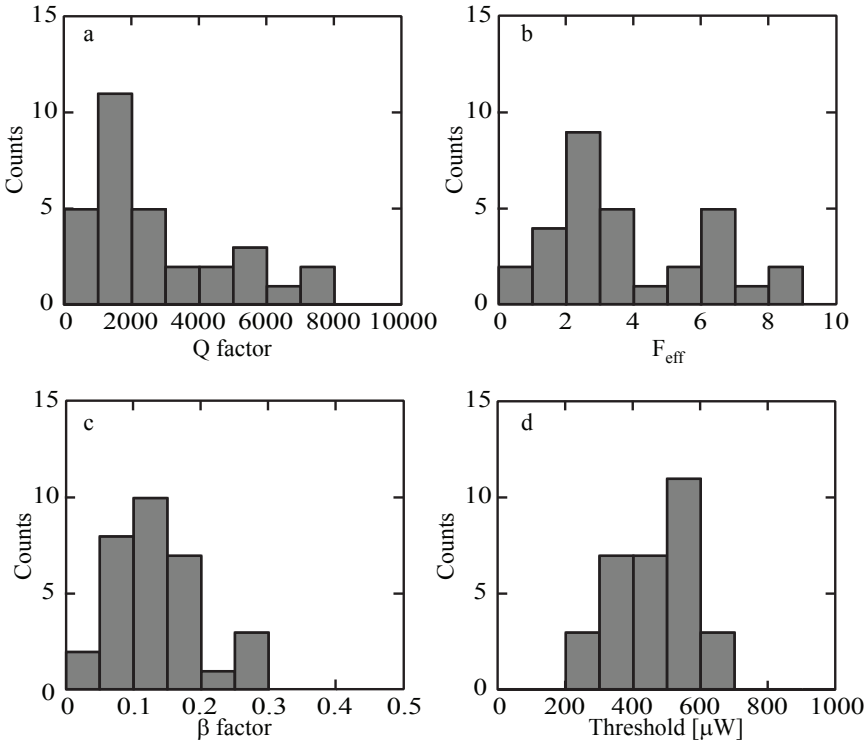

Fig. 4.8: Histograms showing a) Q-factor b) F_{eff} c) β-factor and d) threshold pump power extracted from 30 measured I/O curves. *Parameters in table E.5. Experimental data by courtesy of Jin Liu.*

for large enough waveguides. Alternatively, the high effective Purcell enhancements could be explained by sharp features in the electronic DOS, which will relax the reduction of the F_{eff}. A third possibility is that the optical DOS of the real Anderson localized waveguide mode is too different from the simple Lorentzian form used in section 3.4 for the same conclusions to hold. It is possible that Anderson localized modes do not experience the same reduction of the Purcell enhancement as defect PhC cavities. This could be examined by using an optical DOS that mimics the expected features of the waveguide system, however, due to time constraints, this was not implemented.

4.4 Quantum Dot Devices

Using the same techniques as in section 4.1, we now investigate QD devices. As mentioned in chapter 3, the QDs differ from the QWs through the electronic DOS, which for the QD case consist of a narrow peak. The width of the peak is controlled by the homogeneous and inhomogeneous broadening. The homogeneous broadening is dominated by dephasing due to random phonon collisions and is difficult to affect except by changing the temperature [73].

The inhomogeneous broadening, on the other hand, is controllable to some extend through better fabrication techniques. At the moment, QD samples grown using self-assembled growth display relatively large inhomogeneous broadening of the order of 10 meV [37]. Much work is going into reducing the inhomogeneous broadening and it is reasonable to assume that the future will bring better QD samples with much narrower energy distributions. In the following, we will therefore investigate the requirements of the degree of inhomogeneous broadening necessary to realize ultra fast QD devices.

As shown in section 4.2, the modulation bandwidth of QW devices is severely limited due to the reduction of the effective Purcell effect. However, this reduction is less pronounced in QD devices due to the relatively narrower electronic DOS. We therefore now examine the modulation speed of QD based nanoLEDs and establish necessary conditions to achieve high modulation speed. We limit the scope to below threshold operation, where spontaneous emission dominates the recombination processes [74].

We consider an ensemble of QDs embedded in a high Q cavity and model the dynamics using the rate equations in eqns. (3.48) and (3.49) with the recombination rates given by

$$R_{nr} = 0 \tag{4.36}$$
$$R_{st} = 0 \tag{4.37}$$
$$R_p = \frac{P}{\tau_p} \tag{4.38}$$

The spontaneous emission rates, R_c and R_b, are given by eqn. (3.50) and (3.51), respectively. For the electronic DOS, eqn. (3.25) was used and the optical DOS is given by (3.34).

From this model, we calculate the 3dB-bandwidth below threshold using the small-signal analysis presented in section 4.1, where the matrix elements are expressed as

$$\gamma_{NN} = \partial_N R_c + \partial_N R_b \tag{4.39}$$
$$\gamma_{NP} = 0 \tag{4.40}$$
$$\gamma_{PN} = \Gamma \partial_N R_c \tag{4.41}$$
$$\gamma_{PP} = \partial_P R_p \tag{4.42}$$

With these matrix elements, the relaxation frequency and damping are $\omega_R^2 = \gamma_{NN}\gamma_{PP}$ and $\gamma_R = \gamma_{NN} + \gamma_{PP}$, so that the 3dB-frequency in eqn. (4.22) reduces

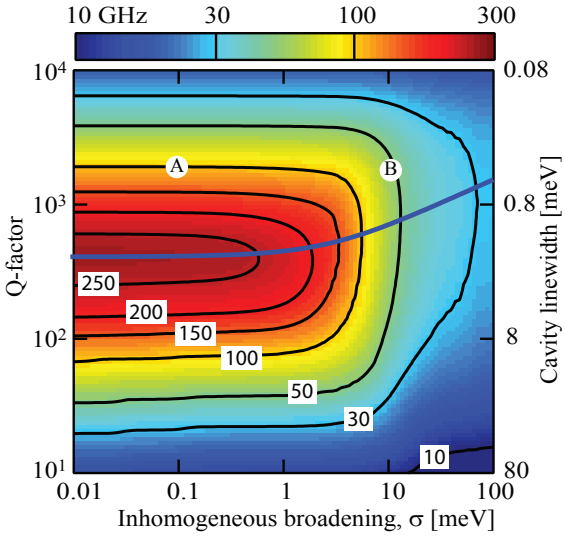

Fig. 4.9: The maximum 3dB-frequency for a range of quantum dot LEDs with different Q-factors and inhomogeneous widths and a homogeneous broadening of 100 μeV. The contours mark equal bandwidths in GHz and the optimal Q-factor is marked by a blue line. Also marked are devices A and B. *Parameters in table E.6.*

to

$$\begin{aligned} f_{3dB} &= \frac{1}{2\pi}\sqrt{-\frac{1}{2}\left(\gamma_{NN}^2+\gamma_{PP}^2\right)+\sqrt{\frac{1}{4}\left(\gamma_{NN}^2+\gamma_{PP}^2\right)^2+\gamma_{NN}^2\gamma_{PP}^2}} \\ &= \frac{1}{2\pi}\sqrt{-\frac{1}{2}\left(\gamma_{NN}^2+\gamma_{PP}^2\right)+\frac{1}{2}\left(\gamma_{NN}^2+\gamma_{PP}^2\right)\sqrt{1+\frac{4\gamma_{NN}^2\gamma_{PP}^2}{\left(\gamma_{NN}^2+\gamma_{PP}^2\right)^2}}} \\ &\approx \frac{1}{2\pi}\sqrt{\frac{\gamma_{NN}^2\gamma_{PP}^2}{\gamma_{NN}^2+\gamma_{PP}^2}} = \frac{1}{2\pi}\left[\frac{1}{\gamma_{NN}^2}+\frac{1}{\gamma_{PP}^2}\right]^{-\frac{1}{2}} \\ &= \frac{1}{2\pi}\left[\tau_{eff}^2+\tau_p^2\right]^{-\frac{1}{2}} \end{aligned} \tag{4.43}$$

where $\frac{1}{\tau_{eff}} = \partial_N R_c + \partial_N R_b$. Using this expression, the 3dB-frequency can be calculated.

We use the transparency condition ($f_c = \frac{1}{2}$) as a lower bound for the threshold and plot the maximum modulation speed below this value to ensure that we are in the LED regime. The result is displayed in figure 4.9 for a range of Q-factors and inhomogeneous widths using the parameters in table E.6. We here choose a value for homogeneous broadening appropriate for low temperature and low density in order to be able to see the effect of inhomogeneous broadening [73].

Two interesting trends are seen: 1) When increasing the Q-factor, the 3dB-frequency goes through a maximum at $Q \sim 500$. The initial rise is due to the Purcell enhancement increase with Q. The decrease at large Q-factors is an intrinsic feature of all resonators and is due to the photon lifetime becoming large, prohibiting fast operation. 2) When increasing the inhomogeneous broadening above ~ 0.5 meV, the 3dB-frequency decreases, whereas it is almost constant below ~ 0.5 meV. Both features can be understood from the small-signal expression for the 3dB-bandwidth in eqn. (4.43). Below transparency, τ_{eff} is well described by $\partial_N R_b = 0$ and $\partial_N R_c = 2BN_0$. Here, N_0 is the steady-state carrier density and B can be approximated by (using eqn. (3.27))

$$B = \frac{F}{\tau_{21}\rho_{QD}} \frac{\Gamma_p}{\Gamma_p + \gamma + \sigma'} \tag{4.44}$$

where τ_{21} is the electron-hole recombination time for two states in bulk as defined in ref. [31], ρ_{QD} is the 3D density of dots, $\Gamma_p = \frac{2\hbar}{\tau_p}$ is the cavity linewidth and the linewidth $\sigma' = 2\sqrt{2\ln(2)}\sigma$ is chosen as to match the inhomogeneous broadening. At low Q-factors, f_{3dB} is governed by $\frac{1}{\tau_{eff}}$, which increases with Q, but at high Q-factors the bandwidth is limited by the term $\tau_p = \frac{Q}{\omega_c}$. The Q-factor giving the maximum bandwidth is found for $\partial_Q f_{3dB} = 0$ which for $\gamma + \sigma' << \Gamma_p$ equals

$$Q_{opt} = \sqrt{\frac{\pi^2}{6}\omega_c \tau_{21} V_n} \tag{4.45}$$

where we took $N_0 = \frac{\rho_{QD}}{2}$. In figure 4.9, Q_{opt} is indicated by the blue line and is seen to deviate from the value in eqn. (4.45) when $\gamma + \sigma'$ becomes comparable to Γ_p. For increasing inhomogeneous broadening, eqns. (4.43) and (4.44) reproduce the decrease observed in figure 4.9 for large σ.

Figure 4.10 plots f_{3dB} and the recombination rates against the injection current density for the two devices marked in figure 4.9, one with $\sigma = 100$ μeV (device A) and one with $\sigma = 10$ meV (device B), both with $Q = 2000$. The arrows in figure 4.10 indicate lower bounds on the threshold, namely where $f_c = \frac{1}{2}$, indicating the validity range of the present model. The 3dB-frequency for device A is seen to increase with J until it becomes limited by the photon lifetime and the spontaneous recombination is dominated by emission into the cavity. For device B, R_c increases with J until the quasi Fermi level separation becomes larger than the cavity resonance energy. After this point, R_c becomes constant and R_b rises sharply. This is reflected in f_{3dB} which goes through a maximum and then decreases as $\partial_N R_c \to 0$ (c.f. eqn. (4.43)). The final increase is due to R_b that becomes large when the wetting layer states become important.

In figure 4.11, we plot f_{3dB} for the same range of Q-factors and σ as in figure 4.9, but for a homogeneous broadening, γ, of 10 meV corresponding to room temperature operation [73]. The same general dependence on Q and σ is seen, but the maximum 3dB-bandwidth is significantly lower. The modulation bandwidth is seen to become independent of the inhomogeneous broadening, σ, for

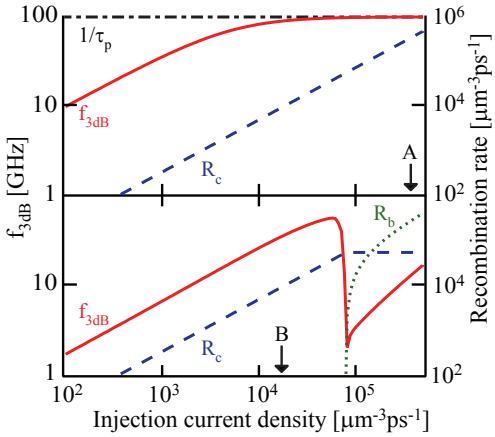

Fig. 4.10: The 3dB-bandwidth (red solid), R_c (blue dashed) and R_b (green dotted) at $Q = 2000$ for an inhomogeneous broadening of 100 μeV (device A, top) and 10 meV (device B, bottom). The black line (dot-dashed) indicates the photon life time limit and the arrows indicate the transparency current for A and B. For device A, $R_b < 100$ m^{-3}ps^{-1} and is therefore not shown. *Parameters in table E.6.*

$\sigma \ll \gamma$. Note that f_{3dB} continues to increase even for $\sigma < \gamma$ as the width of the distribution is inversely proportional to $\gamma + \sigma$ (c.f. eqn. (4.44)).

Figures 4.9 and 4.11 show that modulation speeds of QD nanoLEDs are comparable to conventional diode performance even with today's technology. However, much higher modulation bandwidths are theoretically possible if the QD linewidth can be reduced.

4.5 Comparison to Cluster Expansion Model

As a check of the validity of the full LRE model, we now compare calculated results to the microscopic Cluster Expansion Model (CEM) which was outlined in section 3.7. The CEM starts from the Schrödinger equation where all processes and interactions are included through the Hamiltonian. This is a fundamentally different approach from the phenomenological LREs. The CEM accurately models more features of laser devices than the LREs, but is also computationally more demanding. The LRE model, on the other hand, is comparatively easily solved on a modern computer and analysis of the equations is also tractable. A comparison of the two models therefore has two objectives: 1) A sanity check of the modifications made to the LREs, which is the best alternative in lieu of an experimental comparison and 2) a deeper understanding of the results from the CEM, which can be obtained from analytical results of the LRE model in the regions where the two models agree.

A few modifications are necessary before the models can be expected to yield

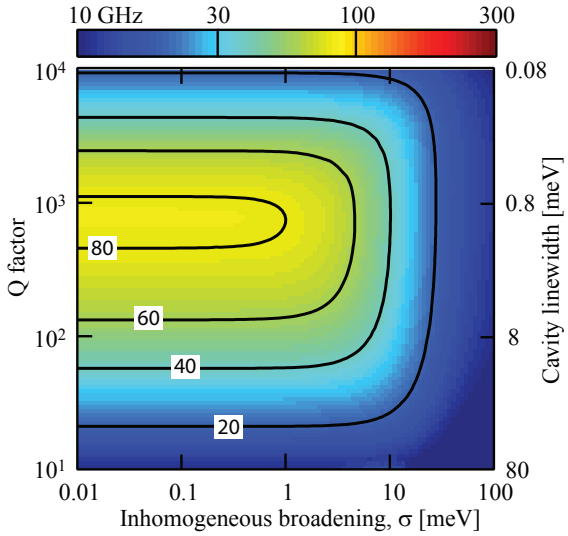

Fig. 4.11: The maximum 3dB-frequency for a range of quantum dot LEDs with different Q-factors and inhomogeneous widths and a homogeneous broadening of 10 meV. The contours mark equal bandwidths in GHz and the optimal Q-factor is marked by a blue line. Also marked are devices A and B. *Parameters in table E.6.*

comparable results [75]. First, the β-factor, which in the CEM is a fixed number that can be chosen freely, is in the LRE model calculated as the ratio of the spontaneous emission into the cavity to the total spontaneous emission. In the LRE model, the β-factor varies significantly across the pumping range of interest (c.f. figure 4.1) and will result in different steady-state behavior than in the CEM. The β-factor does not enter the PESE terms and will therefore not change that part of the comparison. We therefore fix β in the LRE model to the value used in the CEM. The background emission is then determined from R_c and the definition of β as

$$R_b = \left(\frac{1}{\beta} - 1\right) R_c \tag{4.46}$$

A drawback of this approach is that the background emission is limited for large carrier densities because of the bandfilling effect discussed in connection with figure 3.4. This is mainly an issue for devices where the photon loss is larger than the maximum gain, i.e. for non-lasing devices, as the carrier density clamps at the threshold carrier density for lasing devices. In this comparison, we therefore restrict ourselves to lasing devices.
The second modification is to assume instantaneous carrier scattering in the CEM pumping term by setting the scattering rate s (infinitely) large. This is necessary because the present LRE model only includes one QD level and assumes the carriers to follow a Fermi distribution.

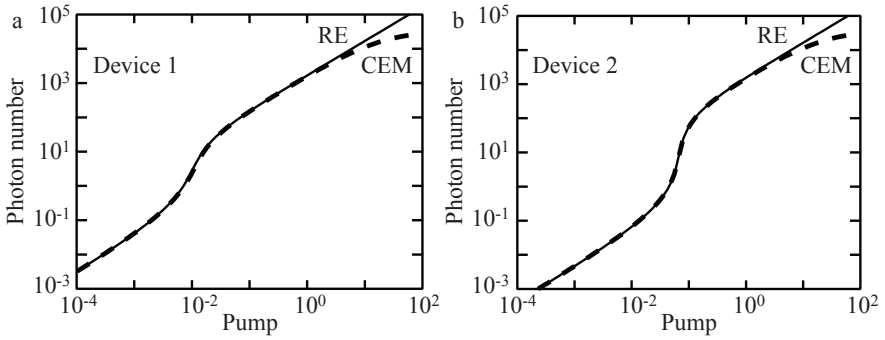

Fig. 4.12: The I/O curve for device 1 (left) and 2 (right) calculated using the LRE model (solid) and the CEM (dashed). *Parameters in tables E.7 and E.8.*

With these modifications to the models in sections 3.6 and 3.7, the calculated quantities are connected by the following expressions

$$J = \frac{2N_{QD}}{V_a} p \tag{4.47}$$

$$N = \frac{N_{QD}}{V_a} f_s \tag{4.48}$$

$$P = \frac{n_p}{V} \tag{4.49}$$

$$R = \frac{N_{QD}}{V_a} r \tag{4.50}$$

where the last line connects rates in the LRE model to rates in the CEM. Note that as electrons scatter into the s-state from two p-states in the CEM, eqn. (4.47) must have the extra factor of 2.

Two devices were chosen for the comparison. Device 1 has a Purcell factor of 25 and a β-factor of 0.3 and device 2 has $F = 50$ and $\beta = 0.1$ and both have $Q = 10000$, $\Gamma_H = 100$ μeV and $N_{QD} = 100$ (Parameters for the two devices are listen in tables E.7 and E.8 in appendix E). The inhomogeneous broadening was assumed to be negligible small ($\sigma = 1$ μeV) and the mode volume was calculated based on the values for the Purcell factor and Q as

$$V_n = \frac{6}{\pi^2} \frac{Q}{F} \tag{4.51}$$

The confinement factor is given in terms of the active and modal volumes ($\Gamma = \frac{V_a}{V}$).

In figure 4.12, the I/O curves for device 1 and 2 calculated in the two models are shown. The models yield identical I/O curves except at high pump ($p > 10$ ps^{-1}), where the CEM curve saturates due to Pauli blocking. The LRE model does not encompass this effect and the I/O curve can therefore continue to increase linearly in the high pumping regime. The near perfect

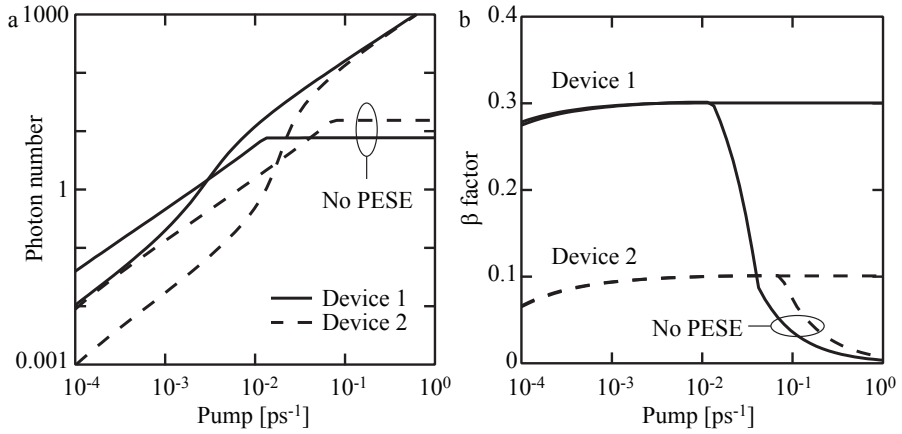

Fig. 4.13: a) The I/O curves for device 1 (solid) and 2 (dashed) calculated using the LRE model both with and without Purcell enhancement of the stimulated emission. b) The β-factors corresponding to the I/O curves in a). *Parameters in tables E.7 and E.8.*

agreement between the I/O curves indicates that the inclusion of Purcell enhancement in stimulated emission is indeed necessary for nanocavity devices. This is underlined by figure 4.13a where the I/O curves for device 1 and 2 are calculated in the LRE model both with and without enhancement of the stimulated emission. It is evident that inclusion of the Purcell factor in stimulated emission is vital, as the non-enhanced devices in this case do not reach lasing. As mentioned above, the β-factor is fixed in the simplified LRE model for the comparison, which limits the comparison to lasing devices. For this reason the data in figure 4.13a have been calculated using a varying β-factor, i.e. by calculating R_c and R_b independently. The resulting β-factors are shown in figure 4.13b. For both devices, the optical DOS has been modified to ensure a β-factor at threshold that corresponds to the CEM value. For the devices with PESE, the β-factor saturates when threshold is reached as the carrier density clamps. The devices without PESE experience a sharp drop in the β-factor that corresponds to the background emission increasing rapidly when the bandfilling effect for R_c appears (c.f. figure 3.4).

The dynamical properties of device 1 and 2 are summarized in figure 4.14 where the modulation response is displayed. Figure 4.14a shows that the 3dB-frequencies for device 1 are similar in the two models. At high pump values, the LRE model predicts a 3dB-frequency that is limited by the cavity lifetime. This deviates from the CEM result, which gives a slightly decreasing modulation bandwidth. The discrepancy can be explained by the pump saturation in the CEM, which also was evident in the corresponding I/O curve. At low pump values, both models predict a steady increase in bandwidth following the pump. Close to threshold a rapid jump to the above threshold value is observed, but the details of the near-threshold behavior is different in the models. The dif-

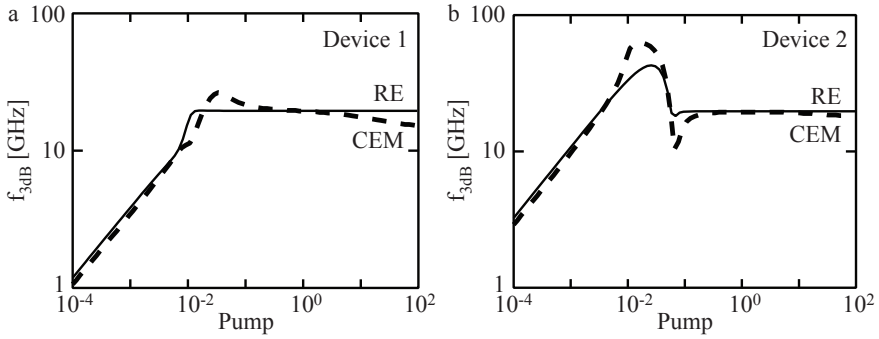

Fig. 4.14: a) The 3dB-frequency for device 1 and b) 2 calculated using the LRE model (solid) and the CEM (dashed). *Parameters in tables E.7 and E.8.*

ference can be explained by the fact that the CEM includes non-Markovian effects (see eqn. (3.64)), which affect the dynamical properties even if they are not affecting the I/O curve.

In figure 4.14b, the modulation bandwidth for device 2 is shown. Overall it follows the same behavior as device 1, except that the below threshold 3dB-frequency is significantly higher than for device 1 and the near-threshold behavior is different. Just below threshold, both models predict a maximum in the modulation bandwidth that exceeds the limit set by the cavity lifetime. At threshold a small dip in f_{3dB} is observed. To understand this behavior, we need to examine the small-signal expression for the model.

Approximate analytical expressions can be derived for special pumping regimes using a simplified version of the CEM. The simplifications consist of the assumptions $f_p = f_p^h$ and $f_s = f_s^h$, neglecting the higher order correlations in eqn. (3.64) and replacing the CEM pumping term $2s\,(1 - f_s)\,f_p$ by J_p, effectively neglecting Pauli blocking. With these modifications, the steady-state photon assisted polarization can be written

$$\left\langle b^\dagger v^\dagger c \right\rangle = \frac{1}{\kappa + \gamma} \left(f_s^2 + (2f_s - 1) n_p \right) \tag{4.52}$$

This results in a simplified version of eqns. (3.60)-(3.62) that can be written in a form that is similar to the LREs

$$\dot{f}_s = J_p - (\alpha + \delta)\, f_s^2 - \alpha\,(2f_s - 1)\, n_p \tag{4.53}$$

$$\dot{n_p} = \alpha N_{QD} \left(f_s^2 + (2f_s - 1)\, n_p \right) - \frac{2\kappa}{\hbar} n_p \tag{4.54}$$

where

$$\alpha = \frac{F}{\tau_{bulk}} \frac{\kappa}{\kappa + \gamma} \tag{4.55}$$

$$\delta = \frac{F}{\tau_{bulk}} \left(\frac{1}{\beta} - 1 \right) \tag{4.56}$$

Linearizing the equations as in section 4.1, the matrix elements can be written as

$$\gamma_{ff} = 2(\alpha + \delta) f_s + 2\alpha n_p \tag{4.57}$$
$$\gamma_{fn} = \alpha(2f_s - 1) \tag{4.58}$$
$$\gamma_{nf} = 2\alpha N_{QD}(f_s + n_p) \tag{4.59}$$
$$\gamma_{nn} = \frac{2\kappa}{\hbar} - \alpha N_{QD}(2f_s - 1) \tag{4.60}$$

The 3dB-frequency is calculated as

$$\omega_R^2 = \gamma_{ff}\gamma_{nn} + \gamma_{fn}\gamma_{nf} \tag{4.61}$$
$$\gamma_R = \gamma_{ff} + \gamma_{nn} \tag{4.62}$$
$$f_{3dB} = \frac{1}{2\pi}\sqrt{\omega_R^2 - \frac{\gamma_R^2}{2} + \sqrt{\left(\omega_R^2 - \frac{\gamma_R^2}{2}\right)^2 + \omega_R^4}} \tag{4.63}$$

It turns out that in most cases $\gamma_R \gg \omega_R$ and we can use the approximation

$$f_{3dB} \approx \frac{1}{2\pi}\frac{\omega_R^2}{\gamma_R} = \frac{1}{2\pi}\frac{\gamma_{ff}\gamma_{nn} + \gamma_{fn}\gamma_{nf}}{\gamma_{ff} + \gamma_{nn}} \tag{4.64}$$

Above threshold, we have $n_p \gg f_s$ which allows for the following approximations

$$\gamma_{ff} \approx 2\alpha n_p \tag{4.65}$$
$$\gamma_{nf} \approx 2\alpha N_{QD} n_p \tag{4.66}$$
$$\gamma_{nn} \approx 0 \tag{4.67}$$

The last approximation is clear from the above threshold steady-state equation for n_p, i.e.

$$\dot{n}_p = \alpha N_{QD}\left(f_s^2 + (2f_s - 1) n_p\right) - \frac{2\kappa}{\hbar} n_p = 0$$
$$0 \approx \alpha N_{QD}(2f_s - 1) - \frac{2\kappa}{\hbar} \tag{4.68}$$

Thus, we have

$$f_{3dB} \approx \frac{1}{2\pi}\frac{\gamma_{fn}\gamma_{nf}}{\gamma_{ff}} = \frac{1}{2\pi}\frac{\alpha(2f_s - 1)\, 2\alpha N_{QD} n_p}{2\alpha n_p}$$
$$= \frac{1}{2\pi}\alpha N_{QD}(2f_s - 1) = \frac{1}{2\pi}\frac{2\kappa}{\hbar} = \frac{1}{2\pi}\frac{1}{\tau_p} \tag{4.69}$$

This corresponds exactly to the observed above threshold behavior when Pauli blocking is neglected.

Below threshold it is found that $\gamma_{ff}\gamma_{nn} \gg \gamma_{fn}\gamma_{nf}$, so that we can write

$$f_{3dB} \approx \frac{1}{2\pi}\frac{\gamma_{ff}\gamma_{nn}}{\gamma_{ff} + \gamma_{nn}} = \frac{1}{2\pi}\left[\frac{1}{\gamma_{ff}} + \frac{1}{\gamma_{nn}}\right]^{-1} \tag{4.70}$$

This expression for the below threshold bandwidth resembles closely eqn. (4.43), which was derived in section 4.4 for a QD nanoLED. Equation (4.70) is governed by the matrix elements γ_{ff} and γ_{nn}, the latter of which can be rewritten as $\gamma_{nn} = \frac{\alpha N_{QD} f_s^2}{n_p}$. For below threshold operation where the photon density is low, γ_{nn} will be larger than γ_{ff} and eqn. (4.70) therefore simplifies to

$$\begin{aligned} f_{3dB} &\approx \frac{1}{2\pi}\gamma_{ff} = \frac{1}{2\pi} 2\left(\alpha+\delta\right) f_s + 2\alpha n_p \\ &\approx \frac{1}{2\pi} 2\delta f_s \end{aligned} \tag{4.71}$$

where the last approximation is valid for $\alpha \ll \delta$, which is the case for low β-factors. From eqn. (4.71), we can see that for devices with sufficiently low β, the below threshold behavior is governed by the spontaneous emission into the background. This is reflected in the difference between the 3dB-frequency for device 1 ($\beta = 0.3$) and 2 ($\beta = 0.1$), where f_{3dB} is significantly higher for the low β device. For sufficiently low β and high F, the below threshold 3dB-frequency can even surpass the cavity photon loss, which usually determines the upper limit of the bandwidth. This gives rise to the maximum in figure 4.14 which can be found from $\frac{df_{3dB}}{df_s} = 0$

$$f_{s,max} = \frac{1}{2} \frac{1 + \frac{2\kappa}{\hbar \alpha N_{QD}}}{1 + \sqrt{\frac{\delta}{\alpha N_{QD}}}} \tag{4.72}$$

The maximum f_{3dB} can be found by inserting eqn. (4.72) back into eqn. (4.70), but it does not result in a simple expression.

Equations (4.69) and (4.71) closely reproduce the behavior of the 3dB-frequency sufficiently far away from threshold. The dip in the 3dB-frequency at transparency can also be approximately described by assuming $\gamma_{ff} \gg \gamma_{nn}$, which is fulfilled close to threshold. Then

$$f_{3dB} \approx \frac{1}{2\pi}\left(\gamma_{nn} + \frac{\gamma_{fn}\gamma_{nf}}{\gamma_{ff}}\right) \tag{4.73}$$

where we have from the steady-state equations and eqns. (4.57)-(4.60)

$$\gamma_{nn} = \frac{2\kappa}{\hbar} - \alpha N_{QD}\left(2f_s - 1\right) = \alpha N_{QD} \frac{f_s^2}{n_p} \tag{4.74}$$

$$\frac{\gamma_{fn}\gamma_{nf}}{\gamma_{ff}} = \frac{2\alpha^2 N_{QD}\left(2f_s-1\right)\left(f_s+n_p\right)}{2\left(\alpha+\delta\right)f_s + 2\alpha n_p} = \frac{\frac{2\kappa}{\hbar} - \alpha N_{QD}\frac{f_s^2}{n_p}}{1 + \frac{\delta}{\alpha}\frac{f_s}{f_s+n_p}} \tag{4.75}$$

Thus, the 3dB-bandwidth becomes

$$f_{3dB} \approx \frac{1}{2\pi} \frac{\frac{2\kappa}{\hbar} + \alpha N_{QD}\frac{f_s^2}{n}\epsilon}{1+\epsilon} \tag{4.76}$$

where we introduced

$$\epsilon = \frac{\delta}{\alpha}\frac{f_s}{f_s+n_p} = \frac{d_{f_s} R_b}{d_{f_s}\left(R_c + R_s\right)} \tag{4.77}$$

From this we see that above threshold, where $n_p \gg f_s$, we have $\epsilon \approx 0$, so that $f_{3dB} = \frac{1}{2\pi}\frac{2\kappa}{\hbar}$. Below threshold $\epsilon \approx \frac{\delta}{\alpha}$ and therefore $f_{3dB} = \frac{1}{2\pi}\frac{\alpha\delta}{\alpha+\delta}N_{QD}\frac{f_s^2}{n_p}$, so that f_{3dB} first increase and then decreases as n_p becomes comparable to f_s^2. For $n_p \gg 1$, the bandwidth returns to the above threshold expression.

Using the analytical results developed above, we can understand the features seen in the modulation bandwidth. Apparently, the above threshold bandwidth is always limited by the cavity lifetime and can only be affected by changing the Q-factor of the system, while below threshold the bandwidth is controlled by the background emission and can exceed the above threshold value for devices with low β-factors and large F. It would seem like the highest modulation bandwidth is found below threshold, but because the effective Purcell factor is reduced for high Q (as discussed in section 3.4), large cavity quality factors are not essential for large F_{eff}. The lasing modulation bandwidth can then be maximized by lowering the Q-factor as much as possible without having the cavity loss become so large that the device cannot lase.

5. OPTICAL PROPERTIES

In this chapter, the optical properties of nanocavities are studied. We use the Finite-Difference Time-Domain (FDTD) method, which is outlined in section 5.1, for setting up and simulating relevant structures. In section 5.2, the modes a modified L3 photonic crystal cavity is extracted from 2D simulations and compared to structures fabricated at DTU Fotonik by PostDoc. Søren Stobbe. Single defect H1 cavities are examined in section 5.3, both as isolated cavities and in coupled two-cavity systems. In section 5.4, we outline a method for calculating farfield patterns based on FDTD simulations and we end the chapter by analyzing the farfield patterns of the isolated and coupled H1 systems discussed in section 5.3.

5.1 The Finite-Difference Time-Domain Method

The importance of knowing the electromagnetic field on a small scale have become more and more pronounced in recent years. With the advent of nano-optical devices, where the structures are on a length scale comparable to the light wavelength, comes a necessity to know details about the electromagnetic field. In cavity quantum electro dynamics it is crucial for understanding to know if the quantum dot is placed at a node or antinode of the optical mode and knowledge about the distribution of k-vectors inside a photonic crystal membrane is important for design of high-Q cavities. At such small length scales, the normal wave optics methods breaks down and it is necessary to solve Maxwell's equations directly. Here, the finite difference method becomes a useful approach.

We start from the full set of Maxwell's equations given by [76]

$$\frac{d\boldsymbol{\mathcal{D}}(\boldsymbol{r},t)}{dt} = \boldsymbol{\nabla} \times \boldsymbol{\mathcal{H}}(\boldsymbol{r},t) - \boldsymbol{j}(\boldsymbol{r},t) \tag{5.1}$$

$$\frac{d\boldsymbol{\mathcal{B}}(\boldsymbol{r},t)}{dt} = -\boldsymbol{\nabla} \times \boldsymbol{\mathcal{E}}(\boldsymbol{r},t) \tag{5.2}$$

$$\boldsymbol{\nabla} \cdot \boldsymbol{\mathcal{D}}(\boldsymbol{r},t) = \rho(\boldsymbol{r},t) \tag{5.3}$$

$$\boldsymbol{\nabla} \cdot \boldsymbol{\mathcal{B}}(\boldsymbol{r},t) = 0 \tag{5.4}$$

where $\boldsymbol{\mathcal{E}}$ and $\boldsymbol{\mathcal{H}}$ are the electric and magnetic fields, $\boldsymbol{\mathcal{D}}$ and $\boldsymbol{\mathcal{B}}$ are the electric displacement and the magnetic induction fields. $\boldsymbol{j}$ is the electric current density

and ρ is the charge density. The constitutive equations are

$$\mathfrak{D}(\boldsymbol{r},t) = \varepsilon(\boldsymbol{r},t)\,\mathfrak{E}(\boldsymbol{r},t) \tag{5.5}$$
$$\mathfrak{B}(\boldsymbol{r},t) = \mu(\boldsymbol{r},t)\,\mathfrak{H}(\boldsymbol{r},t) \tag{5.6}$$

where ε and μ are the dielectric permittivity and magnetic permeability, respectively. In finite difference methods, the time and space variables are discretized as (following ref. [77])

$$z_i = z_0 + i\delta z \tag{5.7}$$
$$t_n = t_0 + n\delta t \tag{5.8}$$

so that the differential equations are replaced by difference equations. For a 1D uniform, static and lossless medium this reduces to

$$\left.\frac{d\mathcal{E}_x(z,t)}{dt}\right|_{z_i}^{t_n} \approx \frac{\mathcal{E}_x(z_i,t_n+\delta t)-\mathcal{E}_x(z_i,t_n-\delta t)}{2\delta t} = \frac{\mathcal{E}_i^{n+1}-\mathcal{E}_i^{n-1}}{2\delta t} \tag{5.9}$$
$$\left.\frac{d\mathcal{H}_y(z,t)}{dz}\right|_{z_i}^{t_n} \approx \frac{\mathcal{H}_y(z_i+\delta z,t_n)-\mathcal{H}_y(z_i-\delta z,t_n)}{2\delta z} = \frac{\mathcal{H}_{i+1}^{n}-\mathcal{H}_{i-1}^{n}}{2\delta z} \tag{5.10}$$

and Maxwell's equations (eqns. (5.1) and (5.2)) then take the form (ignoring $\boldsymbol{j}$)

$$\frac{\mathcal{E}_i^{n+1}-\mathcal{E}_i^{n-1}}{2\delta t} = \frac{1}{\varepsilon}\frac{\mathcal{H}_{i+1}^{n}-\mathcal{H}_{i-1}^{n}}{2\delta z} \tag{5.11}$$
$$\frac{\mathcal{H}_i^{n+1}-\mathcal{H}_i^{n-1}}{2\delta t} = -\frac{1}{\mu}\frac{\mathcal{E}_{i+1}^{n}-\mathcal{E}_{i-1}^{n}}{2\delta z} \tag{5.12}$$

Because the time derivative of the electric field only depends on the magnetic quantities and the time derivative of the magnetic field only depends on electric quantities, we can update the $\mathcal{E}$ and $\mathcal{H}$ fields independently. This is an advantages as the fields can be stored on separate grids that are displaced by half a step. The effective step-length is then shorter which reduces the error without evaluating more points. In such a staggered grid (or Yee lattice), the late time quantities are expressed in terms of the (known) earlier time steps, i.e.

$$\mathcal{E}_i^{n+\frac{1}{2}} = \mathcal{E}_i^{n-\frac{1}{2}} - \frac{\delta t}{\delta z}\frac{1}{\varepsilon}\left(\mathcal{H}_{i+\frac{1}{2}}^{n} - \mathcal{H}_{i-\frac{1}{2}}^{n}\right) \tag{5.13}$$
$$\mathcal{H}_{i+\frac{1}{2}}^{n+1} = \mathcal{H}_{i+\frac{1}{2}}^{n} - \frac{\delta t}{\delta z}\frac{1}{\mu}\left(\mathcal{E}_{i+1}^{n+1} - \mathcal{E}_i^{n+1}\right) \tag{5.14}$$

Thus, if we know the $\mathcal{H}$ field, we can advance the $\mathcal{E}$ field half a time step and then use the new $\mathcal{E}$ field to advance the $\mathcal{H}$ field half a time step. This leapfrog updating scheme is at the heart of FDTD modeling.

As the time variable is updated by the spatial field variable, both variables are connected to the same resolution. The step size for the variables are connected via the Courant factor, S_C

$$\delta t = S_C \delta z \tag{5.15}$$

The Courant factor is a stability factor that is chosen depending on the dimensionality of the problem. A Courant factor of $\frac{1}{2}$ is sufficient for most 1D, 2D and 3D structures.

In the following we will use the software, `MEEP` [78, 79], which is a freely available implementation of the FDTD method. It was developed by Stephen Johnson at Massachusetts Institute of Technology and it can handle calculations of structures in 1D, 2D, 3D and cylindrical coordinates.

A typical calculation in `MEEP` consists of the following steps:
1) Setting up the computational cell, including dimensions and spatial resolution.
2) Defining the dielectric function that describes the structure under consideration. This involves writing a function that returns the dielectric constant at each space point.
3) Setting up sources. Sources in `MEEP` consists of a temporal and spatial part and an amplitude function. The temporal part defines the type of source (continuous wave, gaussian pulse, etc.), the spatial part defines the volume of excitation and the amplitude function allows for exact shaping of the source. All three components are customizable by the user.
4) Defining symmetries and boundary conditions. Often Perfectly Matched Layers (PML) are used as boundary conditions when infinitely large structures are considered. The PML constructs a special type of non-reflecting material that mimics the continuation of the medium to infinity.

`MEEP` implements methods for reducing the computational cell through symmetry operations. If both the dielectric structure and the sources have some (even or odd) symmetry about a symmetry axis, so will the calculated fields. The calculation domain can then be reduced to the smallest asymmetric cell.

`MEEP` has two interfaces: Scheme, which is a programming language developed at Massachusetts Institute of Technology and C++, in which `MEEP` is originally written. While the Scheme interface is better documented, it also limits the structures to combinations of basic shapes (planes, boxes, cylinders, etc.). Not all structures can easily be constructed using these basic shapes and furthermore, data extraction for certain types of simulations have proven difficult. The C++ interface on the other hand, offers more flexibility and direct access to the underlying code, but is not documented to the same extend as the Scheme interface. Often it is necessary to explore the `MEEP` source code to find syntax for relevant functions. In the following, we use the C++ interface, because farfield calculations require access to the fields during the simulations. In appendix B, we include a practical guide for setting up `MEEP` calculations using the C++ interface, which can be used as reference for later studies.

5.2 Modes of a Modified Noda Cavity

For a first calculation, consider the structure shown in figure 5.1. The struc-

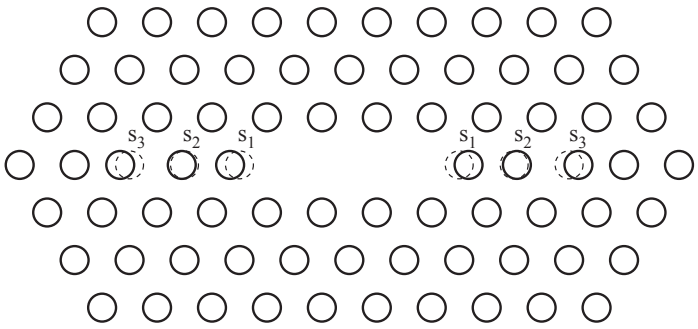

Fig. 5.1: The dielectric structure of a modified Noda type cavity. The three innermost on-axis holes are shifted by $s_1 = 0.175a$, $s_2 = 0.025a$ and $s_3 = 0.175a$. *Parameters in table E.9.*

ture is based on the well-known Noda cavity [51], where the cavity is formed by removing three on-axis holes in a hexagonal lattice. The innermost hole is shifted slightly away from the cavity in order to fulfill the principle of gentle confinement discussed in ref. [51]. The slight perturbation of the hole position helps to move the in-plane k-vectors outside the light cone, which reduces the out-of-plane loss. Q factors exceeding 45000 can be achieved in this type of structures. In the modified structure in figure 5.1, which was fabricated at DTU Fotonik by PostDoc. Søren Stobbe, is similar to the Noda cavity except that the positions of the three innermost on-axis holes are perturbed.

A number of parameters are important for calculation length and precision, including: Number of layers of holes around the cavity, N_{holes}, resolution, R, time after sources, T_{as}, and PML-layer thickness, d_{PML}. Based on an educated guess, we start from a set of standard parameters and vary the parameters one at the time in order to study the change in the calculated mode frequencies. The initial parameter set is: $R = 20$ points per lattice constant, $N_{holes} = 6$, $d_{PML} = 1$ and $T_{as} = 100$ optical cycles. For excitation, we use several dipole emitters at different frequencies and at different locations (away from high symmetry points). The same set of emitters is used in all simulations. In each convergence test, several resonances were found and the relevant parameter was varied until the number and position of the resonances were constant. Figure 5.2 summarizes the convergence tests.

The T_{as} parameter indicates how many `MEEP` time steps the calculation will continue after the excitation dipoles have been turned off. Although, T_{as} is not a structure parameter, it is important for the subsequent extraction of the resonances. For this test, a very long calculation was performed and the modes where extracted using an increasingly larger part of the data. Figure 5.2a shows how the frequencies of the modes found in this way change with T_{as}. Surprisingly, the modes do not converged until at least 6000 optical cycles are used, which is fairly long compared to the initial guess. Possibly, the very

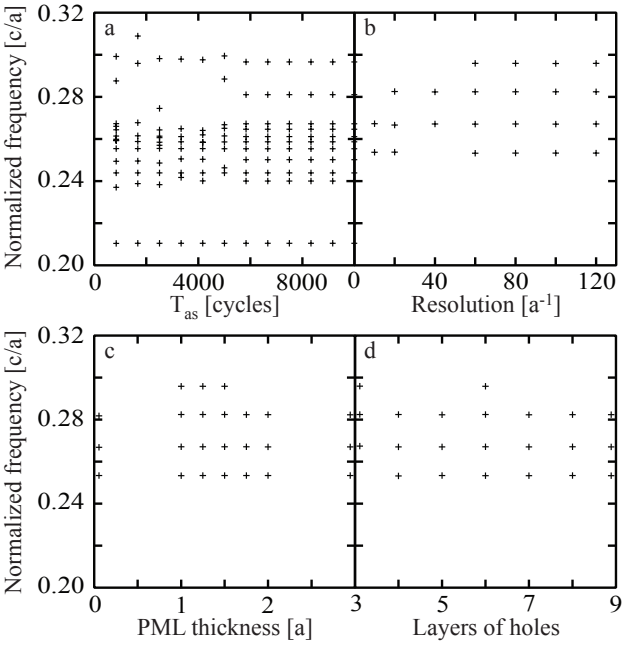

Fig. 5.2: Convergence tests for the modified Noda cavity for a) the time after the sources have died out, T_{as} b) resolution, R c) PML thickness, d_{PML} and d) the number of hole layers surrounding the cavity, N_{holes}.

long T_{as} is only necessary when using broad excitations and a lower T_{as} may acceptable when focusing on only a single mode. For the present calculations, the initial guess of a T_{as} of 100 optical cycles was too low and resulted in unconverged Q-factors. The converged value of 6000 optical cycles was therefore chosen instead.

The resolution is an important factor for the computational resources and runtime, especially for 3D calculations where the number of grid points increases with the resolution to the power of 3. Figure 5.2b shows the convergence of the mode frequencies with the resolution. It seems that a value of $R = 60$ is needed for the frequencies to converge, which is very high even for 2D calculations.

The PML surrounding the computational cell is used as a non-reflecting layer that mimics the behavior of an infinitely large computational cell. A too thin PML layer will give unwanted reflections that will affect the results. As figure 5.2c shows, a PML thickness of 1.8 is sufficient for the present system.

The number of holes surrounding the cavity defect scales the size of the computational cell and is important for the in-plane confinement of the optical mode. Too few holes will degrade the calculated Q-factors and too many makes the computational cell unnecessarily large. Figure 5.2d shows the convergence of

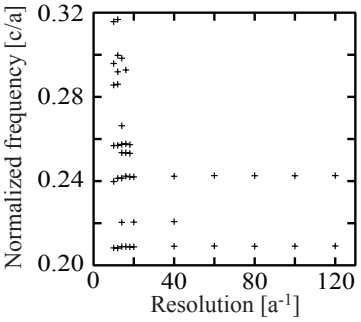

Fig. 5.3: Convergence test for the modified Noda cavity for the resolution with sub-pixel averaging turned on.

the frequencies with number of hole layers. The lowest allowed number of holes is three as the three nearest on-axis holes are shifted in the modified L3 structure. A minimum of 7 layers of holes seems to produce converged results.

The very high converged value of the resolution is problematic for large 2D calculations and for any 3D calculations. Fortunately, `MEEP` implements a method for sub-pixel averaging of the dielectric function, which gives higher precision at lower resolution [80]. Small details in the dielectric function, which affect the modes, require high resolution to be resolved. Sub-pixel averaging calculates a weighted mean of the dielectric function at the critical positions, so that correct results are obtained even if the resolution is too low to resolve all details. Figure 5.3 shows an additional convergence test of the required resolution where sub-pixel averaging is turned on. The effect on the convergence of the frequencies is quite remarkable. Using sub-pixel averaging reduces the necessary resolution to a tractable 20 points per lattice constant.

Following the conclusions of the calculations above, the set of converged parameters in table E.9 were used for the following calculations. The modes are mapped by placing spectrally broad excitation dipoles at positions away from symmetry points and recording the components of the electrical field. We expect modes in $\mathcal{E}_x$ and $\mathcal{E}_y$ and sweep both components to get all the modes. Figure 5.4 compares the modes found by the FDTD simulations to experimentally determined mode positions.

The simulations using broad excitation dipoles predict 6 distinct high-Q modes positioned from $0.20 - 0.25$ c/a and a number of low-Q modes above 0.25 c/a. The position and Q-factors of the high-Q modes were confirmed by a series of simulations using narrow excitation dipoles. Comparing to the experimentally obtained mode positions ($\diamond$), we note that although the number and relative spacing of the FDTD modes agree with the experimental modes, there is a general shift of the modes. The shift is most likely due to the fact that the simulations were performed in 2D and thus did not include details about the PhC

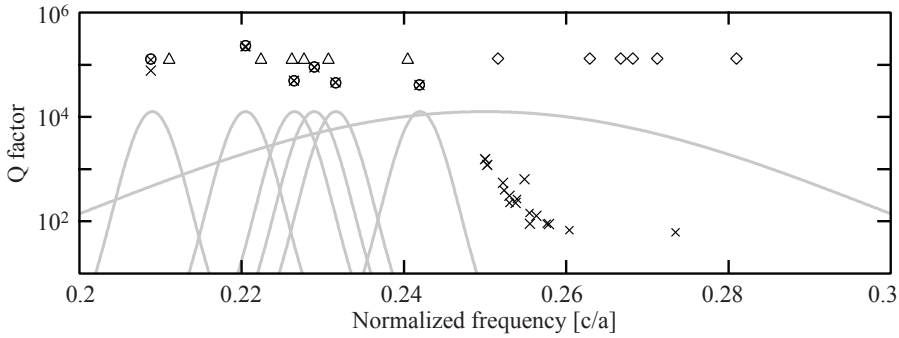

Fig. 5.4: 2D calculation of the modes of the modified Noda cavity. Modes found by the broad (×) and narrow (○) $\mathcal{E}_x$ and $\mathcal{E}_y$ dipoles are shown together with the experimentally measured mode positions (◇). Experimental Q-factors not plotted. The △ denotes the experimental modes, which have been shifted to compensate for the 2D calculation. The spectral positions and widths of the broad and narrow excitation dipoles are shown. *Parameters in table E.9. Experimental data by Serkan Ates.*

membrane thickness. Moving the experimental modes to the $0.20 - 0.25$ c/a range to compensate for the 2D calculation (△), we see that the relative positions match reasonably well. The discrepancies are attributed to fabrication imperfections and uncertainties in the measurements and to the 2D calculations. We see from these calculations that `MEEP` produces results that are close to what is expected from experimental measurements. The $\mathcal{E}_x$ and $\mathcal{E}_y$ field components of the mode profiles of the 6 modes found by FDTD simulations are shown in figures C.1 and C.2 in appendix C.

5.3 Coupled Modes of Single Defect Cavities

In order to study the optical properties of coupled nanocavities, we begin by simulating the modes of a single isolated H1 cavity. Once familiar with the isolated system, we construct coupled systems of two cavities and investigate the behavior of the modes. These types of coupled structures were fabricated by Ph.D. student Martin Schubert at DTU Fotonik and the experimental data in this section is also measured by him.

The isolated single cavity structure consists of a freestanding GaAs PhC membrane with a single hole missing in the otherwise regular rectangular hole lattice (H1 cavity, see figure 5.5a). Structure parameters were extracted from SEM images of the fabricated structures. For the investigated structures, the lattice constant was measured to $a = 280$ nm, the membrane thickness was $d = 0.59a$ and the hole radius was $r = 0.38a$. A refractive index of $n = 3.5$ appropriate for GaAs structures were used and values for other parameters was determined from convergence tests. Full set of converged parameters is shown in table E.10 in appendix E.

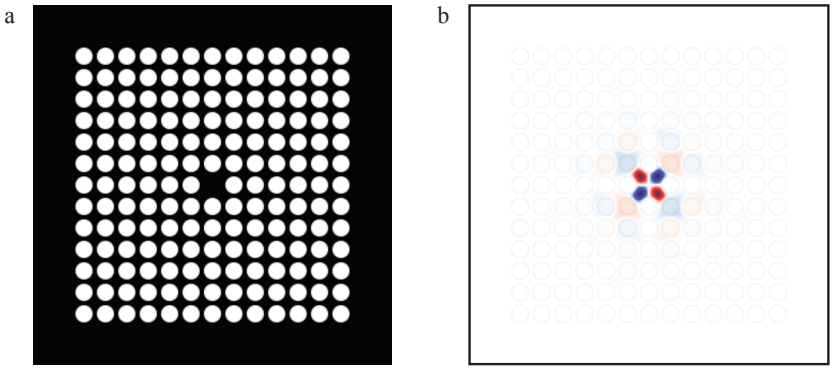

Fig. 5.5: a) The structure of the quadratic lattice H1 cavity and b) the $\mathcal{H}_z$ component of the quadrupole mode. *Parameters in table E.10.*

Based on these information, 3D FDTD simulations of the single cavity structure in figure 5.5a were performed. A number of modes were identified including degenerate dipole modes in the x- and y-directions and monopole modes. We focus on the quadrupole mode found at 0.3111 c/a with a Q-factor of more than 25000. The mode profile is shown in figure 5.5b and is seen to have a structure consisting of four main lobes, where each lobe is π out of phase with its neighboring lobes. Thus, along the lines $x = 0$ and $y = 0$ the field amplitude is always zero. The mode is well confined inside the defect and the evanescent tails reach only a few lattice periods into the surrounding PhC.

The symmetries of the rectangular PhC lattice leads to two natural configurations of two coupled cavities. Either coupling along the x-axis (or y-axis) or along the diagonal (xy-direction). In terms of the symmetry points of the lattice (c.f. figure 2.7), the on-axis coupling configuration is designated the ΓX-direction and the diagonal is the ΓM-direction. Both directions are interesting. In the ΓX-direction, the cavities are closer together than in the ΓM-direction for the same number of holes separating the cavities (N_{sep}), but due to the four-lobe structure of the quadrupole mode, we expect the evanescent mode tails to be stronger in the ΓM-direction. Calculations of the modes in a two cavity system, where the cavities are separated by 2 holes are shown in figure 5.6.

For the two coupled cavities, the quadrupole mode splits up into an in-phase mode and out-of-phase mode, which is a well-known behavior for coupled modes. We call the modes with similar lobe structure inside the defect regions for "in-phase" (figure 5.6 top) and the other for "out-of-phase" (figure 5.6 bottom). The two modes have different resonance frequencies, which are split symmetrically around the frequency found for the isolated single cavity. The splitting is proportional to the coupling strength and thus decreases with increasing intercavity distance. This can be seen from figure 5.7, where the

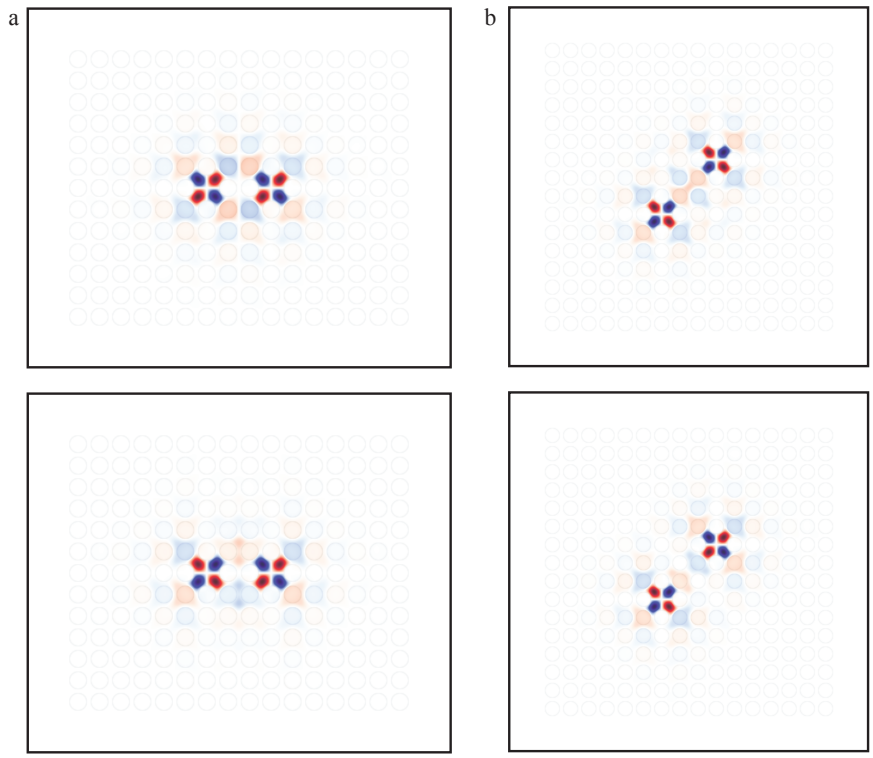

Fig. 5.6: The in-phase and out-of-phase configurations of the quadrupole mode for two coupled cavities in the a) ΓX-direction and b) ΓM-direction. *Parameters in table E.10.*

resonance frequencies are plotted for calculations with varying intercavity distance.

The frequencies converge on the single cavity frequency for increasing intercavity distance, which is to be expected as two cavities infinitely removed from each other will essentially behave as isolated cavities, reproducing the single cavity results. Interestingly, the frequencies of the in-phase and out-of-phase modes for the ΓX-direction alternate between being positively and negatively detuned from the single cavity frequency. The resonance frequencies for the ΓM-direction do not show the same behavior and always have the in-phase mode as the high energy mode.

To understand this behavior, we need to study the field distribution of the coupled modes (figure 5.6). Each mode seems primarily to be concentrated in the low-index holes of the PhC material, which is the natural behavior for a mode, that tries to minimize its energy [43]. Thus, the mode "jumps" from hole to hole (though never diagonally) changing the phase by π for each jump.

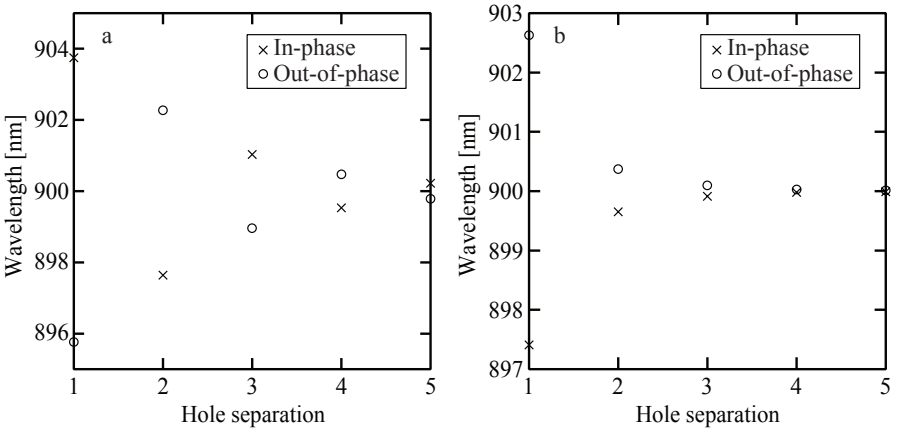

Fig. 5.7: Resonance frequencies for two cavity systems with the intercavity distance varied from 1 to 5 holes for a) the ΓX-direction and b) the ΓM-direction. In-phase modes are marked by × and out-of-phase modes by ○. *Parameters in table E.10.*

In the ΓX case, with one hole separating the two cavities, the modes of the two cavities will destructively interfere in the intermediate hole if the modes are in-phase. If the modes are out-of-phase, the result is constructive interference, which increases the energy of the total field and gives the out-of-phase mode the highest energy. For two hole separation, the in-phase mode gives constructive interference in the separating holes (and thus the highest energy) and vice versa for the out-of-phase mode (c.f. figure 5.6a). In this way, the behavior in figure 5.7a can be understood.

To understand why the same behavior is not seen in figure 5.7b, we study the mode profiles in figure 5.6b for the ΓM case. We see that the shortest route connecting two cavities in the ΓM-direction always involve an even number of holes (assuming that the mode does not jump diagonally). Thus, it is always the in-phase mode that is associated with constructive interference and therefore have the highest energy.

With this new understanding of the coupled mode behavior, the designations "in-phase" and "out-of-phase" may seem a bit illogical. A more consistent definition would be to always designate the high energy mode as "in-phase" and the low energy mode as "out-of-phase". However, because of the non-trivial frequency splitting behavior (figure 5.7) makes this definition difficult to work with, we stick with our original definition.

Comparison to experimentally measured mode splittings gives a good qualitative agreement (not shown).

5.4 Farfield Calculations

The farfield patterns for the simulated structures can, in principle, be calculated by FDTD methods by expanding the computational cell, so that the radiation zone is included. However, this method requires many computational resources and is rather inefficient. Instead, we use a transformation, that allow us to express the farfield radiation pattern in terms of the fields directly above the structure [53, 81–83].

Consider a plane parallel to the PhC membrane located outside the tails of the evanescent tails of the mode (see figure 5.8). The electromagnetic field at this plane can be converted into equivalent electric and magnetic surface currents as [82]

$$\boldsymbol{J}_s = \boldsymbol{n} \times \boldsymbol{\mathcal{H}} = -\mathcal{H}_y \hat{\boldsymbol{x}} + \mathcal{H}_x \hat{\boldsymbol{y}} \tag{5.16}$$

$$\boldsymbol{M}_s = -\boldsymbol{n} \times \boldsymbol{\mathcal{E}} = \mathcal{E}_y \hat{\boldsymbol{x}} - \mathcal{E}_x \hat{\boldsymbol{y}} \tag{5.17}$$

where $\boldsymbol{n}$ is the surface normal and $\hat{\boldsymbol{x}}$ and $\hat{\boldsymbol{y}}$ are unit vectors in the x- and y-directions. The farfield can then be calculated in terms of the potentials $\boldsymbol{A}$ and $\boldsymbol{F}$ as [81]

$$\boldsymbol{\mathcal{E}}_{FF} = -i\omega \boldsymbol{A} - \frac{i\omega}{k^2} \boldsymbol{\nabla} (\boldsymbol{\nabla} \cdot \boldsymbol{A}) - \frac{1}{\varepsilon_0} \boldsymbol{\nabla} \times \boldsymbol{F} \tag{5.18}$$

$$\boldsymbol{\mathcal{H}}_{FF} = -i\omega \boldsymbol{F} - \frac{i\omega}{k^2} \boldsymbol{\nabla} (\boldsymbol{\nabla} \cdot \boldsymbol{F}) - \frac{1}{\varepsilon_0} \boldsymbol{\nabla} \times \boldsymbol{A} \tag{5.19}$$

The vector potentials are given by

$$\boldsymbol{A} = \frac{\mu_0}{4\pi} \int_{\mathcal{S}} \boldsymbol{J}_s \frac{e^{-ikr}}{r} dS \tag{5.20}$$

$$\boldsymbol{F} = \frac{\varepsilon_0}{4\pi} \int_{\mathcal{S}} \boldsymbol{M}_s \frac{e^{-ikr}}{r} dS \tag{5.21}$$

where $k = \frac{\omega}{c}$ is the free-space wave-vector and r is the distance from a given point, $\mathcal{P}$, on the surface $\mathcal{S}$ to the observation point, $\mathcal{O}$, in the farfield (see figure 5.8). From the figure, it is clear that $\boldsymbol{r} = \boldsymbol{R} - \boldsymbol{r'}$, so that we can write (for $r' \ll R$)

$$\begin{aligned} r &\approx \sqrt{R^2 - 2Rr' \cos(\varphi)} = R\sqrt{1 - 2\frac{r'}{R} \cos(\varphi)} \\ &\approx R - r' \cos(\varphi) \end{aligned} \tag{5.22}$$

where φ is the angle between vectors $\boldsymbol{R}$ and $\boldsymbol{r'}$. Using eqn. (5.22), we can write eqns. (5.20) and (5.21) as

$$\boldsymbol{A} \approx \mu_0 \frac{e^{-ikR}}{4\pi R} \boldsymbol{N} \tag{5.23}$$

$$\boldsymbol{F} \approx \varepsilon_0 \frac{e^{-ikR}}{4\pi R} \boldsymbol{L} \tag{5.24}$$

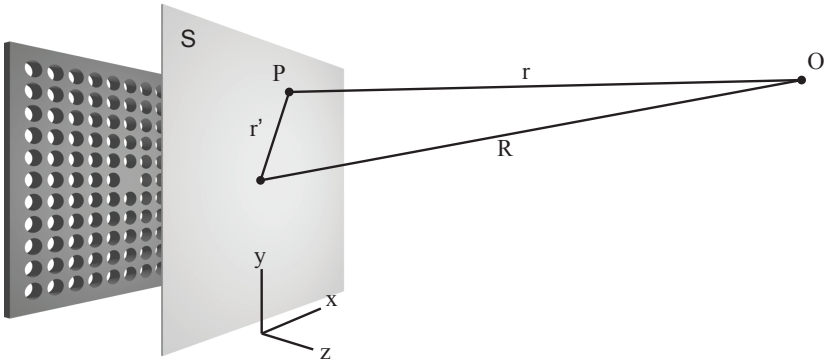

Fig. 5.8: The plane $\mathcal{S}$ located outside the evanescent tails of the PhC mode parallel to the membrane. The vector to a given point, $\mathcal{P}$, on the plane is denoted $\boldsymbol{r'}$, the vector to the observation point, $\mathcal{O}$, in the farfield is denoted, $\boldsymbol{R}$ and the vector connecting the points $\mathcal{P}$ and $\mathcal{O}$ is denoted $\boldsymbol{r}$.

where

$$\boldsymbol{N} = \int_{\mathcal{S}} \boldsymbol{J}_s e^{-ikr'\cos(\varphi)} dS \tag{5.25}$$

$$\boldsymbol{L} = \int_{\mathcal{S}} \boldsymbol{M}_s e^{-ikr'\cos(\varphi)} dS \tag{5.26}$$

and where we neglected $r'\cos(\varphi)$ in the denominators of eqns. (5.23)-(5.24). Using the dot product of vectors $\boldsymbol{R} = (x, y, z)$ and $\boldsymbol{r'} = (x', y', 0)$, i.e. $\boldsymbol{R} \cdot \boldsymbol{r'} = Rr'\cos(\varphi) = xx' + yy'$, we can write eqns. (5.25) and (5.26) as

$$\boldsymbol{N} = \int_{\mathcal{S}} \boldsymbol{J}_s e^{-i\boldsymbol{k}_\parallel \cdot \boldsymbol{r'}} dS \tag{5.27}$$

$$\boldsymbol{L} = \int_{\mathcal{S}} \boldsymbol{M}_s e^{-i\boldsymbol{k}_\parallel \cdot \boldsymbol{r'}} dS \tag{5.28}$$

where $\boldsymbol{k}_\parallel = k\left(\frac{x}{R}\hat{\boldsymbol{x}} + \frac{y}{R}\hat{\boldsymbol{y}}\right)$. Thus, we have reduced $\boldsymbol{N}$ and $\boldsymbol{L}$ to 2D fourier transformations evaluated at the k-vector $\boldsymbol{k}_\parallel$. Note that as the length of $\boldsymbol{k}_\parallel$ cannot exceed k, only k-vectors lying within the light cone contributes to the farfield [82]. Inserting eqns. (5.16) and (5.17) into eqns. (5.27) and (5.28), we can express the fourier components in terms of the field components at the surface $\mathcal{S}$

$$N_x = -\mathcal{F}\{H_y\}|_{k=k_\parallel} \tag{5.29}$$

$$N_y = \mathcal{F}\{H_x\}|_{k=k_\parallel} \tag{5.30}$$

$$L_x = \mathcal{F}\{E_y\}|_{k=k_\parallel} \tag{5.31}$$

$$L_y = -\mathcal{F}\{E_x\}|_{k=k_\parallel} \tag{5.32}$$

Inserting the potentials $\boldsymbol{A}$ and $\boldsymbol{F}$ in eqns. (5.18) and (5.19) and neglecting all terms decaying faster than $\frac{1}{R}$, we find (in spherical coordinates)

$$\mathcal{E}_\theta = \quad \eta\mathcal{H}_\phi = -i\frac{e^{-ikR}}{2\lambda R}\left[\eta N_\theta + L_\phi\right] \tag{5.33}$$

$$\mathcal{E}_\phi = -\eta\mathcal{H}_\theta = -i\frac{e^{-ikR}}{2\lambda R}\left[\eta N_\phi - L_\theta\right] \tag{5.34}$$

where $\eta = \sqrt{\frac{\mu_0}{\varepsilon_0}}$ and λ is the wavelength. Following the above results, it is only necessary to record the x- and y-components of the $\mathcal{E}$ and $\mathcal{H}$ fields at a surface above the PhC structure and then transform according to eqns. (5.29)-(5.34). Note, however, that the surface $\mathcal{S}$ must lie outside the tails of the evanescent field from the membrane. If not, components of the field, that normally die out exponentially, will be translated to the farfield zone and give an erroneous emission pattern.

Most often, we are interested in the spectral fourier transform of the emitted fields. This can be obtained by recording the time evolution of the fields and Fourier transform after the simulation is done. In actual calculations, it turns out to be impractical to record the field in every time step for large calculations. Instead, the Fourier transform is calculated during the simulation, where the discrete Fourier transformation can be summed up progressively as [53]

$$\mathcal{F}\{\mathcal{E}\} = \mathcal{F}\{\mathcal{E}\}|_i^{n-1} + \mathcal{E}|_i^n \, e^{i\omega_c t_n} \tag{5.35}$$

$$\mathcal{F}\{\mathcal{H}\} = \mathcal{F}\{\mathcal{E}\}|_i^{n-1} + \mathcal{H}|_i^n \, e^{i\omega_c t_n} \tag{5.36}$$

which sums to the fourier transform at the cavity frequency, ω_c. Of course, the full spectrum can be obtained by calculating the Fourier sum at more frequencies, however, for high-Q cavities, the emission spectrum is sharply peaked and so, for our purposes, it is sufficient to evaluate the Fourier transform only at ω_c.

As a test of the method, we calculate the farfield from the grating structure shown in figure 5.9a. This is basically Young's double slit experiment [84] and it has a well-known farfield pattern consisting of discrete points set apart by an angle calculated as

$$\sin(\theta_m) = m\frac{\lambda}{d} \tag{5.37}$$

where d is the grating period and m is the order of the maximum. In the simulation, the grating period was chosen to be $2a$ and the structure was illuminated from below using a continuous wave plane source with frequency $2\ c/a$. Thus, according to eqn. (5.37), there should be five maxima appearing at angles $\theta_0 = 0°$, $\theta_1 = 14.5°$, $\theta_2 = 30.0°$, $\theta_3 = 36.9°$ and $\theta_4 = 90°$. In figure 5.9b, we show the calculate farfield (electrical component) in spherical coordinates. The center of the plot corresponds to a polar angle of zero ($\theta = 0$) and the azimuthal angle varies along the circumference of the plot. In the figure, we see three points, which fits exactly with θ_0 and θ_1. Plotting the farfield on

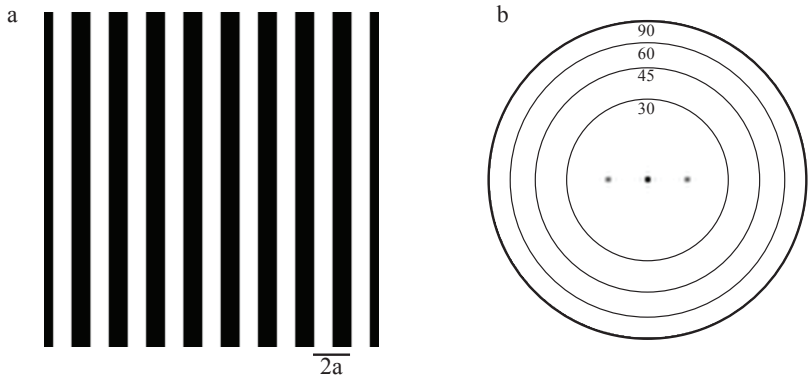

Fig. 5.9: a) The structure and b) calculated $\mathcal{E}$ farfield for a grating.

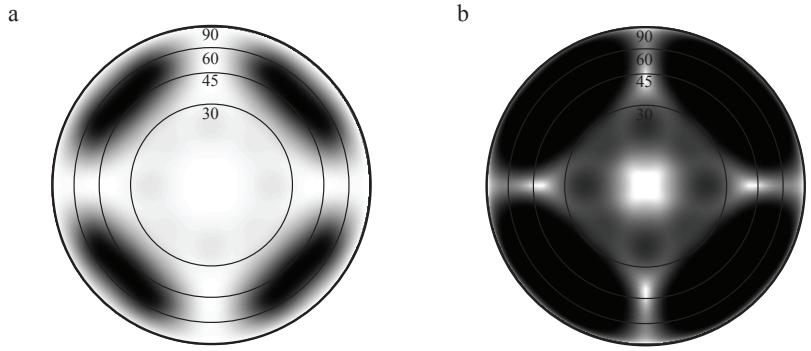

Fig. 5.10: Calculated farfield of an isolated H1 cavity on a) a linear scale b) logarithmic scale. Black color indicates high intensity.

a logarithmic scale, the following three points also becomes visible and they coincide precisely with the predicted angles as well (not shown).

With this indication that the farfield method is working, we move on to the H1 cavities discussed in section 5.3. We begin by calculating the farfield for the quadrupole in the isolated H1 cavity and plot the result in figure 5.10. The farfield seems to concentrate into four lobes between 45° and 60° from vertical with a clear minimum at $\theta = 0$. The fact that the farfield amplitude is zero at $\theta = 0$ is to expected from the symmetric four-lobed mode structure, which destructively interferes vertically above the cavity. Plotting the farfield on a logarithmic scale as is done in figure 5.10b reveals more structure for $\theta < 30°$. The x and y components of the farfield show a similar four-lobed structure and does not exhibit any distinct polarization (not shown).

Moving on to coupled structures, we calculate the farfield patterns for coupling in both the ΓX- and ΓM-direction and for the quadrupole modes in-

and out-of-phase. The intercavity distance, N_{sep}, is varied from 1 to 5 holes and the produced farfields are plotted in figures 5.11 and 5.12. The farfields show complicated patterns, which vary with the intercavity separation. Focusing first on the ΓX-direction in figure 5.11, we see that two distinct types of farfield patterns emerge. The patterns for $N_{sep} = 2$ and $N_{sep} = 4$ show clear stripes with either a maximum or a minimum at $\theta = 0$ for both in- and out-of-phase modes. This is a well-known signature of in-phase and out-of-phase coupled modes, where the farfield patterns with central maxima are associated with in-phase modes and the out-of-phase mode is associated with the central minimum modes [85–87]. The patterns for $N_{sep} = 1$, $N_{sep} = 3$ and $N_{sep} = 5$ are more difficult to explain. The farfield patterns consist of several isolated lobes at angles $> 45°$ and does not conform to the same in- and out-of-phase rules as for the other separations. However, we note that if the farfield patterns for the in- and out-of-phase modes are added together, the farfield pattern of the single isolated H1 cavity (figure 5.10) is roughly recovered.

The farfield patterns for the ΓM-direction display a similar dependence as for the ΓX-direction. Even number hole separations give coupled mode radiation patterns, while the odd numbers in- and out-of-phase patterns can be added to give the single cavity pattern. However, for the ΓM-direction it becomes clear that the patterns also have another dependence on the number of holes separating the cavities. As N_{sep} increases, the patterns are separated by more and more minima, which is correlated to the number of holes separation. As of now, we do not have a clear understanding of the farfield behavior of the odd number hole separations, but we speculate that the strong contribution from the field inside the cavity defects may alternately lead to destructive and constructive interference depending on N_{sep}. Constructive interference would drown out the coupled mode details in the farfield, while destructive interference would promote the relatively weaker coupled mode signature.

The coupled modes ($N_{sep} = 2$ and $N_{sep} = 4$) for the ΓX-direction display a quite pronounced polarization of the $\mathcal{E}_x$-component (see figures C.3 and C.4 in appendix C). The un-coupled modes on the other hand do not display any noteworthy polarization behavior. This supports that the patterns for N_{sep} odd are not strongly coupled. The corresponding farfield patterns for the $\mathcal{E}_{xy}$ and $\mathcal{E}_{x-y}$-polarizations for the ΓM-direction (figure C.5 and C.6) also show a similar behavior.

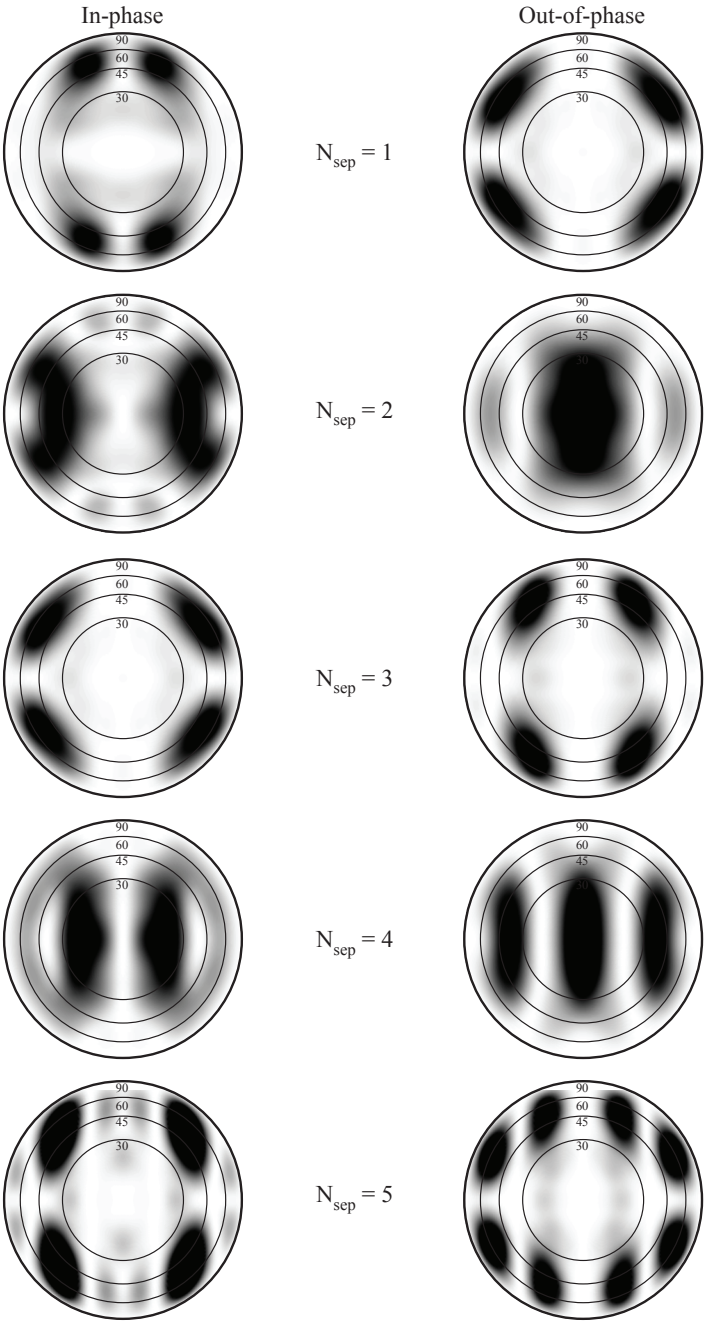

Fig. 5.11: Calculated farfield for two H1 cavities coupled in the ΓX-direction and the quadrupole modes both in- and out-of-phase.

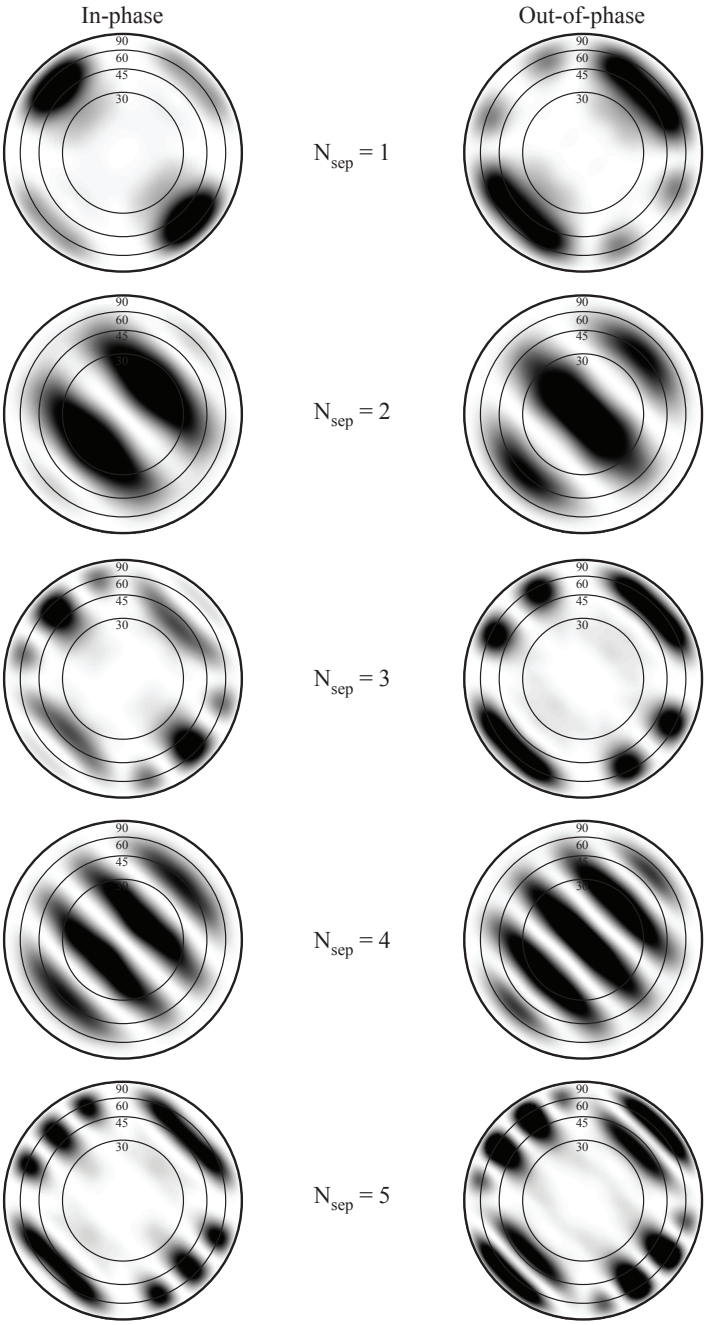

Fig. 5.12: Calculated farfield for two H1 cavities coupled in the ΓM-direction and the quadrupole modes both in- and out-of-phase.

6. COUPLED NANOCAVITY LASERS

In this chapter, the phase-locking properties of coupled nanocavity lasers are studied in a tight-binding formalism. Although placed at the end of the thesis, this was actually some of the first work done and therefore uses the simple expression for the spontaneous recombination rate (eqns. (3.4) and (3.5)), rather than the full model outlined in section 3.6, which was not developed until later. Although the simple model does not capture the bandfilling effect of the spontaneous emission and the stimulated emission is not Purcell enhanced, we believe that the results in this chapter are still valid for two reasons. 1) The coupled system was investigated in the laser regime close to threshold where bandfilling is not a problem as the carrier density clamps and 2) variations in the Purcell enhancement were achieved by changing the mode volume, not the Q-factor, so that Purcell factor used can be interpreted as F_{eff}.

As mentioned in the introduction, nanocavity light emitting devices show promise of higher modulation speed and efficiency, but only have limited use in long range applications due to the low output power of single nanocavity emitters. The output from nanocavities is limited by the inherent fact that the active volume is very small, so that only a small amount of active material can efficiently participate in the operation of the device. This limits the practical use to short-distance communication. For nanocavity devices to be usable for long-haul optical communication, the output power must be significantly improved. A way to improve the output, that have previously been explored for vertical cavity surface emitting lasers [87–90], is to fabricate large arrays of nanocavity lasers that can produce the desired output power levels. While conceptually simple, the nanocavity laser array still contain many unsolved problems. For instance, how to electrically pump several thousand individual devices at the same time remains an open question. The focus of this chapter is a bit different, but equally important. In order to produce stable output from the array, it is necessary to bring the cavities to phase-lock, i.e. to operate at the same frequency and with a fixed phase-difference. Output from arrays that are not phase-locked will be noisy, exhibit destructive interference and beating, which renders it unusable for high-speed communication.

As mentioned in section 4.1, Altug et al. [12] have previously experimentally investigated coupled PhC cavities and found indications of lasing with modulation speeds exceeding 100 GHz and although the reported dynamical results have later been questioned [26], they did show I/O characteristics for coupled devices, which showed the feasibility of this type of devices.

To study the phase-locking properties of coupled laser arrays, we employ a tight-binding formalism. The optical modes in PhC defect cavities are mainly concentrated inside the defect region, but evanescent tails of the mode reach into the PhC and can overlap with other nearby cavities. The mode can then leak into the neighboring cavities. Typically, the overlaps will be small, which is well suited for tight-binding type models. Winful *et al.* studied such a tight-binding LRE model in a series of papers [29, 30, 91–93] and argued for the robustness of the model. Here, we extend this tight-binding LRE model to the nanocavity regime by including Purcell enhancement of the spontaneous emission and by investigating the coupling strength of PhC cavities through FDTD simulations. We present simulations of two coupled PhC lasers and show that regimes where the lasers phase-lock exist, but that they are sensitive to detuning effects such as those arising from fabrication imperfections in the PhC.

Again, we use the LRE in eqns. (3.48) and (3.49) with the rates given by

$$R_{nr} = A_s N + C N^3 \tag{6.1}$$

$$R_c = \beta F_{eff} B N^2 \tag{6.2}$$

$$R_b = (1-\beta)\, B N^2 \tag{6.3}$$

$$R_{st} = P v_g G_0 \ln\left(\frac{N+N_s}{N_{tr}+N_s}\right) \tag{6.4}$$

$$R_p = \frac{P}{\tau_p} \tag{6.5}$$

In this case, the spontaneous emission factor is taken as a constant value. Because we examine phase sensitive interactions, we supply the usual LREs by an equation for the evolution of the phase

$$\dot{\varphi} = \frac{1}{2}\Gamma\alpha\,(G - G_{th}) \tag{6.6}$$

where G_{th} is the threshold gain and α is the linewidth enhancement factor. The equation expresses the fact that the refractive index of the active material changes with the carrier density and therefore also the frequency of the light [31].

We consider two PhC defect cavities, that are in close proximity, so that their electromagnetic fields overlap. The coupling can then for a weakly coupled system be described in a tight-binding model and terms giving the coupling can be derived as outlined in appendix D. Here, we take a shortcut and derive the coupling terms by postulating that the coupling of the electric field in cavities A and B is given as

$$\dot{\mathcal{E}}_A = i\omega_A \mathcal{E}_A + \frac{1}{2} i\kappa\bar{\omega}\mathcal{E}_B \tag{6.7}$$

$$\dot{\mathcal{E}}_B = i\omega_B \mathcal{E}_B + \frac{1}{2} i\kappa\bar{\omega}\mathcal{E}_A \tag{6.8}$$

where $\mathcal{E}_A$ and $\mathcal{E}_B$ are the complex electric fields in cavities A and B with resonance frequencies ω_A and ω_B. κ is the coupling constant and $\bar{\omega} = (\omega_A +$

$\omega_B)/2$. We split eqns. (6.7) and (6.8) into equations for the photon density, P and phase, φ, using $\mathcal{E} = \sqrt{P}\exp(i\omega t + i\varphi)$, so that

$$P = \mathcal{E}\mathcal{E}^* \tag{6.9}$$

$$\varphi = -\omega t - \frac{1}{2} i \ln\left(\frac{\mathcal{E}}{\mathcal{E}^*}\right) \tag{6.10}$$

where $\mathcal{E}^*$ is the complex conjugate of $\mathcal{E}$. Inserting eqns. (6.9) and (6.10) in $\dot{P}$ and $\dot{\varphi}$ yields

$$\dot{P} = \dot{\mathcal{E}}\mathcal{E}^* + \mathcal{E}\dot{\mathcal{E}}^* \tag{6.11}$$

$$\dot{\varphi} = -\omega - \frac{1}{2} i \left[\frac{\dot{\mathcal{E}}}{\mathcal{E}} - \frac{\dot{\mathcal{E}}^*}{\mathcal{E}^*}\right] \tag{6.12}$$

Thus, by inserting eqns. (6.7) and (6.8), the coupling terms for cavities A and B take the form

$$\dot{P}_A = +\kappa\bar{\omega}\,\mathrm{Im}\left\{\mathcal{E}_A\mathcal{E}_B^*\right\} \tag{6.13}$$

$$\dot{P}_B = -\kappa\bar{\omega}\,\mathrm{Im}\left\{\mathcal{E}_A\mathcal{E}_B^*\right\} \tag{6.14}$$

$$\dot{\varphi}_A = \frac{1}{2}\kappa\bar{\omega}\,\mathrm{Re}\left\{\frac{\mathcal{E}_B}{\mathcal{E}_A}\right\} \tag{6.15}$$

$$\dot{\varphi}_B = \frac{1}{2}\kappa\bar{\omega}\,\mathrm{Re}\left\{\frac{\mathcal{E}_A}{\mathcal{E}_B}\right\} \tag{6.16}$$

Using the electric field ($\mathcal{E} = \sqrt{P}\exp(i\omega t + i\varphi)$), we end up with the set of coupling equations

$$\dot{P}_A = +\kappa\bar{\omega}\sqrt{P_A P_B}\sin\left(\delta\omega t + \delta\varphi\right) \tag{6.17}$$

$$\dot{P}_B = -\kappa\bar{\omega}\sqrt{P_A P_B}\sin\left(\delta\omega t + \delta\varphi\right) \tag{6.18}$$

$$\dot{\varphi}_A = \frac{1}{2}\kappa\bar{\omega}\sqrt{\frac{P_B}{P_A}}\cos\left(\delta\omega t + \delta\varphi\right) \tag{6.19}$$

$$\dot{\varphi}_B = \frac{1}{2}\kappa\bar{\omega}\sqrt{\frac{P_A}{P_B}}\cos\left(\delta\omega t + \delta\varphi\right) \tag{6.20}$$

where $\delta\omega = \omega_A - \omega_B$ and $\delta\varphi = \varphi_A - \varphi_B$. The final system of LREs with coupling terms is then

$$\dot{N}_A = J - \left(A_s + CN_A^2\right)N_A - \beta F_{eff} B N_A^2 - (1-\beta)\,BN_A^2 - G_A P_A \tag{6.21}$$

$$\dot{N}_B = J - \left(A_s + CN_B^2\right)N_B - \beta F_{eff} B N_B^2 - (1-\beta)\,BN_B^2 - G_B P_B \tag{6.22}$$

$$\dot{P}_A = \left[\Gamma G_A - \frac{1}{\tau_p}\right]P_A + \Gamma\beta F_{eff} B N_A^2 + \kappa\bar{\omega}\sqrt{P_A P_B}\sin\left(\delta\omega t + \delta\varphi\right) \tag{6.23}$$

$$\dot{P}_B = \left[\Gamma G_B - \frac{1}{\tau_p}\right]P_B + \Gamma\beta F_{eff} B N_B^2 - \kappa\bar{\omega}\sqrt{P_A P_B}\sin\left(\delta\omega t + \delta\varphi\right) \tag{6.24}$$

$$\dot{\delta\varphi} = \frac{1}{2}\Gamma\alpha\left(G_A - G_B\right) + \frac{1}{2}\kappa\bar{\omega}\left[\sqrt{\frac{P_B}{P_A}} - \sqrt{\frac{P_A}{P_B}}\right]\cos\left(\delta\omega t + \delta\varphi\right) \tag{6.25}$$

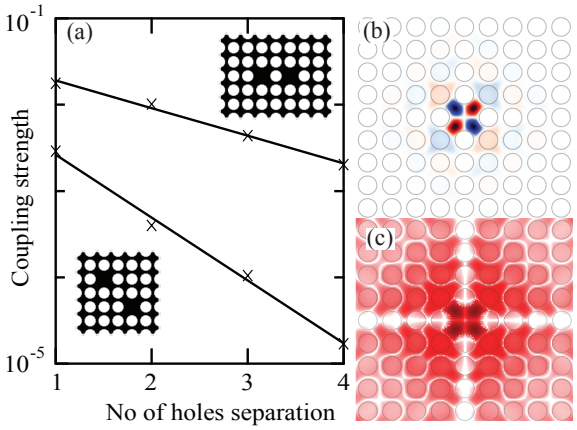

Fig. 6.1: (a) Calculated coupling strength for two cavities with varying intercavity distance in both the ΓX and ΓM-direction. The solid lines are exponential fits. (b) Mode profile for the quadrupole mode. (c) Absolute square of the quadrupole mode.

The coupling strength, κ, is usually defined from an overlap integral between neighboring modes [31, 94]. The dissipative nature of cavity modes, however, renders this approach highly ambiguous since the modes necessarily diverge exponentially at long distances [95], calling for a non-Hermitian reformulation of the coupling equations. This is beyond the scope of the present work, so we take a more direct approach based on time-domain calculations.

In a system of two resonant and passive cavities described by eqns. (6.17) - (6.20), exciting a mode in only one cavity leads to an oscillating field amplitude as energy is exchanged between the cavities. It can be shown that the field amplitude oscillates at a frequency given by $\omega_{TB} = \frac{1}{2}\kappa\bar{\omega}$. In this way the coupling constant can be derived from the time evolution of the field amplitude, which is easily obtained from FDTD simulations. Figure 6.1a displays example calculations of the coupling strengths for varied intercavity spacing in both the ΓX and ΓM-direction for the quadrupole mode in figure 6.1b-c (c.f. figure 5.7). We note an exponential decrease of the coupling strength for both directions, but the decrease is faster for the ΓM-direction corresponding to the cavities being $\sqrt{2}$ further apart. The cavities cannot come closer to each other than 1 hole separation and so the data in figure 6.1a indicate a maximum coupling strength of approximately 10^{-2} for photonic crystals. While there is, in principle, no lower limit for the coupling strength, the coupling terms in real systems must be large enough to overcome the various noise terms.

The differential equations were solved numerically with the initial conditions set to $N_A = N_B = N_{tr}$ and $S_A = S_B = 0.1N_{tr}$. It is clear from eqns. (6.23) - (6.25) that a phase difference of any integer multiple of π will lead to in- and out-of-phase solutions that evolve independently of each other. In practice,

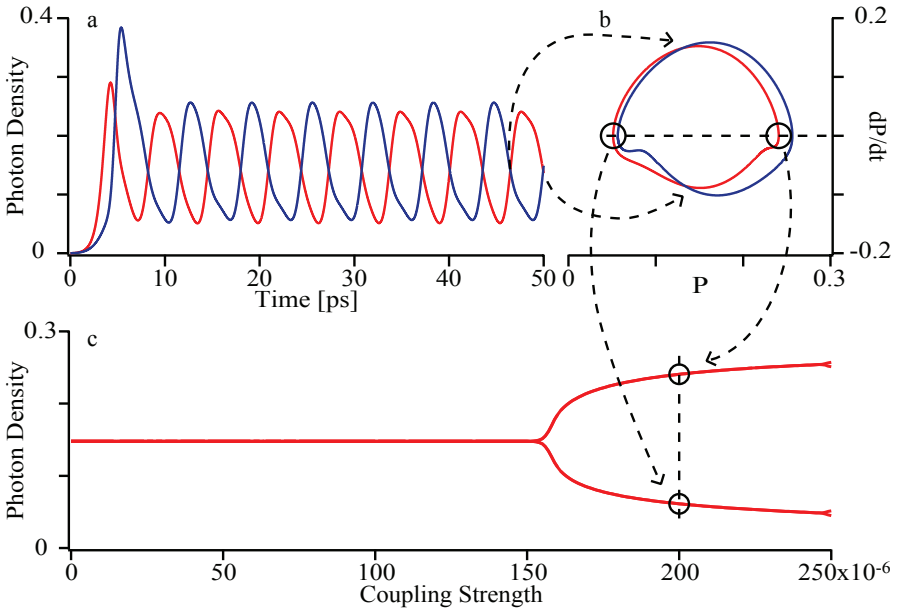

Fig. 6.2: a) The photon density, b) the steady-state phase-space plot and c) the Poincaré map for an example two cavity system.

random noise will perturb these solutions and introduce a coupling and we therefore choose an initial phase difference $\delta\varphi = \frac{\pi}{2}$. In all the simulations, the parameters given in table E.11 were used unless otherwise specified. Solving the modified equations leads to either constant and phase-locked solutions or oscillating solutions depending on the input parameters and the coupling constant. In order to display the phase-locking characteristics of the system in a simple way, we plot the Poincaré map [57] of the steady-state oscillations. The Poincaré map is formed by calculating the steady-state phase-space plot (figure 6.2b) from the evolution of the photon densities (figure 6.2a) and then plotting the points where $d_t P = 0$. As illustrated in figure 6.2c, a constant steady-state solution becomes a single point in the Poincaré map, a simple harmonic oscillation leads to two points, which are seen as a bifurcation and more complicated oscillations show up as several points in the map. Figure 6.3 shows Poincaré maps of the solutions for two coupled cavities as function of κ.

Looking first at a zero detuning case (figure 6.3 top), we see that for negligible coupling ($\kappa < 4 \times 10^{-6}$), the cavities reach constant steady-state solutions and are phase-locked with a constant phase difference (phase-locking regime I). For $\kappa \approx 4 \times 10^{-6}$, the steady-state solutions begin to oscillate harmonically and further increasing the coupling strength leads to more and more bifurcations giving very complicated oscillatory behavior (see insets in figure 6.3). At large coupling strengths ($\kappa > 2 \times 10^{-4}$), the complicated oscillations suddenly collapse and a new phase-locking regime appears (phase-locking regime II).

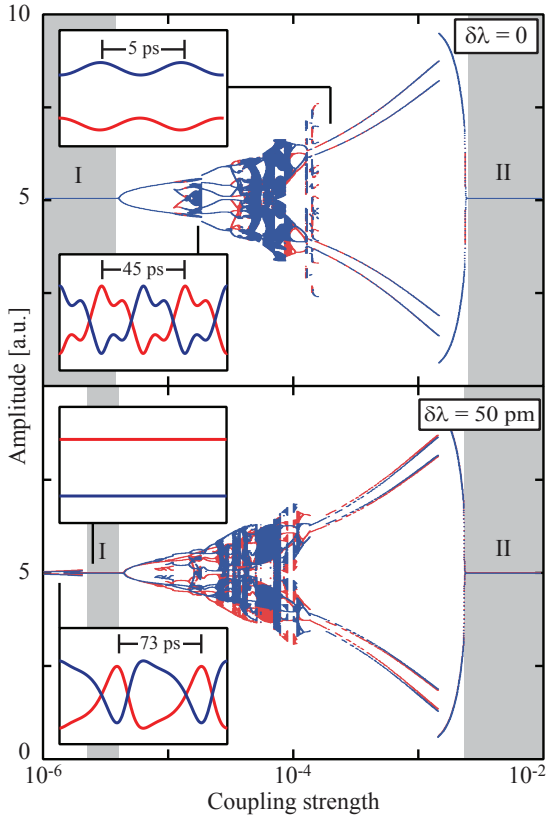

Fig. 6.3: Poincaré map of the steady-state solutions for two coupled cavities for detunings of 0 pm (top) and 50 pm (bottom). The insets show examples of the time evolution of the photon densities at different coupling constants. The colors indicate the amplitudes in cavity A and B and the shaded areas marks the phase-locking regimes I and II. *Parameters in table E.11.*

Due to imperfections in the fabrication processes, the laser cavities will in general differ from each other with variations in the characteristic parameters, including Q-factor, mode volume and resonance frequency. In the bottom part of figure 6.3, we show the Poincaré map for a detuning of 50 pm. In general, the Poincaré map is relatively unchanged except that phase-locking regime I becomes limited from below, where the coupling is dominated by detuning effects. The introduction of detuning is seen to reduce the extent of both phase locking regimes, with regime I being affected at even minute values of the detuning. In both regime I and II, the steady-state photon densities split due to the coupling.

Figure 6.4a shows the dependence of the phase-locking regimes on the coupling strength and detuning (relative to the cavity linewidth), showing that the extent of regimes I and II is strongly affected by detuning, with regime I disappearing for detuning values larger than a critical value that increases with

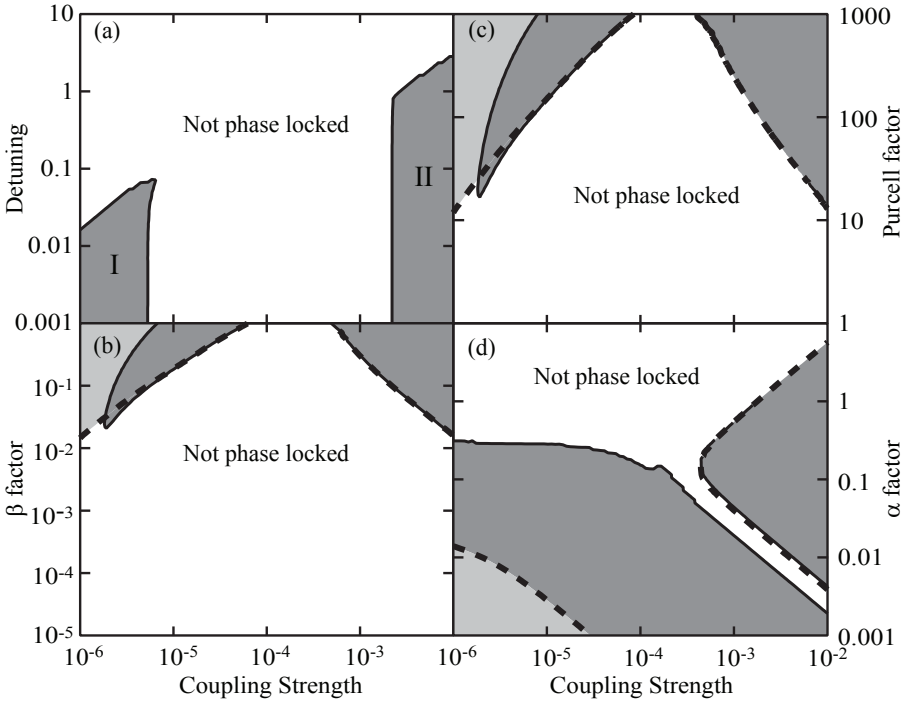

Fig. 6.4: (a) The extend of the phase-locking regimes is shown in the plane of coupling strength and detuning (relative to the cavity linewidth). The shaded areas are phase-locked. (b)-(d) The extend of the phase-locking regimes for zero detuning (dashed line) and for $\delta\lambda = 50$ pm (solid line) in the plane of coupling strength and (b) the β-factor, (c) the Purcell factor and (d) the linewidth enhancement factor. *Parameters in table E.11.*

coupling strength. For realistic detunings imposed by fabrication disorder (a few nanometers), the lower phase-locking bound is already above 10^{-3} and is therefore an important factor to take into account.
Figures 6.4b-d show the extent of the phase-locking regimes as the α, β and effective Purcell factors are varied, with solid (dashed) lines corresponding to $\delta\lambda = 50$ pm ($\delta\lambda = 0$). Figures 6.4b and 6.4c show that surprisingly high values of β and F_{eff} are needed to achieve phase-locking, and that even for zero detuning phase-locking regime II only opens at quite high values of β and F_{eff}. On the other hand, figure 6.4d shows that phase-locking is possible in a much broader range for lower values of the linewidth enhancement factor in agreement with ref. [30].

From the above calculations and from the conclusions drawn in chapter 3.4 about the limitations on the effective Purcell enhancement in QW devices, it seems unlikely that phase-locking can be achieved in QWs. Quantum dot materials seem to be more favorable for coupled cavity systems because of possibility for higher effective Purcell enhancement and lower linewidth enhancement fac-

tors [7, 96–98]. However, a separate analysis using the full LRE model with an exact treatment of the recombination rates is necessary before any conclusions can be drawn in this regard.

7. CONCLUSION AND OUTLOOK

Here we summarize our findings and conclusions. The three main topics, modeling of single nanocavity lasers and light emitting diodes, finite-difference time-domain simulations on structures and modeling of coupled nanocavity lasers will be presented separately.

Modeling of Nanocavity Lasers and Light Emitting Diodes

A laser rate equation model for simulating the characteristics of nanocavity light emitters was set up based on the well-known laser rate equations for conventional semiconductor devices. The spontaneous and stimulated recombination rates were expressed in terms of the optical and electronic density-of-states, so that the Purcell enhancement was taken into account in a rigorous way.

Calculations of the spontaneous emission rate in the full model, revealed a non-trivial dependence on the cavity quality factor. It was found that the enhancement of the spontaneous emission exhibits a severe reduction relative to what is expected from the usual Purcell enhancement. The reduction was shown to appear when the electronic density-of-states is broad relative to the cavity linewidth and the enhancement becomes effectively independent of the quality factor. An effective Purcell factor, which captures the reduction, was introduced and it was found that for quantum well systems, where the electronic density-of-states is typically much broader than the cavity linewidth, the effective Purcell enhancement saturates for a quality factor of a few hundreds. For realistic mode volumes, this makes quantum well system experience only low enhancements, which is of great importance for understanding of this type of system. Quantum dot systems have a much narrower electronic density-of-states and the effective Purcell enhancement therefore saturates for a much higher quality factor (several thousands). Note, that the reduction of the Purcell enhancement pertains to the quality factor only and the effective Purcell enhancement can still be increased by altering the mode volume.

Through small-signal analysis of the full model for quantum well systems, the dynamical properties of nanocavity light emitters was investigated. It was found that the reduction of the Purcell enhancement limits the maximum achievable modulation bandwidth. For reasonable mode volumes, the highest obtainable modulation bandwidth is comparable to that of conventional diode lasers and quantum well nanocavity devices are therefore not advantageous until major improvements of the mode volume have been achieved.

For quantum dot devices operated below threshold, a sizable effective Purcell factor was found, which increased the maximum bandwidth considerable. The homogeneous and inhomogeneous broadening of the electronic density-of-states for quantum dot ensembles was found to be the main limiting factor for the bandwidth. With the lowest realistic broadening, the bandwidth of quantum dot nanocavity light emitting diodes is already competitive with conventional devices and can be further improved by reducing the size of the inhomogeneous broadening.

It was argued that in laser rate modeling of nanocavity systems, the Purcell enhancement should appear in both the spontaneous and stimulated emission term, contrary to common practice. For quantum well devices, the reduction of the Purcell enhancement effectively negates the Purcell effect for quality factors commonly used and modeling using the standard expressions for spontaneous and stimulated emission is permissible in most cases. For quantum dot devices, the inclusion of the Purcell effect in the stimulated emission term is of great importance. Results from the full laser rate equation model were compared to a microscopic model, which includes Purcell enhancement of both recombination processes by default. It was clearly seen that agreement between the two models was only found if a Purcell enhanced stimulated emission rate was used. This conclusion, which to our knowledge is not widely realized, leads to better laser rate equation modeling of quantum dot nanocavity devices and may help to bridge the gap to microscopic modeling of similar systems. Approximate small-signal expressions for the 3dB-frequency was derived and it was seen that the largest modulation bandwidth is found below threshold, where the device is not limited by the cavity linewidth, but rather a combination of the effective Purcell enhancement and the β-factor.

Finite-Difference Time-Domain Simulations

A freely available implementation of the finite-difference time-domain method (`MEEP`) was employed to calculate optical properties of relevant photonic devices. The system consisting of two coupled H1 cavities in a rectangular photonic crystal membrane was studied and in-phase and out-of-phase coupled modes of the combined system was calculated. A surprising alternation of the calculated modes around the resonance frequency of a single isolated cavity was observed. A qualitative explanation for the frequency behavior was linked to the number of holes separating the cavities.

The farfield emission patterns from the isolate single cavity mode, was calculated based on `MEEP` simulations. The emission profile was found to consist of four lobes at large angles from vertical. Similar calculations on the coupled cavity structures revealed a non-trivial dependence on the intercavity separation. Systems with an even number of holes separating the cavities showed clear signs of mode coupling, while odd-number separations of the cavities did not. Rather, when adding the emission patterns for the in-phase and out-of-

phase modes for the odd-number separations the emission patterns resemble the pattern for the single isolated cavity. This behavior is difficult to explain, but is important for design of coupled cavity systems.

Modeling of Coupled Nanocavity Lasers

The system consisting of two coupled cavities was treated in a tight-binding formalism, where the overlapping modes from neighboring cavities lead to coupling terms for the amplitude and phase of the electromagnetic field. The coupling terms were included in a laser rate model, which allowed for a study of the phase-locking behavior of the system. It was found that phase-locking was critically dependent on the exact parameter values and coupling strength. Poincaré maps of the photon density steady-state behavior was plotted as a function of the coupling strength. It was found that increasing the coupling strength leads to more and more complicated oscillatory behavior, which shows up in the Poincaré maps as bifurcations that gives a very rich structure. An upper and lower coupling regime where phase-locking is possible were identified. Estimates of the realistic values for the coupling strength, which can be difficult to calculate, were extracted from finite-difference time-domain calculations.

The dependence of the phase-locking regimes with respect to intercavity detuning, linewidth enhancement factor, spontaneous emission factor and Purcell enhancement was studied. The dependence on the linewidth enhancement factor was especially pronounced and it was concluded that phase-locking in quantum well devices is practically impossible for realistic values of the effective Purcell enhancement and spontaneous emission factor. Quantum dot devices are expected to have lower linewidth enhancement factors and present a promising alternative.

Outlook

The realization that the Purcell effect enhances both spontaneous and stimulated emission was not realized until late in the Ph.D. and Purcell enhanced stimulated emission was therefore not included in the analysis of the quantum well devices. The reduction of the Purcell enhancement effectively negates the Purcell effect for quantum well devices and is therefore not expected to change the conclusions drawn from these calculations, however confirmation through a thorough investigation of the dynamical properties using the Purcell enhanced stimulated emission should be sought.

The optical properties of coupled photonic crystal nanocavities have proven to be a complicated, but interesting system. The non-trivial dependence on the intercavity separation seen in the calculated farfield patterns in section 5.4 is important to understand for design of photonic crystal nanocavity arrays and warrants a detailed analysis of the near-field patterns. Farfield calculations on systems involving more than two cavities are likely to reveal more interesting

behavior and should be analyzed in the light of the two-cavity results.

The tight-binding analysis in chapter 6 showed that phase-locking in quantum well systems is difficult to achieve with realistic parameter values. Quantum dot systems are promising alternatives that requires a separate study using the full model for the Purcell enhanced recombination rates. Estimates of the parameter values necessary for achieving phase-locking in quantum dot systems are of significant practical interest for design of future nanocavity light emitters. Furthermore, the tight-binding analysis of the quantum well devices were done using an expression for the stimulated emission that did not include Purcell enhancement and the results in chapters 6 should be confirmed using a more detailed model for the recombination rates.

APPENDIX

A. PURCELL ENHANCED STIMULATED EMISSION

In this appendix, we examine the steps in the derivation of the recombination rates from Einstein's coefficients that led to the different treatment of Purcell enhancement in the spontaneous and stimulated emission in chapter 3. An alternative approach, which treats the recombination rates on equal footing is outlined and an expression for the total recombination rate, where the same prefactor scales both spontaneous and stimulated emission is derived. The appendix builds heavily on notes by N. Gregersen [64].

The electron-hole recombination rates for a specific transition energy, $h\nu$, between the conduction and valence bands are given in terms of the Einstein A and B coefficients and the available differential carrier densities dN_2 and dN_1

$$dR_{sp}^{21} = AdN_2 \tag{A.1}$$
$$dR_{st}^{21} = BW(\nu)\, dN_2 \tag{A.2}$$
$$dR_{st}^{12} = BW(\nu)\, dN_1 \tag{A.3}$$

where $W(\nu)$ is the radiation spectral density. The Einstein coefficients can be expressed as

$$A = \rho_o(\nu)\, h\nu B \tag{A.4}$$
$$B = \frac{1}{2\hbar^2 n n_g \varepsilon_0} \tag{A.5}$$

where ρ_o is the optical DOS, n and n_g are refractive and group indices and ε_0 is the vacuum permittivity. In thermal equilibrium, the radiation spectral density can be written as

$$W(\nu) = h\nu f_B(\nu)\, \rho_o(\nu) \tag{A.6}$$

where f_B is the Boltzmann distribution. As shown in section 3.2, the Purcell enhancement enters the spontaneous emission expression through the optical DOS and as the optical DOS appears in the expression for both the spontaneous and stimulated emission, it seems likely that both recombination rates should be Purcell enhanced. However, eqn. (A.6) describes closed systems in thermal equilibrium, which does not include a laser cavity. Therefore, in order to reach equations useful for describing laser devices, the radiation spectral density in eqn. (A.6) is often replaced by

$$W(\nu) = h\nu P\delta(\nu - \nu_c) \tag{A.7}$$

That is, a radiation spectral density, which concentrate the energy, $h\nu P$, at the laser frequency, ν_c, and thus mimics the behavior of a laser. Using the definition in eqn. (A.7), the well-known stimulated emission rate can be derived from eqns. (A.1)-(A.3). However, using eqn. (A.7) removes the optical density (and therefore also the Purcell enhancement) from the equations leading to stimulated emission. An approach more suitable for nanocavities is to return to eqn. (A.6) and replace the equilibrium Boltzmann distribution with another distribution that describes the non-equilibrium operation of the laser.

One possible generalization is to assume that primarily one quasi mode is excited and write the radiation spectral density as

$$W\left(\hat{\boldsymbol{d}}, \boldsymbol{r_0}, \nu\right) = \hbar\nu P \rho_L\left(\hat{\boldsymbol{d}}, \boldsymbol{r_0}, \nu\right) \tag{A.8}$$

where the local optical DOS, ρ_L, includes details of both the spectral and spatial variation of the field ($\hat{\boldsymbol{d}}$ and $\boldsymbol{r_0}$ are the dipole orientation and position), which is appropriate for an inhomogeneous optical medium as the one studied here. Equations (A.1)-(A.3) change accordingly to

$$dR_{sp}^{21} = \rho_L\left(\hat{\boldsymbol{d}}, \boldsymbol{r_0}, \nu\right) \hbar\nu B^G dN_2 \tag{A.9}$$

$$dR_{st}^{21} = W\left(\hat{\boldsymbol{d}}, \boldsymbol{r_0}, \nu\right) B^G dN_2 \tag{A.10}$$

$$dR_{st}^{12} = W\left(\hat{\boldsymbol{d}}, \boldsymbol{r_0}, \nu\right) B^G dN_1 \tag{A.11}$$

where $B^G = nn_g B$ and the factor nn_g appears because ρ_L includes the general non-uniform dielectric constant in its normalization. The total differential recombination rates are formed by taking the difference between eqns. (A.10) and (A.11). Following the approach in section 3.2, the infinitesimal contributions to the number of state pairs for the upwards and downwards transitions, i.e.

$$dN_c = f_c\left(E_{21}\right)\left(1 - f_v\left(E_{21}\right)\right)\rho_e\left(E_{21}\right) dE_{21} \tag{A.12}$$

$$dN_v = f_v\left(E_{21}\right)\left(1 - f_c\left(E_{21}\right)\right)\rho_e\left(E_{21}\right) dE_{21} \tag{A.13}$$

are inserted and the homogeneous broadening is included as a convolution with $L\left(h\nu - E_{21}\right)$. This yields the equations

$$\begin{aligned} R_{sp} = B^G \int \rho_L\left(\hat{\boldsymbol{d}}, \boldsymbol{r_0}, \nu\right) h\nu f_c\left(E_{21}\right)\left(1 - f_v\left(E_{21}\right)\right) \\ \times \rho_e\left(E_{21}\right) L\left(h\nu - E_{21}\right) dh\nu dE_{21} \end{aligned} \tag{A.14}$$

$$\begin{aligned} R_{st} = B^G \int W\left(\hat{\boldsymbol{d}}, \boldsymbol{r_0}, \nu\right)\left(f_c\left(E_{21}\right) - f_v\left(E_{21}\right)\right) \\ \times \rho_e\left(E_{21}\right) L\left(h\nu - E_{21}\right) dh\nu dE_{21} \end{aligned} \tag{A.15}$$

Inserting the radiation spectral density, the total recombination rate can be written

$$\begin{aligned} R_{sp} + R_{st} = B^G \int \rho_L\left(\hat{\boldsymbol{d}}, \boldsymbol{r_0}, \nu\right) h\nu \\ \times \left[f_c\left(E_{21}\right)\left(1 - f_v\left(E_{21}\right)\right) + P\left(f_c\left(E_{21}\right) - f_v\left(E_{21}\right)\right)\right] \\ \times \rho_e\left(E_{21}\right) L\left(h\nu - E_{21}\right) dh\nu dE_{21} \end{aligned} \tag{A.16}$$

Assuming that the spectral variation of the local density of states is described by a Lorentzian reflecting the Q-factor of the cavity as

$$\rho_L\left(\hat{\boldsymbol{d}}, \boldsymbol{r_0}, \nu\right) = \rho_L\left(\hat{\boldsymbol{d}}, \boldsymbol{r_0}, \nu_c\right) \frac{\left(\frac{1}{2}\delta\nu_c\right)^2}{\left(h\nu - h\nu_c\right)^2 + \left(\frac{1}{2}\delta\nu_c\right)^2} \tag{A.17}$$

we have

$$\begin{aligned} R_{sp} + R_{st} = \rho_L\left(\hat{\boldsymbol{d}}, \boldsymbol{r_0}, \nu_c\right) B^G \int \frac{\left(\frac{1}{2}\delta\nu_c\right)^2}{\left(h\nu - h\nu_c\right)^2 + \left(\frac{1}{2}\delta\nu_c\right)^2} h\nu \\ \times \left[f_c\left(E_{21}\right)\left(1 - f_v\left(E_{21}\right)\right) + P\left(f_c\left(E_{21}\right) - f_v\left(E_{21}\right)\right)\right] \rho_e\left(E_2 1\right) \\ \times L\left(h\nu - E_{21}\right) dh\nu dE_{21} \end{aligned} \tag{A.18}$$

From this expression it is clear that the spontaneous and stimulated emission rates are scaled by the same prefactor, $\rho_L\left(\hat{\boldsymbol{d}}, \boldsymbol{r_0}, \nu_c\right)$, which contains any Purcell enhancement. Thus, the two recombination rates should feel the same light-matter interaction.

B. MEEP RECIPES

In this appendix, we include a short instruction in setting up and running MEEP scripts on the Linux cluster computer at DTU Fotonik (named kloster) using the C++ interface. It is thought as a help for people at DTU Fotonik, who need to work with MEEP. Readers not interested in the particulars of setting up MEEP scripts can skip this appendix entirely.

Scripts in MEEP can be set up in using either of two interfaces. The first is the Scheme[1] interface, which is well documented [79] and relatively easy to use. However, in the Scheme interface the structures are created from basic, predefined shapes (slabs, boxes, spheres, cylinders, etc.) and not all structures can easily be constructed. Greater flexibility is possible by using the underlying C++ interface, where one has access to the basic MEEP functions that the Scheme interface calls. The C++ interface is not as well documented as the Scheme interface and it is often necessary to go hunting through the source code for a specific function or syntax. However, using C++, we have full control over the structure construction and can work in a more mainstream programming language.

We use the C++ interface and explore some of the functionality through practical examples. The tutorial should be read after the general introduction to MEEP on the program's homepage [79],

Dipole Source in Vacuum

To see the basic structure of the MEEP script, we begin with the simplest possible example: A dipole emitter in free space. Start by logging on to kloster with a Secure Shell (SSH) client. Use kloster.com.dtu.dk for the "host name" and log on using your DTU credentials. Create a new folder "tutorial" with mkdir tutorial and navigate to it with cd tutorial. Create a new file (DEIFS.cpp) using your favorite text editor, e.g. EMACS, by entering emacs DEIFS.cpp (EMACS automatically creates a new file if it does not already exist). Input the following program:

```
// Include the MEEP library and other useful functions
#include <meep.hpp>
#include <fstream>

using namespace meep;
```

[1] Scheme is a programming language developed at Massachusetts Institute of Technology

```
// Define constants that we will need
const int res       = 20;          // How many points per lattice constant
const double d_pml  = 1.0;         // Thickness of PML layer
const double epsbck = 1.0;         // Background permittivity (vacuum)
const double sx     = 5 + 2*d_pml; // Cell length x
const double sy     = 5 + 2*d_pml; // Cell length y
const double fc     = 0.2;         // Center frequency of source
const double fw     = 0.1;         // Spectral width of source
const double mtime  = 75;          // H$ow long to run the simulation
const string fn     = "DEIFS";     // Filename for output purposes

complex<double> * Hz_data;         // Data storage

// Define epsilon function
double eps_empty(const vec &p){return epsbck;}

// Here comes the main program
int main(int argc, char **argv){

  initialize mpi(argc, argv);

  // Set up structure
  grid_volume vol = vol2d(sx, sy, res);          // The computational cell
  structure s(vol, eps_empty, pml(d_pml));       // Draw the structure
  fields f(&s);                                  // Initialize the fields

  // Set up source
  gaussian_src_time src(fc, fw);                 // Temporal aspect of source
  f.add_point_source(Hz, src, vol.center());     // Spatial aspect of source

  // Set up data collection
  const int Ntime = floor(mtime/f.dt);           // f.dt is the temporal resolution
  Hz_data = new complex<double> [Ntime];         // Number of data points

  // Run the simulation
  int ii = 0;
  while(f.time() < mtime){
    f.step();                                    // Step the time
    Hz_data[ii] = f.get_field(Hz, vol.center()); // Collect field
    ii++;
  }

  // Output time evolution of field
  ofstream fs;
  string str = fn + "_re.txt";
  fs.open(str.c_str(), ios::out);
  for(int m=0; m<Ntime; m++){fs << real(Hz_data[m]) << "\n";}

  // Output spatial field profile
  h5file *foo = f.open_h5file(fn.c_str());
  f.output_hdf5(Hz, vol.surroundings(), foo);
  fs.close();

  return 0;
}
```

Here, we first defined the various parameters that is used in the program and the dielectric function. The dielectric function takes a vector to a point in the computational cell and should return the value of the dielectric profile at that point. In the case of free space, the dielectric function is 1 everywhere. After this, the main program is initiated, the structure is set up (`structure` sweeps the structure volume and passes the vector to the epsilon function) and the $\mathcal{H}_z$ point source is added to the center. In the loop, time is advanced one step each time `f.step()` is called, so that the time stepping ends when the loop condition evaluates to false. The final lines outputs the collected data.

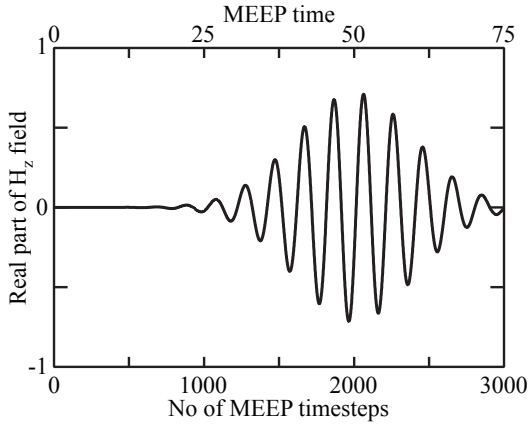

Fig. B.1: Time evolution of the $\mathcal{H}_z$ component of a dipole emitter in free space.

Save the file and return to the command prompt. Now we need to compile the script, input the following two commands[2]

```
export PKG_CONFIG_PATH="/usr/local/lib/pkgconfig/"

pathCC ‘pkg-config --cflags meep‘ DEIFS.cpp -o DEIFS ‘pkg-config --libs meep‘ -OPT:Olimit=0
```

The second line compiles the script and produces a new file (`DEIFS`, no type extension). To run the script, we can either submit it to the `kloster` queue system or we can run it interactively in the terminal. The latter is the easiest and allowable[3] for short programs. Enter the command

```
./DEIFS
```

After the program finishes, type `ls` at the command prompt to list the directory. Two new files have appeared. `DEIFS.h5`, contains the spatial field profile at the end of the simulation and `DEIFS_re.txt` contains the real part of the time evolution of the field in the center. Plotting the data in `DEIFS_re.txt` gives us the time series in figure B.1. The figure shows the real part of the $\mathcal{H}_z$ component of the field in the center of the computational cell. Notice that the amplitude follows the Gaussian shape that we specified above and reflects the frequency width, `fw`. The number of `MEEP` time steps are connected to the (normalized) `MEEP` time through the resolution, so that

$$\text{MEEP time} = \text{Courant factor} \times \frac{\text{number of time steps}}{\text{resolution}} \tag{B.1}$$

The Courant factor is important for the stability of the FDTD code and is set to $\frac{1}{2}$ in `MEEP`. Therefore, in this case $75 = \frac{1}{2} \times 3000/20 =$ `mtime`. Plotting the spatial field in `DEIFS.h5` requires some more post processing. Input

[2] The first line is only necessary once per SSH session.

[3] The host `kloster.com.dtu.dk` is mainly used for submitting jobs to the queue and are shared by many users. Running long programs interactively will quickly use up the limited system resources and it is therefore in general better to submit jobs to the queue.

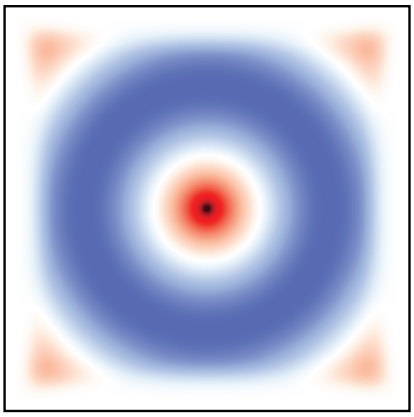

Fig. B.2: The spatial distribution of the $\mathcal{H}_z$ component of a dipole emitter in free space.

```
H5topng -S3 -Zc dkbluered DEIFS.h5
```

That is, convert the .h5 file to a .png, scale it up 3 times and change the colormap to dark-blue-red. This produces the .png file shown in figure B.2. We see that the field radiates out from the center, where the dipole emitter was positioned and that the field rapidly goes to zero once it enters the PML layer. Notice, that in the calculations set up in the C++ interface, the PML layer overlaps with the computational cell, unlike in the Scheme interface where it is padded onto the cell. Therefore, in C++ calculations, we must remember to add the PML layer thickness to the total size of the computational domain.

Cylindrical Bragg Cavity

A more interesting example is based on the cylindrical Bragg cavity [11, 99], which constitutes a 2D Bragg stack with alternating layers of high and low refractive indices. Create a new file `CBC.cpp` and input the following program

```
// Include the MEEP library and other useful functions
#include <meep.hpp>
#include <fstream>

using namespace meep;

// Define constants that we will need
const int res       = 20;           // How many points per lattice constant
const double d_pml  = 1.0;          // Thickness of PML layer
const double epsbck = 1.0;          // Background permittivity (air)
const double epsmat = 12.25;        // Background permittivity (n = 3.5)
const double sx     = 10 + 2*d_pml; // Cell length x
const double sy     = 10 + 2*d_pml; // Cell length y
const double fc     = 0.2;          // Center frequency of source
const double fw     = 0.1;          // Spectral width of source
const double TAS    = 100;          // Time after source
const string fn     = "CBC";        // Filename for output purposes

complex<double> * Hz_data;          // Data collection variable
```

```
// Define epsilon function
double eps_CBC(const vec &p){
   const double r = sqrt(pow(p.x()-sx/2, 2) + pow(p.y()-sy/2, 2));

   if(r <  0.4746){return epsmat;}
   if(r <  2.1358){return epsbck;}
   if(r <  2.3732){return epsmat;}
   if(r <  4.0344){return epsbck;}
   if(r <  4.2717){return epsmat;}
   if(r <  5.9329){return epsbck;}
   if(r <  6.1702){return epsmat;}
   if(r <  7.8314){return epsbck;}
   if(r <  8.0687){return epsmat;}
   if(r <  9.7300){return epsbck;}
   if(r <  9.9673){return epsmat;}
   if(r < 11.6285){return epsbck;}
   if(r < 11.8658){return epsmat;}
   if(r < 14.3576){return epsbck;}
   if(r < 14.5949){return epsmat;}
   if(r < 16.2562){return epsbck;}

   return epsbck;
}

// Here comes the main program
int main(int argc, char **argv){

  initialize mpi(argc, argv);

  // Set up structure
  grid_volume vol = vol2d(sx, sy, res);          // The computational cell
  structure s(vol, eps_CBC, pml(d_pml));         // Draw the structure
  fields f(&s);                                  // Initialize the fields

  // Set up source
  gaussian_src_time src(fc, fw);                 // Temporal aspect of source
  f.add_point_source(Hz, src, vol.center());     // Spatial aspect of source

  // Set up data collection
  const int Ntime = floor((f.last_source_time() + TAS)/f.dt);
  Hz_data = new complex<double> [Ntime];         // Number of data points
  int maxbands = 5;
  complex<double> *amps = new complex<double>[maxbands];
  double *freq_re = new double[maxbands];
  double *freq_im = new double[maxbands];

  // Run the simulation
  int ii = 0;
  while(f.time() < f.last_source_time() + TAS){
    f.step();                                    // Step the time
    Hz_data[ii] = f.get_field(Hz, vol.center()); // Collect field
    ii++;
  }

  // Output structure
  f.output_hdf5(Dielectric, vol.surroundings());

  // Output time evolution of field
  ofstream fs;
  string str = fn + "_re.txt";
  fs.open(str.c_str(), ios::out);
  for(int m=0; m<Ntime; m++){fs << real(Hz_data[m]) << "\n";}

  // Output spatial field profile
  h5file *foo = f.open_h5file(fn.c_str());
  f.output_hdf5(Hz, vol.surroundings(), foo);

  // Calculate modes
  int num =  do_harminv(Hz_data, Ntime, f.dt, 0.8*fc, 1.2*fc, maxbands, amps, freq_re, freq_im);
  master_printf("frequency,quality factor\n");
```

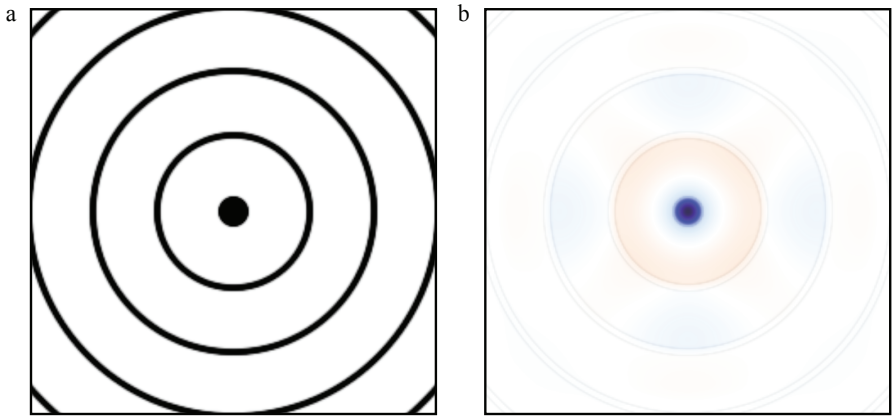

Fig. B.3: a) The dielectric profile of a cylindrical Bragg cavity and b) the calculated $\mathcal{H}_z$ component of the field.

```
  for (int i=0; i<num; ++i){
    master_printf("%0.6g,%g\n",freq_re[i],-0.5*freq_re[i]/freq_im[i]);
  }

  // Clean up
  fs.close();

  return 0;
}
```

In this case, the epsilon function describes concentric layers of material with alternating dielectric constants. The thicknesses of the layers are chosen so they coincide with the zeros and extrema of a zeroth order Bessel function. The epsilon structure is saved to the hard drive (`eps-000250.00.h5`) and we plot with

```
H5topng -S3 eps-000250.00.h5
```

which yields the .png file shown in figure B.3a. We can overlay this picture on the spatial field profile using

```
H5topng -S3 -Zc dkbluered -a yarg -A eps-000250.00.eps CBC.h5
```

That is, convert `CBC.h5` to a .png, scale it up 3 times, change colormap to `dkbluered`, overlay eps-000250.00.h5 and change the colormap of the overlay to `yarg` (grays). This gives the field profile shown in figure B.3b. We see that the field is concentrated in the center high index material and quickly dies out away from the center.

In figure B.4, we again plot the time evolution of the field. Notice that the field lives for a longer time compared to figure B.1, indicating that we have excited a mode of the structure with a high Q-factor. The spectral position and the Q of the mode is calculated by the program using harmonic inversion [100] and printed to the screen. The result is

```
frequency,quality factor
0.214722,1041.95
```

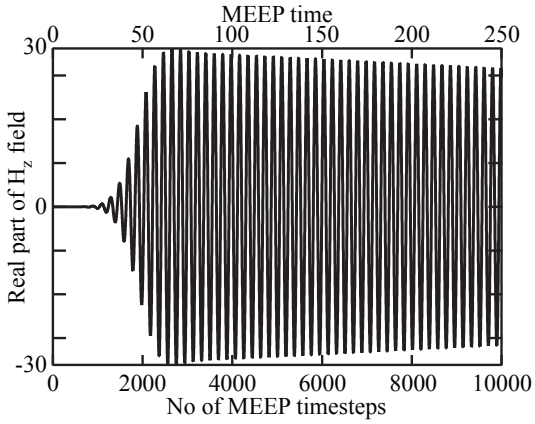

Fig. B.4: Time evolution of the $\mathcal{H}_z$ component of a cylindrical Bragg cavity mode.

It confirms that there is a mode at 0.214722 c/a (c being the speed of light and a being the lattice constant) with a Q of more than[4] 1000.

Reducing Calculation Time

Notice that the calculation time is printed out in the end. In the above calculation, the runtime was around 70 s. which is not a lot. However, this was a 2D calculation on a relatively small computational cell. In 3D calculations, the calculation time increases drastically and can take several days to finish. Luckily, we can employ a number of tricks to reduce the calculation time.

First, we can exploit symmetries to reduce the size of the calculation cell. If the structure is symmetric in the epsilon function and the sources, we can reduce the calculation cell to the smallest asymmetric cell. In the cylindrical Bragg cavity example, we had concentric rings and a source in the center. This allows for several symmetries. We can choose the mirror symmetries in x- and y-directions through zero, so that we only need to calculate the fields in one quadrant. This is implemented by changing

```
// Set up structure
grid_volume vol = vol2d(sx, sy, res);          // The computational cell
structure s(vol, eps_CBC, pml(d_pml));         // Draw the structure
fields f(&s);                                  // Initialize the fields
```

in the script above to

```
// Set up structure
grid_volume vol = vol2d(sx, sy, res);          // The computational cell
const symmetry Sx = mirror(X, vol);
const symmetry Sy = mirror(Y, vol);
structure s(vol, eps_CBC, pml(d_pml), -Sx-Sy); // Draw the structure
fields f(&s);                                  // Initialize the fields
```

[4] In this example, we just estimated the thickness of each layer and the low Q is due to the layer thicknesses being slightly off. Much higher Q-factors can be found by fine tuning the structure parameters.

Compiling and running the program again gives the same result, but now it only takes 15 s.

Notice that we wrote the symmetries with a minus sign. This is because we have chosen a magnetic dipole source, i.e. the $\mathcal{H}_z$ component. Magnetic sources transform as pseudo-vectors, while electric sources transform as vectors. Take the value of the electric field vector at position (x, y, z) to be $(\mathcal{E}_x, \mathcal{E}_y, \mathcal{E}_z))$. If we mirror that field vector in the xy-plane it moves to position $(x, y, -z)$ and the field vector changes to $(\mathcal{E}_x, \mathcal{E}_y, -\mathcal{E}_z))$. Had it been a magnetic vector, $(\mathcal{H}_x, \mathcal{H}_y, \mathcal{H}_z))$, it would still move to position $(x, y, -z)$, but the field vector would change to $(-\mathcal{H}_x, -\mathcal{H}_y, \mathcal{H}_z))$. Notice also that the above `-Sx-Sy` transformation is only valid if the source is at the origin. We can move the source to another position, but only if we also introduce new sources that are mirrored in the axes. If we neglect to do so, `MEEP` produces "undefined" results, which usually means that the fields will diverge after a while.

Another symmetry transformation is possible, namely to exploit the full cylindrical symmetry of the structure. In this case, we need to change to cylindrical coordinates, which is done by specifying the volume with `volcyl` instead of `vol2d` and change the epsilon function to specify the structure in the rz-plane. The rest is the same although vectors are constructed using `veccyl` instead of `vec`. Finally, we can also specify 90 and 180 degrees rotational symmetry using `rotate4` and `rotate2`.

Another approach to reducing the runtime, is to enable sub-pixel averaging. In figure B.3a, the rings seem to be pixelated, which is due to the finite resolution that can be applied in FDTD. So the actual structure that is being simulated includes these ragged edges between high and low index materials, which changes the predicted modes. Of course, we could just increase the resolution, but the number of grid points would then also increase (quadratically for 2D and cubically for 3D) making the simulation slow. Instead, we can enable sub-pixel averaging, which is a method to smooth out discontinuities in the epsilon function by calculating an averaged value of the epsilon function. This method can produce converged results for lower resolutions (c.f. section 5.2). Two things are worth noting: 1) `MEEP` spends some time calculating the averaged structure, so for short calculations sub-pixel averaging might not be an advantage. 2) `MEEP` has been known to have stability problems in 3D with sub-pixel averaging turned on (the fields simply diverges at some point), so one need to check that `MEEP` is producing correct results when doing 3D simulations[5].

Sub-pixel averaging is turned on by changing

[5] Both these issues are eliminated in the Scheme interface, where the dielectric structures are constructed from predefined basic shapes rather than from a user-defined epsilon function. The advantage of using predefined shapes is that exact solutions of the sub-pixel averaging of these shapes are known. For a predefined arbitrary epsilon function, the sub-pixel averaging routine needs to sample the epsilon function in many points until a self-consistent solution is found [78, 80].

```
// Set up structure
grid_volume vol = vol2d(sx, sy, res);          // The computational cell
const symmetry Sx = mirror(X, vol);
const symmetry Sy = mirror(Y, vol);
structure s(vol, eps_CBC, pml(d_pml), -Sx-Sy); // Draw the structure
fields f(&s);                                  // Initialize the fields
```

to

```
// Set up structure
grid_volume vol = vol2d(sx, sy, res);          // The computational cell
const symmetry Sx = mirror(X, vol);
const symmetry Sy = mirror(Y, vol);
structure s(vol, eps_CBC, pml(d_pml), -Sx-Sy); // Draw the structure
s.set_epsilon(eps_CBC, true);
fields f(&s);                                  // Initialize the fields
```

Running this program, we notice that the computation time actually increased to 40 s, which is a result of this being a fairly short calculation. The benefit of sub-pixel averaging is better seen for longer calculations. The result of the harmonic inversion is also changed

```
frequency,quality factor
0.16626,220.463
0.212777,770.084
```

The mode we found before has moved slightly, Q is changed and in addition another mode has appeared.

C. ADDITIONAL MODES AND FARFIELD PLOTS

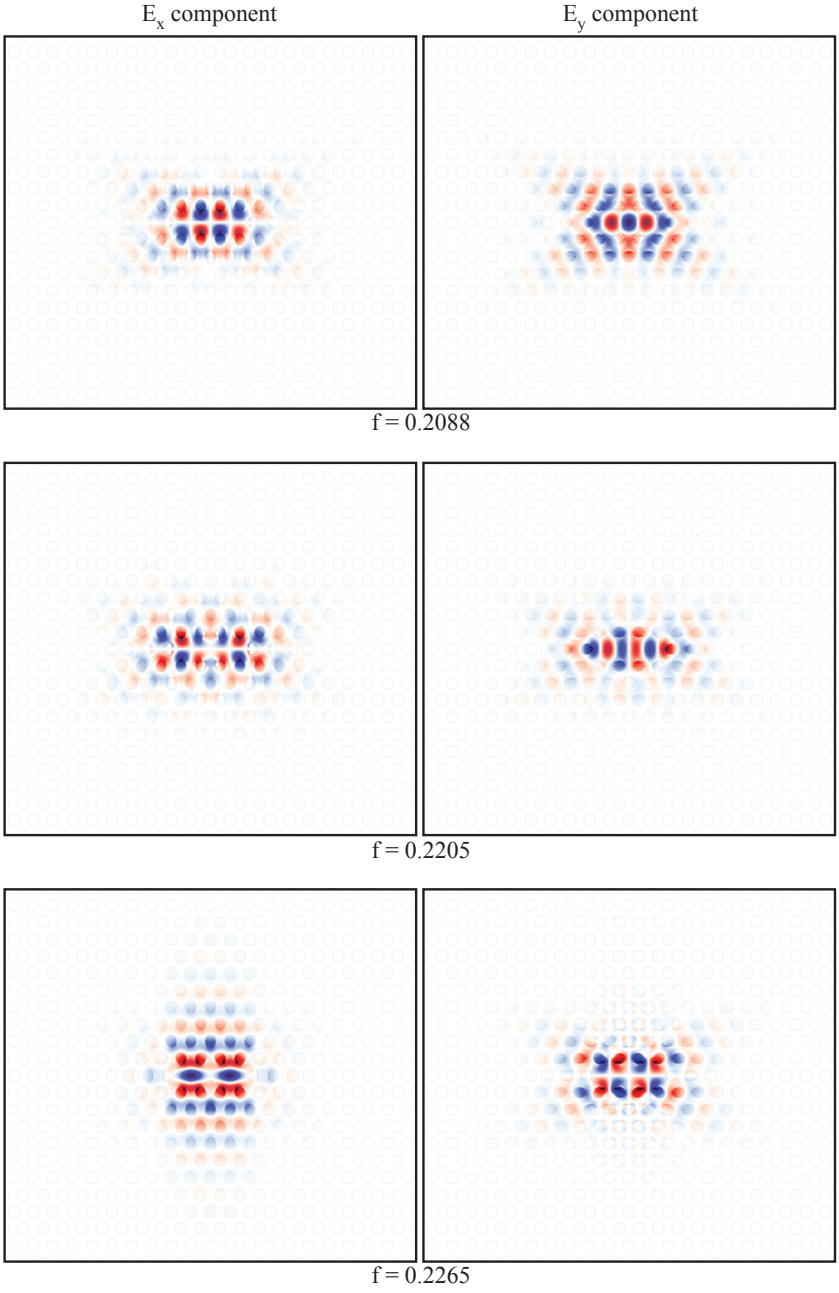

Fig. C.1: $\mathcal{E}_x$ and $\mathcal{E}_y$ components of the calculated 2D modes of the modified Noda cavity. *Parameters in table E.9.*

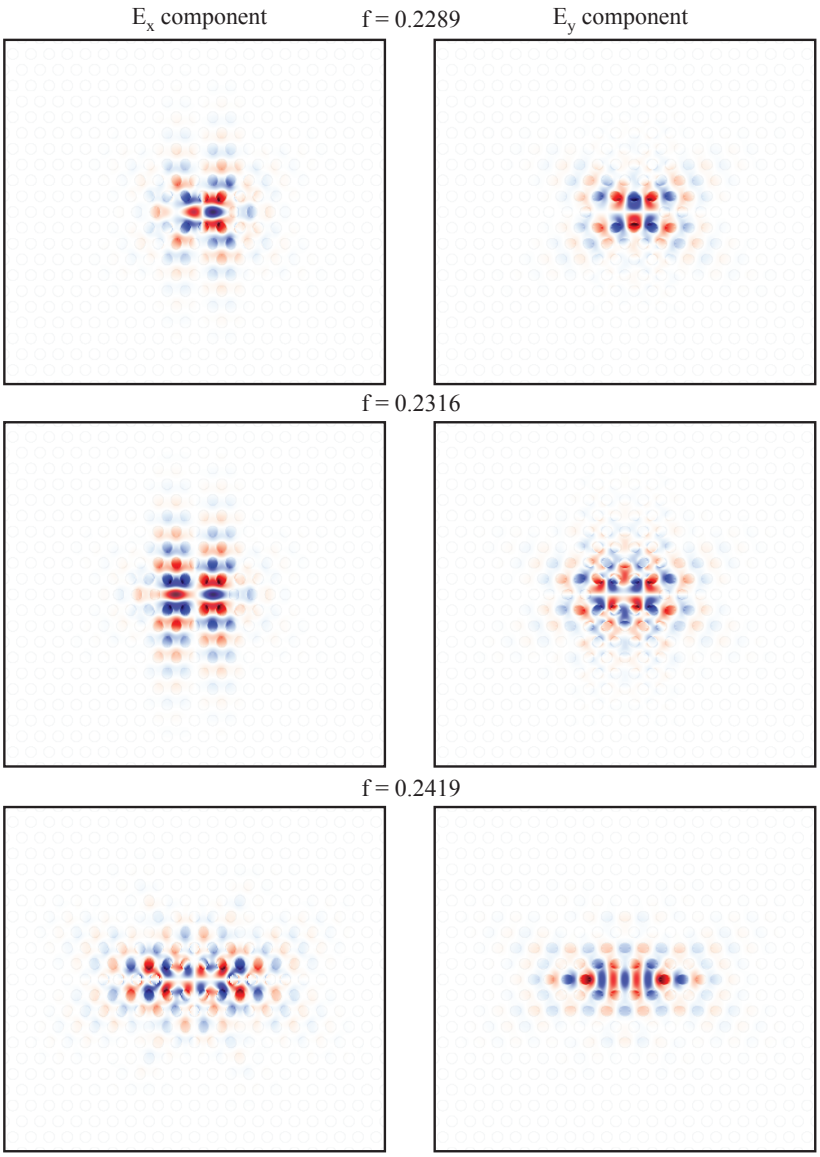

Fig. C.2: $\mathcal{E}_x$ and $\mathcal{E}_y$ components of the calculated 2D modes of the modified Noda cavity. *Parameters in table E.9.*

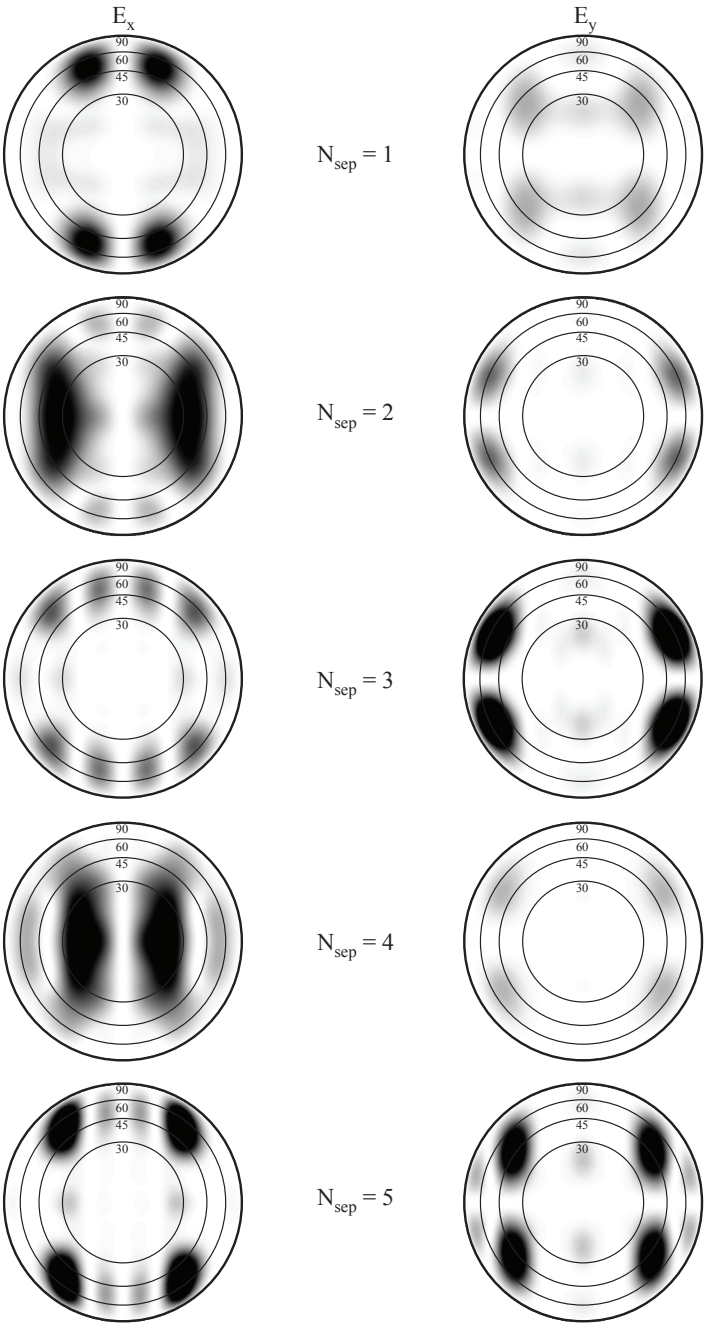

Fig. C.3: Calculated $\mathcal{E}_x$ and $\mathcal{E}_y$ components of the farfield for two coupled H1 cavities. Coupling in ΓX-direction and quadrupole modes in phase.

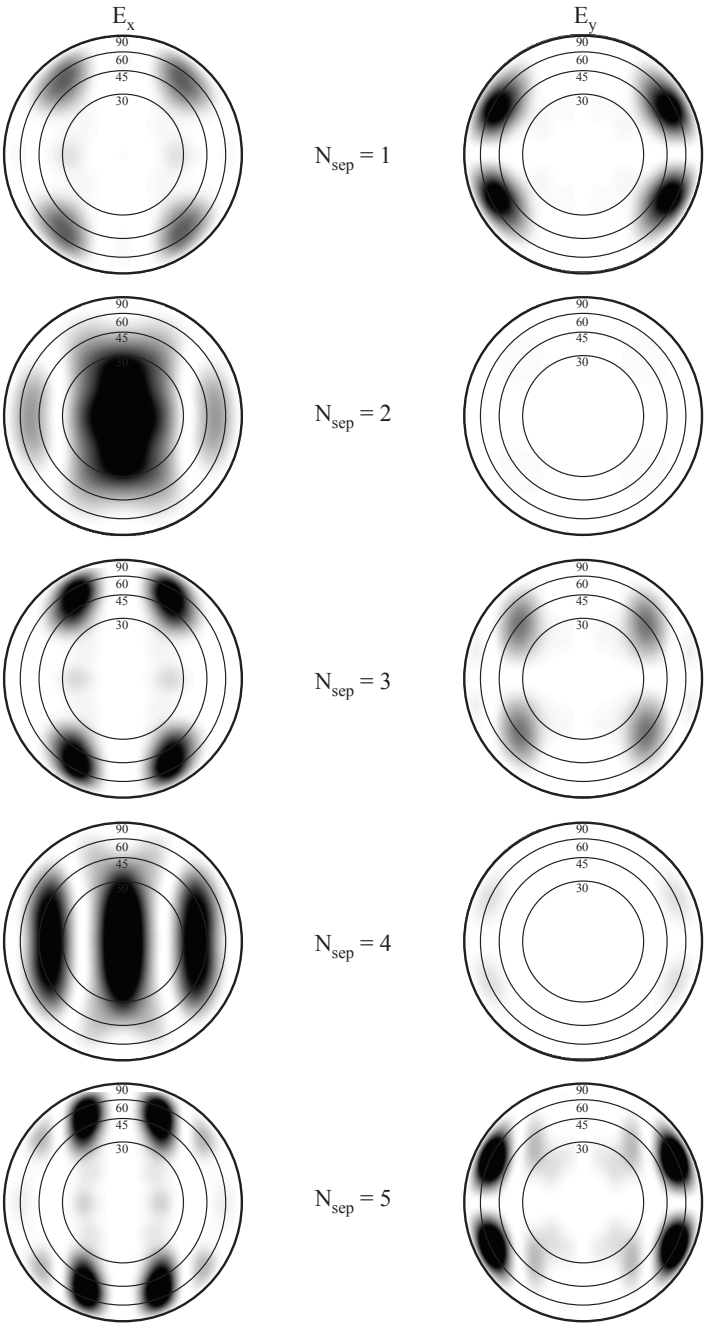

Fig. C.4: Calculated $\mathcal{E}_x$ and $\mathcal{E}_y$ components of the farfield for two coupled H1 cavities. Coupling in ΓX-direction and quadrupole modes out of phase.

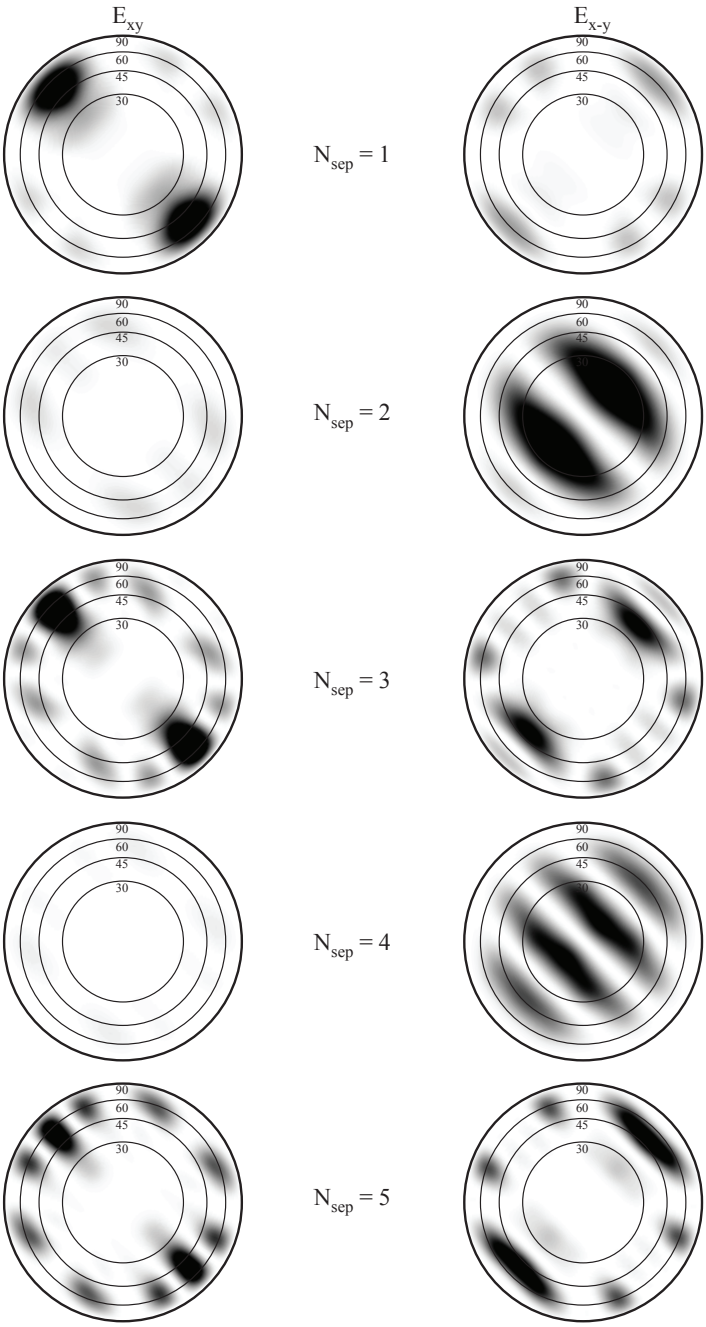

Fig. C.5: Calculated $\mathcal{E}_{xy}$ and $\mathcal{E}_{x-y}$ components of the farfield for two coupled H1 cavities. Coupling in ΓM-direction and quadrupole modes in phase.

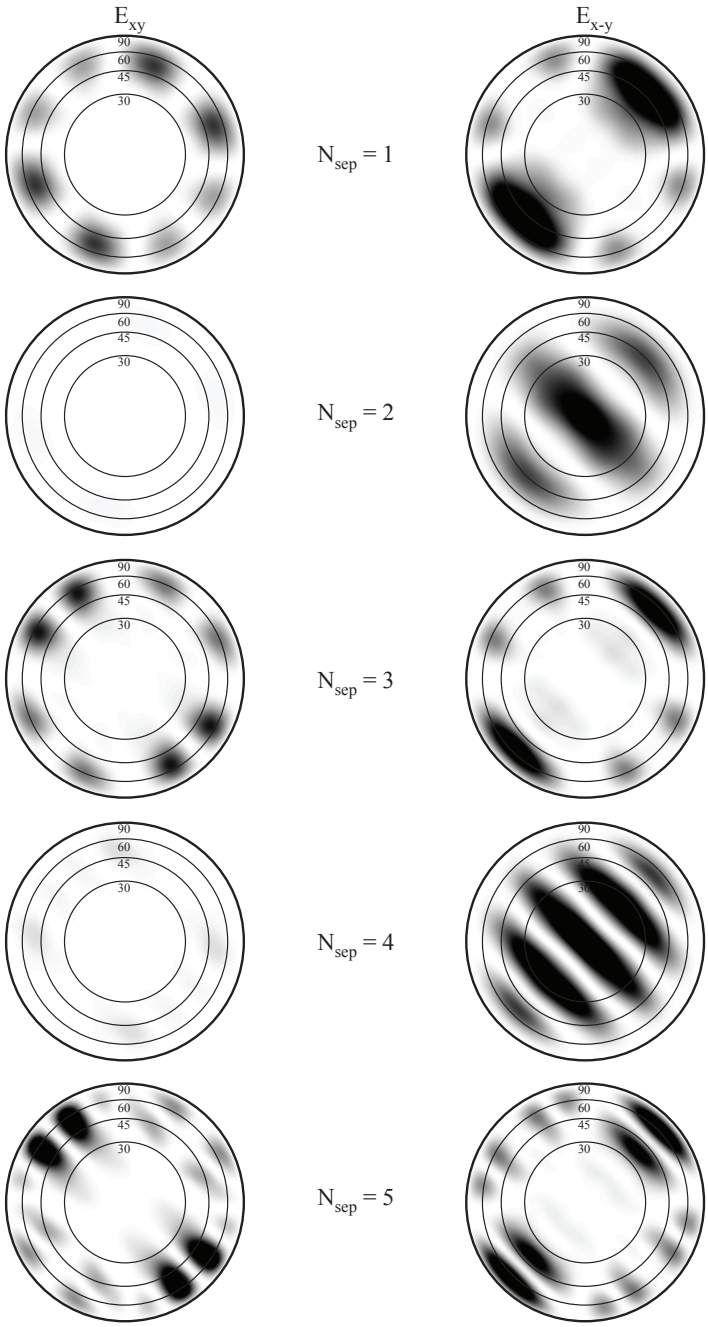

Fig. C.6: Calculated $\mathcal{E}_{xy}$ and $\mathcal{E}_{x-y}$ components of the farfield for two coupled H1 cavities. Coupling in ΓM-direction and quadrupole modes out of phase.

D. TIGHT BINDING MODEL

We consider a system of two neighboring cavities as the one shown in fig. D.1 and derive equations for the coupling following [31, 94]. Each cavity, q, is made as a defect in a photonic crystal and has a dielectric profile $\varepsilon_q = \varepsilon_q(\boldsymbol{r})$ that consist of a background contribution, $\varepsilon_b = \varepsilon_b(\boldsymbol{r})$, from the periodic photonic lattice and a perturbation, $\Delta\varepsilon_q = \Delta\varepsilon_q(\boldsymbol{r})$ arising from the photonic crystal defect. All in all, the dielectric profile for a single cavity is given by $\varepsilon_q = \varepsilon_b + \Delta\varepsilon_q$ and a schematic of the variation of the dielectric constant along a line connecting two neighboring cavities is shown in fig. D.2.

To derive equations for the coupling between the cavities, we need to solve the Maxwell wave equation

$$c^2\boldsymbol{\nabla}^2\boldsymbol{\mathcal{E}} = \partial_t^2\boldsymbol{\mathcal{E}} + \frac{1}{\varepsilon_0}\partial_t^2\boldsymbol{\mathcal{P}} \tag{D.1}$$

where $c^2 = \frac{1}{\varepsilon_0\mu_0}$ is the speed of light in vacuum, ε_0 is the vacuum permittivity and μ_0 is the vacuum permeability. $\boldsymbol{\mathcal{E}} = \boldsymbol{\mathcal{E}}(\boldsymbol{r},t)$ is the electric field and $\boldsymbol{\mathcal{P}} = \boldsymbol{\mathcal{P}}(\boldsymbol{r},t)$ is the polarization.

We take the polarization[1] to be $\boldsymbol{\mathcal{P}} = (\varepsilon - \varepsilon_0)\boldsymbol{\mathcal{E}}$ and rewrite the wave equation to

$$c^2\boldsymbol{\nabla}^2\boldsymbol{\mathcal{E}} = \varepsilon_r\partial_t^2\boldsymbol{\mathcal{E}} \tag{D.2}$$

where $\varepsilon_r = \frac{\varepsilon}{\varepsilon_0}$ is the relative dielectric profile. We drop the subscript r and remember that in the following we mean the relative dielectric profile.

We assume that we may expand the total electric field from the cavities A and B in the quasi modes, Φ, of the uncoupled cavities

$$\boldsymbol{\mathcal{E}}_A = \sum_{n=0}^{\infty} A_n\boldsymbol{\Phi}_n^A, \quad \boldsymbol{\mathcal{E}}_B = \sum_{n=0}^{\infty} B_n\boldsymbol{\Phi}_n^B \tag{D.3}$$

where the expansion coefficients, $A_n = A_n(t)$ and $B_n = B_n(t)$, are indicated as dependent on time, because we anticipate that the coupling will influence the probability amplitude of the individual modes. The eigenfunctions $\boldsymbol{\Phi}_n^q = \boldsymbol{\Phi}_n^q(\boldsymbol{r},t)$ must satisfy eqn. (D.2) with $\varepsilon \to \varepsilon_q$ and in order to find the modes, we assume that we may split $\boldsymbol{\Phi}_n^q$ into a part that only depends on

[1] The polarization is given by $\boldsymbol{\mathcal{P}} = \boldsymbol{\mathcal{D}} - \varepsilon_0\boldsymbol{\mathcal{E}}$ and in a linear medium we can write $\boldsymbol{\mathcal{D}}$ as $\boldsymbol{\mathcal{D}} = \varepsilon\boldsymbol{\mathcal{E}}$.

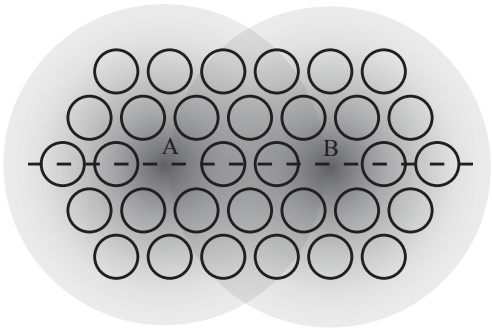

Fig. D.1: The system of two neighboring cavities under consideration. The cavities has been labeled A and B and the dielectric profile through two of the cavities, which is displayed in fig. D.2, is indicated by a dashed line.

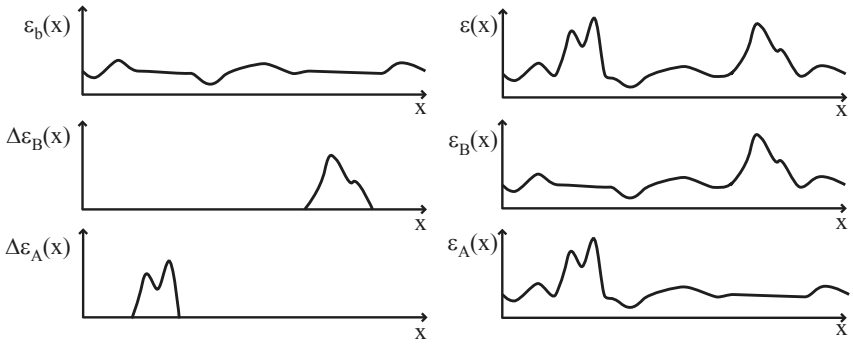

Fig. D.2: The dielectric profile for two neighboring cavities is shown as an example. Also shown are ε_b, ε_q and $\Delta\varepsilon_q$ for $q \in \{A, B\}$ to make clear the differences. The profile is made to correspond to the dashed line in fig. D.1, but note that the shown profiles do not represent the true dielectric profiles, but are merely meant as an illustration.

the spatial argument, $\boldsymbol{E}_n^q = \boldsymbol{E}_n^q(\boldsymbol{r})$, and a part that only depends on time, $T_n^q = T_n^q(t)$. Doing this, we effectively split the time evolution into a slowly varying envelope function, i.e. the expansion coefficient, and a term containing the fast oscillations at the optical frequency. Inserting $\boldsymbol{\Phi}_n^q = \boldsymbol{E}_n^q T_n^q$ in eqn. (D.2) and dividing by $\boldsymbol{E}_n^q T_n^q$ yields

$$\frac{c^2}{\varepsilon_q}\frac{\boldsymbol{\nabla}^2 \boldsymbol{E}_n^q}{\boldsymbol{E}_n^q} = \frac{\partial_t^2 T_n^q}{T_n^q} = -\left(\omega_n^q\right)^2 \tag{D.4}$$

where both sides of the equation must equal an arbitrary constant, $-\left(\omega_n^q\right)^2$, to hold for all values of $\boldsymbol{r}$ and t. We solve for T_n^q and find

$$T_n^q = C_{n,1}^q e^{i\omega_n^q t} + C_{n,2}^q e^{-i\omega_n^q t}, \quad C_{n,1}^q, C_{n,2}^q \in \mathbb{C}, \quad \omega_n^q > 0 \tag{D.5}$$

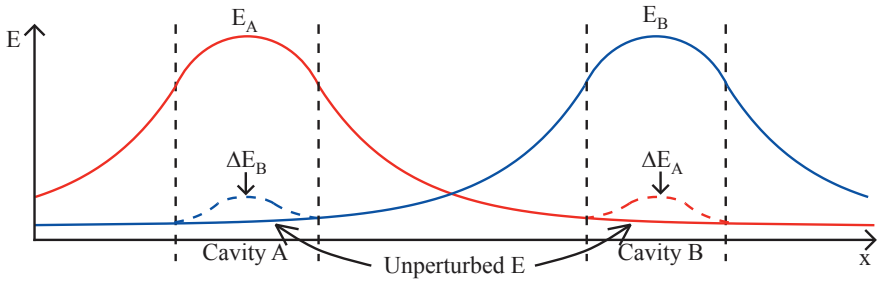

Fig. D.3: Schematic showing the difference between $\boldsymbol{\mathcal{E}}$ and $\Delta\boldsymbol{\mathcal{E}}$. The mode is mostly localized inside cavity A, but also has an exponentially decaying component outside the cavity. Cavity B has a different ε than the background and captures part of the mode.

Extending the sums in eqn. (D.3) to include $-\infty$, we may write the time evolution as $C^q_{n,1}e^{i\omega^q_n t}$ and absorb $C^q_{n,1}$ into the complex envelope functions. Then eqn. (D.3) becomes

$$\boldsymbol{\mathcal{E}}_A = \sum_{n=-\infty}^{\infty} A_n \boldsymbol{E}^A_n e^{i\omega^A_n t} \tag{D.6}$$

$$\boldsymbol{\mathcal{E}}_B = \sum_{n=-\infty}^{\infty} B_n \boldsymbol{E}^B_n e^{i\omega^B_n t} \tag{D.7}$$

where $\omega^q_{-n} = -\omega^q_n$. Now we treat the coupling of the cavities by letting $\varepsilon \to \varepsilon_b + \Delta\varepsilon_A + \Delta\varepsilon_B$, so that the uncoupled field is perturbed slightly. The change in the field in cavity A ($\Delta\boldsymbol{\mathcal{E}}_A$) is due to the perturbation from cavity B ($\Delta\varepsilon_B$), so that the field from cavity A becomes $\boldsymbol{\mathcal{E}}_A \to \boldsymbol{\mathcal{E}}_A + \Delta\boldsymbol{\mathcal{E}}_A$ (shown schematically in figure D.3). The total field changes as $\boldsymbol{\mathcal{E}} \to (\boldsymbol{\mathcal{E}}_A + \Delta\boldsymbol{\mathcal{E}}_A) + (\boldsymbol{\mathcal{E}}_B + \Delta\boldsymbol{\mathcal{E}}_B)$ and inserting this in the wave equation, eqn. (D.2), we find

$$0 = \left[c^2\boldsymbol{\nabla}^2 - (\varepsilon_b + \Delta\varepsilon_A + \Delta\varepsilon_B)\,\partial_t^2\right](\boldsymbol{\mathcal{E}}_A + \boldsymbol{\mathcal{E}}_B + \Delta\boldsymbol{\mathcal{E}}_A + \Delta\boldsymbol{\mathcal{E}}_B) \tag{D.8}$$

Neglecting terms that are second order in the perturbation yields

$$\begin{aligned} 0 = &\left[c^2\boldsymbol{\nabla}^2 - (\varepsilon_b + \Delta\varepsilon_A + \Delta\varepsilon_B)\,\partial_t^2\right](\boldsymbol{\mathcal{E}}_A + \boldsymbol{\mathcal{E}}_B) \\ &+ \left[c^2\boldsymbol{\nabla}^2 - \varepsilon_b\partial_t^2\right](\Delta\boldsymbol{\mathcal{E}}_A + \Delta\boldsymbol{\mathcal{E}}_B) \end{aligned} \tag{D.9}$$

Rearranging gives

$$\begin{aligned} \Delta\varepsilon_B\partial_t^2\boldsymbol{\mathcal{E}}_A + \Delta\varepsilon_A\partial_t^2\boldsymbol{\mathcal{E}}_B = &\left[c^2\boldsymbol{\nabla}^2 - \varepsilon_A\partial_t^2\right]\boldsymbol{\mathcal{E}}_A + \left[c^2\boldsymbol{\nabla}^2 - \varepsilon_B\partial_t^2\right]\boldsymbol{\mathcal{E}}_B \\ &+ \left[c^2\boldsymbol{\nabla}^2 - \varepsilon_b\partial_t^2\right](\Delta\boldsymbol{\mathcal{E}}_A + \Delta\boldsymbol{\mathcal{E}}_B) \end{aligned} \tag{D.10}$$

where $\varepsilon_q = \varepsilon_b + \Delta\varepsilon_q$. Inserting the expansion from eqn. (D.6), we note that the three first terms on the righthand side fulfill eqn. (D.4) and we can make

the substitution $c^2\boldsymbol{\nabla}^2\boldsymbol{\mathcal{E}}_A \to -\left(\omega_n^A\right)^2 \varepsilon_A \boldsymbol{\mathcal{E}}_A$ and likewise for B

$$\begin{aligned}\sum_n \Delta\varepsilon_B \partial_t^2 A_n \boldsymbol{E}_n^A e^{i\omega_n^A t} + \sum_n \Delta\varepsilon_A \partial_t^2 B_n \boldsymbol{E}_n^B e^{i\omega_n^B t} = \\ -\varepsilon_A \sum_n \left(\left(\omega_n^A\right)^2 + \partial_t^2\right) A_n \boldsymbol{E}_n^A e^{i\omega_n^A t} \\ -\varepsilon_B \sum_n \left(\left(\omega_n^B\right)^2 + \partial_t^2\right) B_n \boldsymbol{E}_n^B e^{i\omega_n^B t} \\ + \left[c^2\boldsymbol{\nabla}^2 - \varepsilon_b \partial_t^2\right](\Delta\boldsymbol{E}_A + \Delta\boldsymbol{E}_B)\end{aligned} \tag{D.11}$$

Now we multiply by $(\boldsymbol{E}_m^s)^*$ and integrate over all of space to pull out a single mode, $m \in \{\pm 1, \pm 2, \dots\}$, from cavity s. The last term on the righthand side becomes

$$\int d\boldsymbol{r}\, (\boldsymbol{E}_m^s)^* \left[c^2\boldsymbol{\nabla}^2 - \varepsilon_b \partial_t^2\right](\Delta\boldsymbol{\mathcal{E}}_A + \Delta\boldsymbol{\mathcal{E}}_B) \tag{D.12}$$

which we will neglect in order to get the change in the electric field in terms of the unperturbed fields[2].

The remaining terms can be be written in a simpler way by introducing the overlap integrals

$$\kappa_{mn}^{spq} = \int d\boldsymbol{r}\, (\boldsymbol{\mathcal{E}}_m^s)^* \Delta\varepsilon_p \boldsymbol{\mathcal{E}}_n^q \tag{D.13}$$

$$\gamma_{mn}^{sq} = \int d\boldsymbol{r}\, (\boldsymbol{\mathcal{E}}_m^s)^* \varepsilon_q \boldsymbol{\mathcal{E}}_n^q \tag{D.14}$$

so that we have

$$\begin{aligned}\sum_n \kappa_{mn}^{sBA} \partial_t^2 A_n e^{i\omega_n^A t} + \sum_n \kappa_{mn}^{sAB} \partial_t^2 B_n e^{i\omega_n^B t} = \\ -\sum_n \gamma_{mn}^{sA} \left(\left(\omega_n^A\right)^2 + \partial_t^2\right) A_n e^{i\omega_n^A t} \\ -\sum_n \gamma_{mn}^{sB} \left(\left(\omega_n^B\right)^2 + \partial_t^2\right) B_n e^{i\omega_n^B t}\end{aligned} \tag{D.15}$$

Looking more closely at the overlaps reveals that only κ_{mn}^{ppq} (i.e. for $s = p$) is non-negligible. This is because the integral in eqn. (D.13) is effectively over the cavity p, because $\Delta\varepsilon_p = 0$ outside the cavity p, and we expect the modes to decay to a lower value outside the cavity. The overlap of two modes (s and $q \neq p$) in the cavity p must therefore be smaller than κ_{mn}^{ppq} and is assumed to be negligible.

[2] This term is identically zero for the waveguide structure considered in appendix 14 in ref. [31] as the field can be divided into parallel and perpendicular terms. In that case the perpendicular terms can be transformed using Green's identity and evaluated as a contour integral at infinity, where the localized perpendicular terms of the field is zero. For PhC cavities the situation is bit more complicated as it is not obvious that the field can be divided into parallel and perpendicular parts and it is therefore not given that the terms evaluates to zero.

We also find for γ_{mn}^{sq} that the largest contribution comes from the case when $s = q$. The overlap between cavity modes from the same cavity must be much larger than the overlap between cavity modes from different cavities. So for weakly interacting cavities, we can neglect all γ's but the one for $s = q$. But for $s = q$ we have that the modes of the cavity are orthogonal, so $\gamma_{mn}^{ss} \to \gamma_s \delta_{nm}$, where γ_s also contains the normalization for the cavity mode, which we absorb into the κ's, so that instead of eqn. (D.13), we have

$$\kappa_{mn}^{spq} = \frac{\int d\boldsymbol{r} \left(\boldsymbol{\mathcal{E}}_m^s\right)^* \Delta\varepsilon_p \boldsymbol{\mathcal{E}}_n^q}{\int d\boldsymbol{r} \left(\boldsymbol{\mathcal{E}}_m^s\right)^* \varepsilon_q \boldsymbol{\mathcal{E}}_n^s} \tag{D.16}$$

Equation (D.15) then becomes

$$\sum_n \kappa_{mn}^{AB} \partial_t^2 B_n e^{i\omega_n^B t} = -\left(\left(\omega_m^A\right)^2 + \partial_t^2\right) A_m e^{i\omega_m^A t} \tag{D.17}$$

$$\sum_n \kappa_{mn}^{BA} \partial_t^2 A_n e^{i\omega_n^A t} = -\left(\left(\omega_m^B\right)^2 + \partial_t^2\right) B_m e^{i\omega_m^B t} \tag{D.18}$$

where $\kappa_{mn}^{sq} = \kappa_{mn}^{ssq}$.

Equations (D.17)-(D.18) give the coupling of the cavities and contain both changes in the amplitude ($\propto$ the photon density) and in the phase. The fact that the cavities are separated by a length of material with a different dielectric profile than that of the cavity, introduces a phase difference between the field in the cavity and the interacting field from neighboring cavities. This is because the phase velocity is different in different materials and the light has a shorter wavelength in higher index materials, i.e. $\lambda = \frac{c}{n\nu}$. We will not include this phase difference in the equations at this point, but rather introduce it in the initial conditions, when the equations are solved.

In order to introduce the corrections into the LREs, we need to recast them as first order differential equations. Each term in the sums on the LHS of eqns. (D.17)-(D.18) can be simplified by inserting the RHS of the other equation and neglecting terms of second order in the overlap integrals

$$\begin{aligned}\kappa_{mn}^{AB} \partial_t^2 B_n e^{i\omega_n^B t} &= -\kappa_{mn}^{AB} \left(\left(\omega_n^B\right)^2 B_n e^{i\omega_n^B t} + \sum_{n'} \kappa_{nn'}^{BA} \partial_t^2 A_{n'} e^{i\omega_{n'}^A t}\right) \\ &\approx -\kappa_{mn}^{AB} \left(\omega_n^B\right)^2 B_n e^{i\omega_n^B t}\end{aligned} \tag{D.19}$$

so that we have

$$\partial_t^2 A_m e^{i\omega_m^A t} = -\left(\omega_m^A\right)^2 A_m e^{i\omega_m^A t} - \sum_n \kappa_{mn}^{AB} \left(\omega_n^B\right)^2 B_n e^{i\omega_n^B t} \tag{D.20}$$

$$\partial_t^2 B_m e^{i\omega_m^B t} = -\left(\omega_m^B\right)^2 B_m e^{i\omega_m^B t} - \sum_n \kappa_{mn}^{BA} \left(\omega_n^A\right)^2 A_n e^{i\omega_n^A t} \tag{D.21}$$

Expanding the derivatives as

$$\partial_t^2 A_m e^{i\omega_m^A t} = e^{i\omega_m^A t}\left(-\left(\omega_m^A\right)^2 A_m + 2i\omega_m^A \partial_t A_m + \partial_t^2 A_m\right) \tag{D.22}$$

we may neglect the second derivative if the complex envelope is slowly varying. The result is

$$e^{i\omega_m^A t}\partial_t A_m = -\frac{1}{2i\omega_m^A}\sum_n \kappa_{mn}^{AB}\left(\omega_n^B\right)^2 B_n e^{i\omega_n^B t} \tag{D.23}$$

$$e^{i\omega_m^B t}\partial_t B_m = -\frac{1}{2i\omega_m^B}\sum_n \kappa_{mn}^{BA}\left(\omega_n^A\right)^2 A_n e^{i\omega_n^A t} \tag{D.24}$$

Now we turn the attention towards the exponentials containing the fast oscillations. Expanding the sum in the equation for cavity A in positive and negative parts and multiplying by $e^{-i\omega_m^A t}$ yields

$$\begin{aligned}\partial_t A_m = -\frac{1}{2i\omega_m^A}\sum_{n=1}^{\infty}\Big(&\kappa_{mn}^{AB}\left(\omega_n^B\right)^2 B_n e^{i\left(\omega_n^B-\omega_m^A\right)t} \\ &+\kappa_{m(-n)}^{AB}\left(-\omega_n^B\right)^2 B_{-n} e^{-i\left(\omega_m^A+\omega_n^B\right)t}\Big)\end{aligned} \tag{D.25}$$

Employing the Rotating Wave Approximation (RWA), where it is assumed that the eigenfrequencies of the cavities are almost equal, so that $\omega_n^q-\omega_m^s \ll \omega_n^q+\omega_m^s$, allows us to drop all fast oscillating terms as the contribution from these terms average to zero on the time scale of the slow oscillations [32]. Doing this and introducing the cavity-cavity detuning $\delta\omega_{mn}^{sq} = \omega_m^s - \omega_n^q$ yields

$$\partial_t A_m = -\frac{1}{2i\omega_m^A}\sum_n \kappa_{mn}^{AB}\left(\omega_n^B\right)^2 B_n e^{-i\delta\omega_{mn}^{AB}t} \tag{D.26}$$

Doing the same for B yields the final expressions for the two cavities

$$\partial_t A_m = -\frac{1}{2i}\sum_n \kappa_{mn}^{AB}\frac{\left(\omega_n^B\right)^2}{\omega_m^A}e^{-i\delta\omega_{mn}^{AB}t}B_n \tag{D.27}$$

$$\partial_t B_m = -\frac{1}{2i}\sum_n \kappa_{mn}^{BA}\frac{\left(\omega_n^A\right)^2}{\omega_m^B}e^{+i\delta\omega_{mn}^{AB}t}A_n \tag{D.28}$$

The last task is to transform the equations for the complex envelope functions into equations that describe the evolution of the amplitude ($\propto$ photon density) and the phase separately[3]. To do this we write the density proportional to the amplitude of the complex envelope $P_m^s = \sigma\left|A_m^s\right|^2$, where σ is a proportionality constant [101]. Taking the time derivative and using eqn. (D.27) gives for cavity A

$$\begin{aligned}\partial_t P_m^A &= \sigma\left(A_m^*\partial_t A_m + A_m\partial_t A_m^*\right) = 2\sigma\mathrm{Re}\left\{A_m^*\partial_t A_m\right\} = 2\sigma\mathrm{Im}\left\{iA_m^*\partial_t A_m\right\} \\ &= -\sigma\sum_n \kappa_{mn}^{AB}\frac{\left(\omega_n^B\right)^2}{\omega_m^A}\mathrm{Im}\left\{e^{-i\delta\omega_{mn}^{AB}t}A_m^*B_n\right\}\end{aligned} \tag{D.29}$$

[3] The reason we split into density and phase rather than deriving a laser rate equation for the complex envelope is that the LRE contains terms describing the spontaneous recombination, which requires random Langevin functions to be modeled properly in the complex envelope formalism. The LREs are the results of averaging the complex envelope version of the LREs and thus avoid this problem as the phase noise averages to zero.

where we assumed the overlap integrals to be real. Inserting $A_m = \sqrt{\frac{P_m^A}{\sigma}} e^{i\varphi_m^A}$, where $\varphi_m^A = \varphi_m^A(t)$ is the phase of the field in cavity A, gives

$$\begin{aligned}\partial_t P_m^A &= -\sum_n \kappa_{mn}^{AB} \frac{\left(\omega_n^B\right)^2}{\omega_m^A} \sqrt{P_m^A P_n^B} \mathrm{Im}\left\{e^{-i\delta\omega_{mn}^{AB} t} e^{-i\varphi_m^A} e^{i\varphi_n^B}\right\} \\ &= \sum_n \kappa_{mn}^{AB} \frac{\left(\omega_n^B\right)^2}{\omega_m^A} \sqrt{P_m^A P_n^B} \sin\left(\delta\omega_{mn}^{AB} t + \delta\varphi_{mn}^{AB}\right) \end{aligned} \tag{D.30}$$

where $\delta\varphi_{mn}^{AB} = \varphi_m^A - \varphi_n^B$. In the same way $\varphi_m^A = \frac{1}{2i} \ln\left(\frac{A_m}{A_m^*}\right)$ $(A_m \neq 0)$ produces an equation for the phase in cavity A [101].

$$\begin{aligned}\partial_t \varphi_m^A &= \frac{1}{2i}\left(\frac{\partial_t A_m}{A_m} - \frac{\partial_t A_m^*}{A_m^*}\right) = \frac{\partial_t A_m}{2iA_m} + \left(\frac{\partial_t A_m}{2iA_m}\right)^* = 2\mathrm{Re}\left\{\frac{\partial_t A_m}{2iA_m}\right\} \\ &= \frac{1}{2}\sum_n \kappa_{mn}^{AB} \frac{\left(\omega_n^B\right)^2}{\omega_m^A} \mathrm{Re}\left\{e^{-i\delta\omega_{mn}^{AB} t} \frac{B_n}{A_m}\right\} \\ &= \frac{1}{2}\sum_n \kappa_{mn}^{AB} \frac{\left(\omega_n^B\right)^2}{\omega_m^A} \sqrt{\frac{P_n^B}{P_m^A}} \cos\left(\delta\omega_{mn}^{AB} t + \delta\varphi_{mn}^{AB}\right) \end{aligned} \tag{D.31}$$

Doing the same for cavity B produces the final result

$$\partial_t P_m^A = +\sum_n \kappa_{mn}^{AB} \frac{\left(\omega_n^B\right)^2}{\omega_m^A} \sqrt{P_m^A P_n^B} \sin\left(\delta\omega_{mn}^{AB} t + \delta\varphi_{mn}^{AB}\right) \tag{D.32}$$

$$\partial_t P_m^B = -\sum_n \kappa_{mn}^{BA} \frac{\left(\omega_n^A\right)^2}{\omega_m^B} \sqrt{P_m^B P_n^A} \sin\left(\delta\omega_{nm}^{AB} t + \delta\varphi_{mn}^{AB}\right) \tag{D.33}$$

and

$$\partial_t \varphi_m^A = +\frac{1}{2}\sum_n \kappa_{mn}^{AB} \frac{\left(\omega_n^B\right)^2}{\omega_m^A} \sqrt{\frac{P_n^B}{P_m^A}} \cos\left(\delta\omega_{mn}^{AB} t + \delta\varphi_{mn}^{AB}\right) \tag{D.34}$$

$$\partial_t \varphi_m^B = +\frac{1}{2}\sum_n \kappa_{mn}^{BA} \frac{\left(\omega_n^A\right)^2}{\omega_m^B} \sqrt{\frac{P_n^A}{P_m^B}} \cos\left(\delta\omega_{nm}^{AB} t + \delta\varphi_{mn}^{AB}\right) \tag{D.35}$$

If we assume that the cavities have only one mode (the same) in the photonic bandgap, we can drop the mode indices and write $\delta\omega_{mn}^{AB} = \delta\omega$ and $\delta\varphi_{mn}^{AB} = \delta\varphi$. Assuming $\kappa = \kappa^{AB} = \kappa^{BA}$, we have for small detunings

$$\partial_t P_A = +\kappa\bar{\omega}\sqrt{P_A P_B} \sin\left(\delta\omega t + \delta\varphi\right) \tag{D.36}$$

$$\partial_t P_B = -\kappa\bar{\omega}\sqrt{P_B P_A} \sin\left(\delta\omega t + \delta\varphi\right) \tag{D.37}$$

and

$$\partial_t \varphi_A = \frac{1}{2}\kappa\bar{\omega}\sqrt{\frac{P_B}{P_A}} \cos\left(\delta\omega t + \delta\varphi\right) \tag{D.38}$$

$$\partial_t \varphi_B = \frac{1}{2}\kappa\bar{\omega}\sqrt{\frac{P_A}{P_B}} \cos\left(\delta\omega t + \delta\varphi\right) \tag{D.39}$$

which is the result found in section 6, where we postulated a simplified version of eqn. (D.26).

E. STANDARD VALUES

Here are listed the standard values used as referenced throughout the thesis.

Tab. E.1: Standard parameter values for a photonic crystal quantum well device.

Symbol	**Description**	**Value**
Q	Cavity quality factor.	2000
V_n	Mode volume in $\left(\frac{\lambda}{2n}\right)^3$.	0.2
Γ	Confinement factor.	0.1
n	Refractive index of GaAs.	3.5
$h\nu_c$	Cavity resonance.	0.8 eV
$h\nu_L$	Lower photonic band edge.	0.9 $h\nu_c$
$h\nu_U$	Upper photonic band edge.	1.1 $h\nu_c$
τ_{21}	Lifetime for a specific transition.	125 ps
ℓ	Quantum well width.	8 nm
m_e^*	Effective electron mass.	0.045 m_e
m_h^*	Effective electron mass.	0.37 m_e
γ	Homogeneous broadening.	0 meV

Tab. E.2: Standard parameter values for a photonic crystal quantum dot device.

Symbol	**Description**	**Value**
Q	Cavity quality factor.	2000
V_n	Mode volume in $\left(\frac{\lambda}{2n}\right)^3$.	4.4
Γ	Confinement factor.	0.01
n	Refractive index of GaAs.	3.5
$h\nu_c$	Cavity resonance.	0.8 eV
$h\nu_L$	Lower photonic band edge.	0.9 $h\nu_c$
$h\nu_U$	Upper photonic band edge.	1.1 $h\nu_c$
τ_{21}	Carrier lifetime for a specific transition.	125 ps
γ	Homogeneous broadening.	1 meV
σ	Inhomogeneous broadening.	10 meV
T	Temperature.	300 K
ρ_{QD}	Quantum dot density.	400 μm^{-2}

Tab. E.3: Standard parameter values for quantum well device A

Symbol	**Description**	**Value**
Q	Cavity quality factor.	10^4
V_n	Mode volume in $\left(\frac{\lambda}{2n}\right)^3$.	10
Γ	Confinement factor.	0.1
n	Refractive index of GaAs.	3.5
$h\nu_c$	Cavity resonance.	0.8 eV
$h\nu_L$	Lower photonic band edge.	0.9 $h\nu_c$
$h\nu_U$	Upper photonic band edge.	1.1 $h\nu_c$
τ_{sp}	Spontaneous recombination time.	1 ns
τ_{21}	Lifetime for a specific transition.	125 ps
τ_{nr}	Non-radiative recombination time.	1 ns
G_0	Material gain parameter.	1.284×10^5 m^{-1}
N_{tr}	Transparency carrier density.	1.2×10^{24} m^{-3}
N_s	Logarithmic gain parameter.	0.92 N_{tr}
ϵ	Gain suppression factor.	18 N_{tr}^{-1}
ℓ	Quantum well width.	8 nm
m_e^*	Effective electron mass.	0.045 m_e
m_h^*	Effective electron mass.	0.37 m_e
γ	Homogeneous broadening.	0 meV

Tab. E.4: Standard parameter values for quantum well device B

Symbol	**Description**	**Value**
Q	Cavity quality factor.	10^2
V_n	Mode volume in $\left(\frac{\lambda}{2n}\right)^3$.	0.1
Γ	Confinement factor.	0.1
n	Refractive index of GaAs.	3.5
$h\nu_c$	Cavity resonance.	0.8 eV
$h\nu_L$	Lower photonic band edge.	0.9 $h\nu_c$
$h\nu_U$	Upper photonic band edge.	1.1 $h\nu_c$
τ_{sp}	Spontaneous recombination time.	1 ns
τ_{21}	Lifetime for a specific transition.	125 ps
τ_{nr}	Non-radiative recombination time.	1 ns
G_0	Material gain parameter.	1.284×10^5 m^{-1}
N_{tr}	Transparency carrier density.	1.2×10^{24} m^{-3}
N_s	Logarithmic gain parameter.	0.92 N_{tr}
ϵ	Gain suppression factor.	18 N_{tr}^{-1}
ℓ	Quantum well width.	8 nm
m_e^*	Effective electron mass.	0.045 m_e
m_h^*	Effective electron mass.	0.37 m_e
γ	Homogeneous broadening.	0 meV

Tab. E.5: Standard parameter values for quantum well random photonic crystal waveguides.

Symbol	Description	Value
Γ	Confinement factor.	0.15
n	Refractive index of GaAs.	3.55
λ	Measured wavelength.	1575 nm
τ_{sp}	Spontaneous recombination time.	434 ps
τ_{nr}	Non-radiative recombination time.	1 ns
G_0	Material gain parameter.	1.5×10^5 m^{-1}
N_{tr}	Transparency carrier density.	1×10^{24} m^{-3}

Tab. E.6: Standard parameter values for a photonic crystal quantum dot LED.

Symbol	Description	Value
Q	Cavity quality factor.	2000
V_n	Mode volume in $\left(\frac{\lambda}{2n}\right)^3$.	1
Γ	Confinement factor.	0.01
n	Refractive index of GaAs.	3.4
$h\nu_c$	Cavity resonance energy.	0.8 eV
$h\nu_L$	Lower photonic band edge.	$0.9h\nu_c$
$h\nu_U$	Upper photonic band edge.	$1.1h\nu_c$
τ_{21}	Carrier lifetime for a specific transition.	125 ps
T	Temperature.	100 K
γ	Homogeneous broadening.	100 μeV
ρ_{QD}	Quantum dot density.	2×10^4 m^{-3}

Tab. E.7: Parameter values for quantum dot device 1 for the comparison in section 4.5.

Symbol	Description	Value
Q	Cavity quality factor.	10000
F	Purcell factor	25
V_n	Mode volume in $\left(\frac{\lambda}{2n}\right)^3$.	244
V_{QD}	QD volume (10 by 20 by 20 nm).	4×10^{-6} μm^3
V_a	Active volume ($V_{QD}N_{QD}$).	4×10^{-4} μm^3
Γ	Confinement factor.	1.6×10^{-4}
n	Refractive index.	$\sqrt{12.5}$
λ_c	Cavity resonance frequency.	1550 nm
τ_{21}	Lifetime for a specific transition.	1 ns
β	Spontaneous emission factor	0.3
N_{QD}	Number of quantum dots	100
T	Temperature.	100 K
Γ_H	Homogeneous broadening.	100 μeV
σ	Inhomogeneous broadening.	1 μeV

Tab. E.8: Parameter values for quantum dot device 2 for the comparison in section 4.5.

Symbol	Description	Value
Q	Cavity quality factor.	10000
F	Purcell factor	50
V_n	Mode volume in $\left(\frac{\lambda}{2n}\right)^3$.	122
V_{QD}	QD volume (10 by 20 by 20 nm).	4×10^{-6} μm^3
V_a	Active volume ($V_{QD}N_{QD}$).	4×10^{-4} μm^3
Γ	Confinement factor.	3.1×10^{-4}
n	Refractive index.	$\sqrt{12.5}$
λ_c	Cavity resonance frequency.	1550 nm
τ_{21}	Lifetime for a specific transition.	1 ns
β	Spontaneous emission factor	0.1
N_{QD}	Number of quantum dots	100
T	Temperature.	100 K
Γ_H	Homogeneous broadening.	100 μeV
σ	Inhomogeneous broadening.	1 μeV

Tab. E.9: Parameter values for the modified Noda cavity treated in section 5.2.

Symbol	Description	Value
a	Hole lattice constant.	240 nm
d	Slab thickness.	0.646 a
r	Hole radius.	0.275 a
s_1	Shift of 1$^{\text{st}}$ hole.	0.175 a
s_2	Shift of 2$^{\text{nd}}$ hole.	0.025 a
s_3	Shift of 3$^{\text{rd}}$ hole.	0.175 a
n	Refractive index.	3.5
N_{holes}	Number of hole layers.	7
R	Resolution.	20
T_{as}	Calculation time after sources.	6000 cycles
d_{PML}	PML thickness.	1.8 a

Tab. E.10: Converged parameter set for single defect H1 photonic crystal cavity.

Symbol	Description	Value
a	Hole lattice constant.	280 nm
d	Slab thickness.	0.59 a
r	Hole radius.	0.38 a
n	Refractive index.	3.5
N_{holes}	Number of hole layers.	6
R	Resolution.	20
T_{as}	Calculation time after sources.	40 cycles
d_{PML}	PML thickness.	2 a

Tab. E.11: Standard parameter values for coupled quantum well photonic crystal cavities

Symbol	**Description**	**Value**
Γ	Confinement factor.	0.1
n	Refractive index of GaAs.	3.5
β	Spontaneous emission factor	0.1
α	Linewidth enhancement factor	4
λ_c	Cavity resonance wavelength	937 nm
Q	Cavity quality factor.	1250
V_n	Mode volume in $\left(\frac{\lambda}{2n}\right)^3$.	15
F_{eff}	Purcell factor	50
G_0	Material gain parameter.	0.18 μm^{-1}
N_{tr}	Transparency carrier density.	1.8×10^6 μm^{-3}
N_s	Logarithmic gain parameter.	1.8 μm^{-3}
A	Surface recombination coefficient.	10^{-3} ps^{-1}
B	Bimolecular recombination coefficient.	1.8×10^{-4} $N_{tr}^{-1}\text{ps}^{-1}$
C	Auger recombination coefficient.	3.2×10^{-5} $N_{tr}^{-2}\text{ps}^{-1}$

LIST OF PUBLICATIONS

The following publications have been authored or coauthored during the course of the Ph.D.

Journal Publications

1. T. Suhr, N. Gregersen, K. Yvind, and J. Mørk, *Modulation response of nanoLEDs and nanolasers exploiting Purcell enhanced spontaneous emission*, Opt. Express, **18**, 11, 11230-11241 (2010).

2. C. Agger, T. S. Skovgård, N. Gregersen, and J. Mørk, *Modeling of mode-locked coupled-resonator optical waveguide lasers*, IEEE J. Quantum Electron., **46**, 12, 1804-1812 (2010).

3. M. Schubert, T. Suhr, S. Ek, E. Semenova, J. M. Hvam and K. Yvind, *Lambda shifted photonic crystal cavity laser*, Appl. Phys. Lett., **97**, 19, 191109, (2010).

4. T. Suhr, N. Gregersen, M. Lorke and J. Mørk, *Modulation response of quantum dot nanolight-emitting-diodes exploiting purcell-enhanced spontaneous emission*, Appl. Phys. Lett., **98**, 21, 211109 (2011).

5. T. Suhr, P. T. Kristensen and J. Mørk, *Phase-locking regimes of photonic crystal nanocavity laser arrays*, Appl. Phys. Lett., **99**, 25 (2011).

6. J. Liu, S. Ek, T. Suhr, M. Schubert, P. D. Garcia, H. Thyrrestrup, S. Stobbe, J. Moerk and P. Lodahl, *Slow light controlled micro-cavity random lasing in photonic crystal waveguides*, *Under preparation.*

7. N. Gregersen, T. Suhr, M. Lorke, and J. Mørk, *Quantum-dot nano-cavity lasers with Purcell-enhanced stimulated emission*, Appl. Phys. Lett., **100**, 13 (2012).

8. M. Lorke, T. Suhr, N. Gregersen, and J. Mørk, *Theory of nanolaser devices: modified rate equation analysis vs. microscopic theory*, *Under review.*

Conference Papers

1. M. Schubert, L. H. Frandsen, T. Suhr, T. Lund-Hansen, H. T. Nielsen, P. Lodahl, J. M. Hvam, K. Yvind, *Sub-threshold wavelength splitting in coupled photonic crystal cavity arrays*, PECS VIII Australia (2009).

2. M. Schubert, L. H. Frandsen, T. Suhr, T. Lund-Hansen, H. T. Nielsen, M. Bichler, J. J. Finley, P. Lodahl, J. M. Hvam and K. Yvind, *Sub-threshold investigation of two coupled photonic crystal cavities*, Technical digest, CLEO/IQEC, Baltimore, MA, USA, 1-2 (2009).

3. T. Suhr, P. T. Kristensen, L. H. Frandsen, M. Schubert, N. Gregersen and J. Mørk, *Nonlinear dynamics in photonic crystal nanocavity lasers*, Conference abstract series, CLEO/Europe - EQEC, Munich, Germany, 1-1 (2009).

4. M. Schubert, T. Suhr, S. Ek, E. Semenova, J. M. Hvam and K. Yvind, *Quarter-lambda-shifted photonic crystal lasers*, 22nd IEEE International Semiconductor Laser Conference, Kyoto, Japan, 129-130 (2010).

Book Chapters

1. N. Gregersen, T. Suhr, S. Ek, W. Xue, I.-S. Chung and J. Mørk, *The optical chip : high speed and diminutive size*, Beyond optical horizons : today and tomorrow with photonics, DTU Fotonik, Kgs. Lyngby, 1, 235-249 (2009).

LIST OF FIGURES

LIST OF ABBREVIATIONS

CEM	Cluster Expansion Model
DBR	Distributed Bragg Reflector
DOS	Density-Of-States
FDTD	Finite-Difference Time-Domain
FWHM	Full Width at Half Maximum
I/O curve	Input-Output curve.
LASER	Light Amplification by Stimulated Emission of Radiation
LDOS	Local Density Of States
LED	Light Emitting Diode
LRE	Laser Rate Equation
PESE	Purcell Enhanced Stimulated Emission
PhC	Photonic Crystal
PML	Perfectly Matched Layers
Q-factor	Quality factor
QD	Quantum Dot
QW	Quantum Well
RWA	Rotating Wave Approximation
SEM	Scanning Electron Microscopy
TE	Transverse Electric
TIR	Total Internal Reflection
TM	Transverse Magnetic

LIST OF SYMBOLS

BIBLIOGRAPHY

[1] H. J. R. Dutton. Understanding optical communication, September 1998.

[2] H. C. H. Mulvad, M. Galili, L. K. Oxenløwe, H. Hu, A. T. Clausen, J. B. Jensen, C. Peucheret, and P. Jeppesen. Demonstration of 5.1 tbit/s data capacity on a single-wavelength channel. *Opt. Express*, 18 (2):1438–1443, Jan 2010.

[3] D. A. B. Miller. Physical reasons for optical interconnection. *International Journal of Optoelectronics*, 11(3):155–168, 1997.

[4] D. A. B. Miller. Rationale and challenges for optical interconnects to electronic chips. *Proc. IEEE*, 88(6):728–749, June 2000.

[5] E. B. Desurvire. Capacity demand and technology challenges for lightwave systems in the next two decades. *J. Lightwave Technol.*, 24 (12):4697–4710, 2006.

[6] D. A. B. Miller. Device requirements for optical interconnects to silicon chips. *Proc. IEEE*, 97(7):1166 –1185, 2009.

[7] D. Bimberg, N. Kirstaedter, N. N. Ledentsov, Z. I. Alferov, P. S. Kop'ev, and V. M. Ustinov. Ingaas-gaas quantum-dot lasers. *IEEE J. Sel. Top. Quantum Electron.*, 3(2):196–205, Apr 1997. ISSN 1077-260X.

[8] D. G. Deppe and H. Huang. Quantum-dot vertical-cavity surface-emitting laser based on the purcell effect. *Appl. Phys. Lett.*, 75 (22):3455–3457, 1999.

[9] O. Painter, R. K. Lee, A. Scherer, A. Yariv, J. D. O'Brien, P. D. Dapkus, and I. Kim. Two-dimensional photonic band-gap defect mode laser. *Science*, 284(5421):1819–1821, 1999.

[10] M. Loncar, T. Yoshie, A. Scherer, P. Gogna, and Y. Qiu. Low-threshold photonic crystal laser. *Appl. Phys. Lett.*, 81(15):2680–2682, 2002.

[11] J. Scheuer, W. M. J. Green, G. A. DeRose, and A. Yariv. Lasing from a circular bragg nanocavity with an ultrasmall modal volume. *Appl. Phys. Lett.*, 86(25):251101, 2005.

[12] H. Altug, D. Englund, and J. Vučković. Ultrafast photonic crystal nanocavity laser. *Nat. Phys.*, 2(7):484–488, July 2006. ISSN 1745-2473.

[13] S. Strauf, K. Hennessy, M. T. Rakher, Y.-S. Choi, A. Badolato, L. C. Andreani, E. L. Hu, P. M. Petroff, and D. Bouwmeester. Self-tuned quantum dot gain in photonic crystal lasers. *Phys. Rev. Lett.*, 96(12): 127404, 2006.

[14] D. Englund, H. Altug, B. Ellis, and J. Vučković. Ultrafast photonic crystal lasers. *Laser Photonics Rev.*, 2(4):264–274, 2008. ISSN 1863-8899.

[15] D. Englund, H. Altug, and J. Vučković. Time-resolved lasing action from single and coupled photonic crystal nanocavity array lasers emitting in the telecom band. *J. Appl. Phys.*, 105(9):093110, 2009.

[16] M. Eichfelder, W.-M. Schulz, M. Reischle, M. Wiesner, R. Roßbach, M. Jetter, and P. Michler. Room-temperature lasing of electrically pumped red-emitting $InP/(Al_{0.20}Ga_{0.80})_{0.51}In_{0.49}P$ quantum dots embedded in a vertical microcavity. *Appl. Phys. Lett.*, 95(13):131107, 2009.

[17] M. Nomura, N. Kumagai, S. Iwamoto, Y. Ota, and Y. Arakawa. Photoniccrystal nanocavity laser with a single quantum dot gain. *Opt. Express*, 17(18):15975–15982, August 2009.

[18] M. Nomura, N. Kumagai, S. Iwamoto, Y. Ota, and Y. Arakawa. Laser oscillation in a strongly coupled single quantum dot-nanocavity system. *Nat. Phys.*, 2010.

[19] R. Hostein, R. Braive, L. Le Gratiet, A. Talneau, G. Beaudoin, I. Robert-Philip, I. Sagnes, and A. Beveratos. Demonstration of coherent emission from high-β photonic crystal nanolasers at room temperature. *Opt. Lett.*, 35(8):1154–1156, 2010.

[20] M. Nomura, Y. Ota, N. Kumagai, S. Iwamoto, and Y. Arakawa. Zero-cell photonic crystal nanocavity laser with quantum dot gain. *Appl. Phys. Lett.*, 97(19):191108, 2010.

[21] T. Kakitsuka K. Nozaki T. Segawa T. Sato Y. Kawaguchi S. Matsuo, A. Shinya and M. Notomi. High-speed ultracompact buried heterostructure photonic-crystal laser with 13 fJ of energy consumed per bit transmitted. *Nat. Photonics*, 4(9):648–654, 09 2010.

[22] B. Ellis, M. A. Mayer, G. Shambat, T. Sarmiento, J. Harris, E. E. Haller, and J. Vučković. Ultralow-threshold electrically pumped quantum-dot photonic-crystal nanocavity laser. *Nat. Photonics*, 5(5): 297–300, 2011.

[23] J. J. Coleman, J. D. Young, and A. Garg. Semiconductor quantum dot lasers: A tutorial. *J. Lightwave Technol.*, 29(4):499–510, Feb 2011.

[24] E. M. Purcell. Spontaneous emission probabilities at radio frequencies. *Phys. Rev.*, 69:681, 1946.

[25] H. Yokoyama and S. D. Brorson. Rate equation analysis of microcavity lasers. *J. Appl. Phys.*, 1989.

[26] E. K. Lau, A. Lakhani, R. S. Tucker, and M. C. Wu. Enhanced modulation bandwidth of nanocavity light emitting devices. *Opt. Express*, 17(10):7790–7799, 2009.

[27] L. V. Asryan and R. A. Suris. Upper limit for the modulation bandwidth of a quantum dot laser. *Applied Physics Letters*, 96(22): 221112, 2010.

[28] L. V. Asryan, Y. Wu, and R. A. Suris. Carrier capture delay and modulation bandwidth in an edge-emitting quantum dot laser. *Applied Physics Letters*, 98(13):131108, 2011.

[29] S. S. Wang and H. G. Winful. Dynamics of phase-locked semiconductor laser arrays. *Appl. Phys. Lett.*, 52(21):1774–1776, 1988.

[30] H. G. Winful and S. S. Wang. Stability of phase locking in coupled semiconductor laser arrays. *Appl. Phys. Lett.*, 53(20):1894–1896, 1988.

[31] L. A. Coldren and S. W. Corzine. *Diode Lasers and Photonic Integrated Circuits*. John Weiley & Sons, Inc., 1995.

[32] M. O. Scully and M. S. Zubairy. *Quantum Optics*. Cambridge University Press, 1997.

[33] B. Valeur and M. N. Berberan-Santos. A brief history of fluorescence and phosphorescence before the emergence of quantum theory. *J. Chem. Edu.*, 2011.

[34] B. H. Bransden and C. J. Joachain. *Quantum Mechanics*. Prentice Hall, 2000.

[35] L. E. Ballentine. *Quantum Mechanics*. World Scientific Publishing Co., 2003.

[36] K. Jacobi. Atomic structure of InAs quantum dots on GaAs. *Prog. Surf. Sci*, 2003.

[37] C. Nì Allen, P. Finnie, S. Raymond, Z. R. Wasilewski, and S. Fafard. Inhomogeneous broadening in quantum dots with ternary aluminum alloys. *Appl. Phys. Lett.*, 79(17):2701–2703, 2001.

[38] J. M. Gerard. *P. Michler, Single Quantum Dots: Fundamentals, Applications and New Concepts, (Springer, New York, 2004), Chap. 7 by J. Gerard.*, chapter 7, pages 269–309. Springer, 2004.

[39] J. D. Jackson. *Classical Electrodynamics*. Wiley, 3 edition, 1962.

[40] D. Englund, D. Fattal, E. Waks, G. Solomon, B. Zhang, T. Nakaoka, Y. Arakawa, Y. Yamamoto, and J. Vučković. Controlling the spontaneous emission rate of single quantum dots in a two-dimensional photonic crystal. *Phys. Rev. Lett.*, 95:013904, Jul 2005.

[41] X. Hachair, R. Braive, G. L. Lippi, D. Elvira, L. Le Gratiet, A. Lemaitre, I. Abram, I. Sagnes, I. Robert-Philip, and A. Beveratos. Identification of the stimulated-emission threshold in high-β nanoscale lasers through phase-space reconstruction. *Phys. Rev. A*, 83:053836, May 2011.

[42] F. L. Pedrotti and L. S. Pedrotti. *Introduction to optics*. Prentice Hall, 1993. ISBN 9780135015452.

[43] J. D. Joannopoulos, Robert D. Meade, and Joshua N. Winn. *Photonic crystals: molding the flow of light*. Princeton University Press, 2008. ISBN 9780691124568.

[44] M.H. MacDougal, H. Zhao, P.D. Dapkus, M. Ziari, and W.H. Steier. Wide-bandwidth distributed bragg reflectors using oxide/gaas multilayers. *Electron. Lett.*, 30(14):1147 –1149, jul 1994. ISSN 0013-5194.

[45] M. P. Marder. *Condenced Matter Physics*. John Weiley & Sons, Inc., 2000.

[46] E. Yablonovitch. Inhibited spontaneous emission in solid-state physics and electronics. *Phys. Rev. Lett.*, 58(20):2059–2062, May 1987.

[47] S. John. Strong localization of photons in certain disordered dielectric superlattices. *Phys. Rev. Lett.*, 58(23):2486–2489, Jun 1987.

[48] E. Yablonovitch, T. J. Gmitter, and K. M. Leung. Photonic band structure: The face-centered-cubic case employing nonspherical atoms. *Phys. Rev. Lett.*, 67(17):2295–2298, Oct 1991.

[49] R. Coccioli, M. Boroditsky, K.W. Kim, Y. Rahmat-Samii, and E. Yablonovitch. Smallest possible electromagnetic mode volume in a dielectric cavity. *IEE.: Proc. Optoelectron.*, 145(6):391 –397, dec 1998. ISSN 1350-2433.

[50] J. T. Robinson, C. Manolatou, L. Chen, and M. Lipson. Ultrasmall mode volumes in dielectric optical microcavities. *Phys. Rev. Lett.*, 95: 143901, Sep 2005.

[51] Y. Akahane, T. Asano, B.-S. Song, and S. Noda. High-q photonic nanocavity in a two-dimensional photonic crystal. *Letters to Nature*, (425):944–947, October 2003.

[52] M. Nomura, S. Iwamoto, K. Watanabe, N. Kumagai, Y. Nakata, S. Ishida, and Y. Arakawa. Room temperature continuous-wave lasing in photonic crystal nanocavity. *Opt. Express*, 14(13):6308–6315, Jun 2006.

[53] S.-H. Kim, S.-K. Kim, and Y.-H. Lee. Vertical beaming of wavelength-scale photonic crystal resonators. *Phys. Rev. B*, 73(23): 235117, Jun 2006.

[54] S. Noda, M. Fujita, and T. Asano. Spontaneous-emission control by photonic crystals and nanocavities. *Nat. Photon.*, 1(8), 2007.

[55] M. Schubert, T. Suhr, S. Ek, E. S. Semenova, J. M. Hvam, and K. Yvind. Lambda shifted photonic crystal cavity laser. *Appl. Phys. Lett.*, 97(19):191109 –191109–3, nov 2010. ISSN 0003-6951.

[56] B.-S. Song, S. Noda, T. Asano, and Y. Akahane. Ultra-high-q photonic double-heterostructure nanocavity. *Nat. Mater.*, 4(3):207–210, 2005.

[57] G. B. Arfken and H. J. Weber. *Mathematical Methods for Physicists*. Academic Press, 5 edition, 2001.

[58] N. M. Temme. *NIST Handbook of Mathematical Functions*. Cambridge University Press, 2010.

[59] Y. Sun, S. E. Thomson, and T. Nishida. *Strain effect in semiconductors: Theory and device applications*. Springer New York, 2010.

[60] T. Suhr, N. Gregersen, K. Yvind, and J. Mørk. Modulation response of nanoleds and nanolasers exploiting purcell enhanced spontaneous emission. *Opt. Express*, 18(11):11230–11241, May 2010.

[61] A. J. Campillo, J. D. Eversole, and H.-B. Lin. Cavity quantum electrodynamic enhancement of stimulated emission in microdroplets. *Phys. Rev. Lett.*, 67:437–440, Jul 1991.

[62] M. Djiango, T. Kobayashi, and W. J. Blau. Cavity-enhanced stimulated emission cross section in polymer microlasers. *Appl. Phys. Lett.*, 93(14): 143306, 2008.

[63] C. Gies, J. Wiersig, M. Lorke, and F. Jahnke. Semiconductor model for quantum-dot-based microcavity lasers. *Phys. Rev. A*, 75:013803, Jan 2007.

[64] N. Gregersen, M. Lorke, T. Suhr, and J. Mørk. Quantum-dot nano-cavity lasers with purcell-enhanced stimulated emission. *Accepted for Appl. Phys. Lett.*, 2012.

[65] H. Schoeller. A new transport equation for single-time green's functions in an arbitrary quantum system. general formalism. *Annals of Physics*, 229(2):273 – 319, 1994. ISSN 0003-4916.

[66] J. Fricke. Transport equations including many-particle correlations for an arbitrary quantum system: A general formalism. *Annals of Physics*, (252):479–498, 1996.

[67] C. Wöhler J. Fricke, V. Meden and K. Schönhammer. Improved transport equations including correlations for electron-phonon systems: Comparison with exact solutions in one dimension. *Annals of Physics*, 1997.

[68] K. Hoffman and R. Kunze. *Linear Algebra*. Prentice Hall, inc, 1961.

[69] R. S. Tucker. High-speed modulation of semiconductor lasers. *IEEE Trans. Electron Devices*, 32(12):2572–2584, Dec 1985. ISSN 0018-9383.

[70] P. W. Anderson. Absence of diffusion in certain random lattices. *Phys. Rev.*, 109:1492–1505, Mar 1958.

[71] L. Sapienza, H. Thyrrestrup, S. Stobbe, P. D. Garcia, S. Smolka, and P. Lodahl. Cavity quantum electrodynamics with anderson-localized modes. *Science*, 327(5971):1352–1355, 2010.

[72] J. Liu, S. Ek, T. Suhr, M. Schubert, P. D. Garcia, H. Thyrrestrup, S. Stobbe, J. Moerk, and P. Lodahl. Slow light controlled micro-cavity random lasing in photonic crystal waveguides. *Under preparation*, 2012.

[73] M. Bayer and A. Forchel. Temperature dependence of the exciton homogeneous linewidth in $In_{0.60}Ga_{0.40}As/GaAs$ self-assembled quantum dots. *Phys. Rev. B*, 65(4):041308, Jan 2002.

[74] T. Suhr, N. Gregersen, M. Lorke, and J. Mørk. Modulation response of quantum dot nanolight-emitting-diodes exploiting purcell-enhanced spontaneous emission. *Appl. Phys. Lett.*, 98(21):211109, 2011.

[75] M. Lorke, T. Suhr, N. Gregersen, and J. Mørk. Theory of nanolaser devices: modified rate equation analysis vs. microscopic theory. *Under review*, 2012.

[76] D. J. Griffiths. *Introduction to Electrodynamics*. Prentice Hall, 3 edition, 1999.

[77] A. Taflove. *Computational Electrodynamics: The Finite-Difference Time-Domain Method*. Artech House, Inc., 1995.

[78] A. F. Oskooi, D. Roundy, M. Ibanescu, P. Bermel, J.D. Joannopoulos, and S. G. Johnson. Meep: A flexible free-software package for electromagnetic simulations by the fdtd method. *Comput. Phys. Commun.*, 181(3):687 – 702, 2010. ISSN 0010-4655.

[79]

[80] A. Farjadpour, D. Roundy, A. Rodriguez, M. Ibanescu, P. Bermel, J. D. Joannopoulos, S. G. Johnson, and G. W. Burr. Improving accuracy by subpixel smoothing in the finite-difference time domain. *Opt. Lett.*, 31 (20):2972–2974, Oct 2006.

[81] C. A. Balanis. *Advanced Engineering Electromagnetics*. John Wiley & Sons, 1989.

[82] J. Vučković, M. Loncar, H. Mabuchi, and A. Scherer. Optimization of the q factor in photonic crystal microcavities. *IEEE J. Quantum Electron.*, 38(7):850–856, Jul 2002. ISSN 0018-9197.

[83] Y. Zeng and J. V. Moloney. Polarization-current-based, finite-difference time-domain, near-to-far-field transformation. *Opt. Lett.*, 34(10): 1600–1602, May 2009.

[84] K. S. Krane. *Modern Physics*. John Weiley & Sons, Inc., 2 edition, 1996.

[85] D. K. Serkland, K. D. Choquette, G. R. Hadley, K. M. Geib, and A. A. Allerman. Two-element phased array of antiguided vertical-cavity lasers. *Appl. Phys. Lett.*, 75(24):3754–3756, 1999.

[86] D. Zhou and L. J. Mawst. Two-dimensional phase-locked antiguided vertical-cavity surface-emitting laser arrays. *Appl. Phys. Lett.*, 77(15): 2307–2309, 2000.

[87] J. J. Raftery, A. C. Lehman, A. J. Danner, P. O. Leisher, A. V. Giannopoulos, and K. D. Choquette. In-phase evanescent coupling of two-dimensional arrays of defect cavities in photonic crystal vertical cavity surface emitting lasers. *Appl. Phys. Lett.*, 89(8):081119, 2006.

[88] S. Riyopoulos. Coherent phase locking, collective oscillations, and stability in coupled vertical-cavity-surface emitting laser arrays. *Phys. Rev. A*, 66(5):053820, Nov 2002.

[89] S. Riyopoulos. Optical modulation waves excited in microlaser arrays. *J. Opt. Soc. Am. B*, 19(7):1544–1548, 2002.

[90] S. Riyopoulos. Equilibrium bifurcations and chaotic transitions in coupled microlaser lattices. *Chaos: An Interdisciplinary Journal of Nonlinear Science*, 14(4):1105–1122, 2004.

[91] H. G. Winful L. Rahman. Improved coupled-mode theory for the dynamics of semiconductor laser arrays. *Opt. Lett.*, 18(2):128–130, 1993.

[92] H. G. Winful, S. Allen, and L. Rahman. Validity of the coupled-oscillator model for laser-array dynamics. *Opt. Lett.*, 18(21): 1810–1812, 1993.

[93] L. Rahman and H.G. Winful. Nonlinear dynamics of semiconductor laser arrays: a mean field model. *IEEE J. Quantum Electron.*, 30(6): 1405–1416, Jun 1994. ISSN 0018-9197.

[94] A. Yariv. *Optical Electronics*. Holt McDougal, 1985.

[95] K. M. Lee, P. T. Leung, and K. M. Pang. Dyadic formulation of morphology-dependent resonances. i. completeness relation. *J. Opt. Soc. Am. B*, 16(9):1409–1417, Sep 1999.

[96] T. C. Newell, D. J. Bossert, A. Stintz, B. Fuchs, K. J. Malloy, and L. F. Lester. Gain and linewidth enhancement factor in inas quantum-dot laser diodes. *IEEE Photonics Technol. Lett.*, 11(12):1527 –1529, dec 1999. ISSN 1041-1135.

[97] Z. Mi, P. Bhattacharya, and S. Fathpour. High-speed 1.3 mu m tunnel injection quantum-dot lasers. *Appl. Phys. Lett.*, 86(15):153109, 2005.

[98] S. Melnik, G. Huyet, and A. Uskov. The linewidth enhancement factor α of quantum dot semiconductor lasers. *Opt. Express*, 14(7):2950–2955, Apr 2006.

[99] J. Scheuer and A. Yariv. Coupled-waves approach to the design and analysis of bragg and photonic crystal annular resonators. *IEEE J. Quantum Electron.*, 39(12):1555 – 1562, dec. 2003. ISSN 0018-9197.

[100] V. A. Mandelshtam and H. S. Taylor. Harmonic inversion of time signals and its applications. *J. Chem. Phys.*, 107(17):6756–6769, 1997.

[101] J. Mørk. *Nonlinear dynamics and Stochastic Behaviour of Semiconductor Lasers with Optical Feedback*. PhD thesis, The Technical University of Denmark, 1989.